2017

Digital-Lithographic Fabrication of Unconventional 3D Microstructures

Ran He
Lehigh University

Digital-Lithographic Fabrication of Unconventional 3D Microstructures

by

Ran He

Presented to the Graduate and Research Committee of Lehigh University

in Candidacy for the Degree of Doctor of Philosophy

in Mechanical Engineering

Lehigh University

August 2017

DISSERTATION SIGNATURE SHEET

Approved and recommended for acceptance as a dissertation in partial fulfillment of the requirements for the degree of Doctor of Philosophy.

_____
Date

_____
Dissertation Director: Dr. Yaling Liu

_____
Accepted Date

Committee Members:

_____
Committee Chair: Dr. Yaling Liu

_____
Dr. Brandon Krick

_____
Dr. H. Daniel Ou-Yang

_____
Dr. Chao Zhou

Acknowledgements

It was a great journey and I'll cherish the experiences and memories at Lehigh University. I am grateful to have a great many people who provide guidance, encouragement, trust, friendship, and joy.

Utmost gratitude is owed to my adviser, Prof. Yaling Liu, who brought me to the field of 3D printing and digital fabrication. Prof. Liu shared his knowledge and experience with me, and provided continuous support. His encouragement of developing my own thoughts was a big deal for me, making me grow into self-motivated individuals. I truly appreciate Prof. Liu's trust and all the opportunities he provided, which pushed me to explore things that I never thought of before.

I'd also like to thank all my Ph.D. committee members, Prof. Chao Zhou, Prof. Brandon Krick, and Prof. H. Daniel Ou-Yang. Without their insightful guidance and suggestions, this dissertation cannot be made possible. My special thanks goes to Prof. Chao Zhou, who supported my research and assisted my future career.

Special gratitude also goes to Prof. Charles Smith, who is a great person and professor. Very lucky I had chances to serve as his TA for two semesters. I'd also like to acknowledge professors and staffs in mechanical engineering departments, including but not limited to Prof. Gary Harlow and Prof. Meng-Sang Chew.

To my fellow labmates and friends at Lehigh, I am very fortunate to have met you here. I would like to express my special thanks to Dr. Jifu Tan and Dr. Shunqiang Wang, who are my senior labmates as well as my good friends. They provided tremendous help in my Ph.D. study and so much joy in my life. Great thanks are also owed to my labmates

- Wentao Shi, Christopher Uhl (the amount of food he brought to us was beyond calculation, same as the joy), Doruk Yunus, Salman Sohrabi, Antony Thomas, Jia Hu, Junda Zheng, Yue Xiao, Lucas Lin, and Yiran Shao. I also appreciate the help and work from our talented undergraduate students, including but not limited to Steven Lee, Joachim Amoah, James Currie, Justin Landowne, and Geoffrey Andrews. I want to thank all my friends, and wish our friendship everlasting.

Finally, I would like to thank my beloved parents Lianke He and Yuping Wang, and my fiancée Di Feng for their consistent support. Together we shared all happy moments and pulled through all difficulties. I am the luckiest person to have them in my life.

Contents

List of Figures

Abstract

Developing advanced microfabrication technologies have been regarded as an important direction since many opportunities in technological innovations depend on the ability to fabricate novel structures in microscale. Commercially, high-throughput devices fabricated by cost-effective and efficient techniques that are suitable for mass production are highly desired. Scientifically, the ability to generate unconventional microstructures for improving the design and control experiments has attracted great interest of scientists. This dissertation presents five innovative techniques based on digital-lithographic fabrication to generate unconventional structures as better solutions in various applications. The techniques were firstly developed to advance the microfluidic areas, and then extended to 3D printing fields.

Firstly, a micro-patterning technology was developed to generate customizable micro-wavy patterned microfluidic devices. This method utilized the grayscale Gaussian distribution effect to model inaccuracies inherent in the polymerization process. An accurate pattern can be generated with customizable parameters (wavelength, amplitude, wave shape, pattern profile, and overall dimension), demonstrating the ability of this method to generate wavy patterns with precisely controlled features. Wavy patterns can be generated with the wavelength ranging from 12 μm to 2100 μm, and an amplitude-to-wavelength ratio as large as 300%. Microfluidic devices with pure wavy and wavy-herringbone patterns suitable for capture of circulating tumor cells were made as a demonstrative application. Secondly, build upon the first development, we developed a dual-projection lithography technique to fabricate microfluidic channels with circular and

elliptical cross sections. The method utilized two projecting systems to expose grayscale image face-to-face and simultaneously polymerize the photocurable material. The cross-sectional profiles of the fabricated microchannel were consistent with mathematical predictions and, therefore, demonstrate the capability of controlling the channel shapes precisely. Customized circular microchannel can be generated with complex features such as junctions, bifurcations, hierarchies, and gradually changed diameters. This method was capable of fabricating circular channels with a wide range of diameters (39 μm–2 mm) as well as elliptical channels with a major-to-minor axis ratio up to 600%. Microfluidic devices with circular cross sections suitable for particle analysis were made as a demonstrative application in nanoparticle binding and distribution within a mimetic blood vessel. Thirdly, we developed an in situ fabrication technology to generate controllable actuators through two-color inhibited lithography. The method utilized the light inhibition effect to selectively form an unpolymerized layer that prevents the adhesion between polymerized structures and microfluidic substrates. A novel material system and an optimized optical system were established to allow the simultaneous control of both lights. Magnetic nanoparticles were introduced in the photocurable materials and acoustically aligned. Thus, under magnetic field, remote and precise control of the rotation angle was achieved for a fabricated rotor structure.

Next, we further extended the digital-lithographic fabrication to additive manufacturing and developed two 3D printing technologies. The first technology was based on a scanning lithography that allowed UV projector to continuously cure resin while scanning over the build area. This approach can be regarded as a combination of both laser based 3D printing and DLP (Digital Light Processing) based 3D printing, adopting laser's

mobility and DLP's ability to exposure an area at once. To 3D print large objects, 3D models were sliced in to layer-by-layer "maps", which were ultrahigh-resolution images. Each "map" was further divided into sub-region images to fit the projector's resolution. During the movement of the projector, the sub-region images were dynamically exposed to the photocurable materials and synchronized with the scanning of the projector, causing a still exposure pattern to appear on the target build surface. Therefore, 3D printing of customized build volumes on a large-scale (greater than 1 m3) can be achieved with micro-scale features. The second 3D printing technology utilized an oxygen inhibited lithography approach to achieve continuous fabrication of three-dimensional objects. The oxygen inhibited the polymerization and creates an isolated layer, enabling ultra-high-speed printing with layer-less finish. The tensioned vat system and pressure controlled chamber enabled a close-loop control to provide robust solutions for printing objects with solid inner structures and large cross-sections. Unconventional structures with microscale features that can hardly be fabricated by other methods were generated rapidly.

With these developed microfabrication techniques, we expect the work to provide solutions for effectively generating features that can be extensively applied in various applications.

Chapter 1 : Introduction

1.1 Background and Motivation

Microfabrication can be defined as a process to fabricate physical structures in micrometer scales. It has been approximately 50 years since the field of micro-scale fabrication has been established. The technique was originally used in fabricating integrated circuits, but now has been widely applied in many areas of science and engineering. Over the last two decades, the development of microfabrication was mainly driven by the life science research and industries. Developing advanced microfabrication technologies have been regarded as an important direction since many opportunities in technological innovations depend on the ability to fabricate novel structures in microscale. Commercially, high-throughput devices fabricated by cost-effective and efficient techniques that are suitable for mass production are highly desired. Scientifically, the ability to generate unconventional microstructures for improving the design and control experiments has attracted great interest of scientists.

In particular, microfluidic applications in various scientific and industrial areas such as pharmaceutics[1], biomedical engineering[2], and micro-electro-mechanical systems (MEMS)[3] have great demand in high performance devices that request effective and precise fabrication technologies. For example, in diagnosing applications[4], biomedical microsystems with higher analytical performance, improved automation and control abilities, higher integration, greater sensitivity, improved safety, and reduced cost are expected to be achieved with more advanced microfabrication technologies.

On the other hand, the fabrication of large objects with intricate details also have increasingly demands. In biological and medical areas, devices with more complex control system and structures are expected to further facilitate the research work[5][6]. Large integrated system with microscale components, which allows more components and independents control operations to be embedded in a single device, will have greater potential in both industrial and scientific research fields due to the high-throughput capability. For example, a complex microfluidic logic circuit for arbitrarily controlling flows is composed of several pieces of small devices that are fabricated separately[7]. A fabrication technique that can fabricate all the components as an integration can solve the connection and alignment issues to improve the experimental accuracy.

Therefore, the continuous implementation and definition of novel fabrication techniques is key to advance the development of many scientific and industrial applications. A series of research projects in dissertation provides a few novel fabrication techniques. Before introducing that, we will begin with an overview of current microfabrication technologies. To provide a broad view of current technologies, the mainstream fabrication methods are divided into a few classifications, non-lithography, lithography, and 3D printing approaches, which are described in the following paragraph.

1.2 Non-lithography Based Microfabrication Technologies

Non-lithography methods were initially developed in 1990s. Micromachining in silicon was a popular technology and vastly used in fabricating integrated circuits and MEMs, and was further applied to fabricate microstructures on oxidized silicon and glass materials for biomedical and biological studies. High precision can be achieved from the micromachining on glass and silicon. However, the fabrication process is too complex,

time consuming and costly. At the beginning of the 21st century, other non-lithography microfabrication methods, with low cost and simple processes, have been developed by different researchers. Print and peel (PAP)[8] techniques are typical low cost methods to achieve fast and easy prototyping of microfluidic moulds. The master moulds are normally printed by laserjet or solid ink printer[9], or fabricated by Xurography[10], which utilizes a cutting plotter and adhesive vinyl films. On the other hand, PAP techniques have main limitations of the poor precisions and low resolution (70μm in printed master moulds), which cannot be used in research with high precision requirements. Instead, micromilling[11] is another non-lithography method based on CNC system to achieve less 30μm resolution. Structures with 5μm features can be possibly achieved under the clean room environment. Although high precision and small features can be provided from this technology, this approach has several disadvantages including complex process in tool alignment and easy breakage of the tools. Additionally, only those hard materials that will stand a certain temperature, such as thermoplastics and polymethyl methacrylate (PMMA), can be used for this approach. The other way to fabricate microstructures and microchannels is utilizing direct laser plotting technique[12]. A laser plotter uses effect of thermal degradation to engrave the material surface. This technique provides a simple and fast approach that can generate microchannels with widths less than 100μm[13] (10-20μm can be possibly generated by using ultra-short laser pulses). The laser plotter is also capable to fabricate on a wide range of materials, including polydimethylsiloxane (PDMS)[13]. Despite the advantages offered by this technology, it is only able to produce trapezoidal and close-to rectangular cross sections, which is considered as a big drawback.

1.3 Lithography Based Microfabrication Technologies

Another series of microfabrication technologies is based on lithography approach. Photolithography is a well-developed method in micropatterning and microfabrications[14]. This process requires a mask to be produced with a specific pattern, and then exposes ultraviolet light through the mask to generate patterns on the thin layer of the photoresist. Positive and negative photoresist are two typical kinds of materials in photolithography. During the developing process, the UV-exposed positive resist can be dissolved in the developer while the unexposed part remains, whereas the exposed areas of negative resist keep intact while the unexposed part is dissolved. Two other similar alternatives, electron-beam and X-ray, are considered in MEMS and nanofabrication due to the capability of achieving higher resolution. However, these methods have very high cost, limitations in fabricated structures, long lead time and the need for clean room. These limitations can postpone or terminate some research processes. As a result, soft lithography has become one of the most popular techniques in microfluidic fabrication[15]. Initially introduced by Whitesides' group[16], this technology basically composed of two major processes, pattern printing and replica moulding, as shown in Figure 1-1. The pattern printing process is based on photolithography on UV resin (normally SU8). The resin is spread on a flat surface with a desired thickness (via spin coating), exposed to the UV to form patterned structures and developed in a solvent to etch the unpolymerized parts. Then the elastomeric material (normally PDMS) is poured into the mold and heated to form hardened structures, and then separated from the mould. The separated elastomeric part will be plasma treated in order to bound with substrates (normally glass or PDMS) or another part. Depending on the applications, sometimes holes will be punched as inputs and outputs. The soft lithography technique enables the fabrication of precise and complex

microstructures. On the other hand, the soft lithography approach is still limited by the capability of fabricating cross-section geometry, three-dimensional objects, and structures with large aspect ratios. The entire fabrication process is proper for prototyping rather than volume productions, which limits the extensive use of this technology, especially in industrial applications.

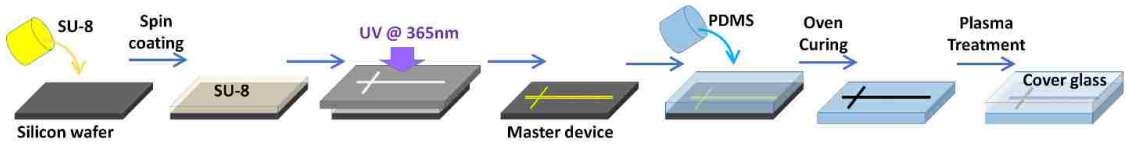

Figure 1-1 The fabrication process of a microfluidic device based on soft lithography technology.

1.4 Additive Manufacturing (3D Printing) Based Microfabrication Technologies

Additive manufacturing or 3D printing has attracted significant interest and has been regarded as the revolutionary technologies in manufacturing. 3D printing is a collective name of various technologies that can directly fabricate three-dimensional objects. 3D printers that are capable of generating structures ranging from microns to centimeters have begun challenging the traditional microfabrication method. 3D printing provides new opportunities in the microfabrication field since three dimensional structures are fabricated in a way that was not previously possible. Meanwhile, the rapid fabrication speed of a testing model for proof of concept is another feature of 3D printing. Compared with traditional microfabrication methods, 3D printing can significantly save the lead time. Among all the 3D printing technologies, inkjet, stereolithography(SLA), and two-photon lithography stand out in microfabrication field because of the capabilities of fabricating microscale features.

Inkjet based 3D printing typically generates pulses either thermally or piezoelectrically to eject ink droplets[17], [18]. The thermal one creates vapor bubbles by heating the ink and jets droplet. The piezo one uses the deformation of piezoelectric element to generate acoustic pulses, pushing the ink droplet out of the nozzle. This printing method generally utilizes printing head with multi-channels and sprays adhesive droplets onto the build platform. Once the first layer is printed, the build platform repositions to leave space for the next layer. High resolution inkjet 3D printing can theoretically provide a resolution ~40 μm. Capable of printing multi-materials is also an advantage over other microfabrication methods. SLA 3D printing builds objects through spatially controlled polymerization of a photocurable resin[19], [20]. This method generally uses either a laser or a digital light projector to expose UV light to the liquid material. Similar to inkjet printing, in most general SLA 3D printing approaches, the objects are built in a layer-by-layer manner, and the build platform needs to be repositioned for each layer. The highest resolution that can be provided by the SLA method can be around 30-50μm. Many of the printers have demonstrated the capabilities in microfluidic fields[21]–[23]. Two-photon lithography is another 3D printing based tool for micro/nano-fabrication[24]. It uses focused femtosecond laser pulses to cure the photosensitive resin. The molecule simultaneously absorbs two photons and induces polymerization. Most of the materials designed for two-photon lithography are specialized for lithographic applications including both negative and positive photoresists[25], [26]. Two-photons lithography can generate features with a resolution of 120 nm, which is a milestone for 3D printing[27]. Thus, this technology has great potential to be used in microfabrication, especially in microfluidic fields[28], [29].

1.5 Limitations of Current Technologies and Research Objectives

Although the prior arts have offered various kinds of microfabrication technologies with unique features, many research and industrial applications that require high performance device and unconventional microstructures still cannot be well satisfied. The main obstacles are the geometric limitations, high fabrication cost, low customizability and complex processes. Micromachining technique has high precision on glass and silicon, but the fabrication process is too complex, time consuming and costly. PAP has main limitations of the poor precisions and low resolution (70μm in printed master moulds), which cannot be used in research with high precision requirements. CNC based micro-milling can achieve high precision and small features, but disadvantages including complex process in tool alignment and easy breakage of the tools. Additionally, only those hard materials that will stand a certain temperature, such as thermoplastics and polymethyl methacrylate (PMMA), can be used for this approach. Laser plotters is only able to produce trapezoidal and close-to rectangular cross sections, which is considered as a big drawback. The traditional stereolithography, electron-beam and X-ray methods have very high cost, limitations in fabricated structures, long lead time and the need for clean room. These limitations can postpone or terminate some research processes. The soft lithography approach is still limited by the capability of fabricating cross-section geometry, three-dimensional objects, and structures with large aspect ratios. The entire fabrication process is proper for prototyping rather than volume productions, which limits the extensive use of this technology, especially in industrial applications. The additive manufacturing based technologies offer rapid fabrication processes. However, limitations still exist for all these approaches. Since conventional 3D printing is a layer-by-layer process, the surface of the

printed structures won't be smooth enough in microscale, which creates problems for research studies and applications that require high surface quality. Meanwhile, printing large-scale object with integrated microscale features is always a problem for 3D printing field. With the extensive adoption of 3D printing, a cost-effective and fast printing method that can fabricate large-scale object as well as intricate details is highly desired.

1.6 Dissertation Layout

To further advance microfabrication technologies, the original research introduced in dissertation aims to develop a series of novel methods to fabricate unconventional microstructures in high customizability and efficiency with lower cost. The research works are described in this dissertation and organized based on the following structure:

Chapter 2 discusses the development of a novel method to more effectively fabricate micro-wavy patterns with high complexity and customizability. This method combines the direct image lithography and grayscale effect to fabricated three dimensional microstructures with complex patterns and smooth surfaces. A computational model of the grayscale polymerization process was established to predict and guide fabrication results. Although extensive studies have been pursued on the micro-patterning technologies, none of them can provide a good combination of low cost, complex structures, customizability, simple processes and predictable results. This method is expected to serve as a versatile tool in various applications, such as generating wavy patterns for capturing circulating tumor cells (CTCs).

Chapter 3 introduces the development of an efficient and cost-effective technology to fabricate microfluidic channels with complex networks as well as circular and elliptical cross-sections. The method utilizes two projection systems to expose grayscale image face-

to-face and simultaneously polymerize the photocurable materials. An improved computational model for this dual-projection lithography method will be established to predict and guide fabrication results. Even though many researchers have developed methods to fabricate circular channels, the geometry limitations, fabrication cost and efficiency of current technologies limit the uses of the fabricated microfluidic devices. This method is expected to provide great convenience for researchers in microfluidic areas and improve scientific experimentation for biological and medical applications, especially in nanomedicine and therapeutic studies.

Chapter 4 introduces the development of a novel method for in situ generating controllable microfluidic actuators. The method utilizes the light inhibition effect to form an unpolymerized layer that prevents the adhesion between polymerized structures and microfluidic substrates. This approach combines an initiating light with a wavelength of 473nm to polymerize the photocurable material and an inhibiting light with a wavelength of 364nm to prevent the polymerization. An optimized optical system will be established to allow the simultaneous control of both lights. Magnetic nanoparticles are introduced in the photocurable materials and acoustically aligned into desired patterns. Remote control of the actuating can be achieved under magnetic field.

Chapter 5 presents an additive manufacturing method to fabricate large-scale three-dimensional objects with intricate structures. To 3D print large objects, 3D models are sliced in to layer-by-layer “maps”, which are ultrahigh-resolution images. Each “map” is further divided into sub-region images to fit the projector’s resolution. During the movement of the projector, the sub-region images are dynamically exposed to the photocurable materials and synchronized with the scanning of the projector, causing a still

exposure pattern to appear on the target build surface. Therefore, large objects with delicate details can be printed layer-by-layer. As such, customized build volumes on a large-scale (greater than 1 m3) can be achieved with micro-scale features. With the capabilities of large-scale fabrication and bulk production, the technology presented in this project is expected to provide ideal solutions in various industrial applications.

Chapter 6 presents a continuous 3D printing technology for high-quality and unconventional 3D structures. This technology utilizes the oxygen inhibition effect to create an isolated layer, enabling ultra-high-speed fabrication of 3D object with improved surface qualities. Parts with complex geometries and intricate details can be generated in very short time, which can significantly reduce the lead time of urgent need or customized products. Through the close-loop control of film and air chamber systems, printing processes are dynamically changed. 3D objects with both solid inner structures and porous structures can be precisely fabricated. Therefore, it has the great potential to be applied in varies industries.

Chapter 7 is a summary of the dissertation and discusses the future work and trends of the presented research.

These presented technologies target on fabricating those microstructures that are very difficult or incapable to be produced by the current methods. Better solutions in various applications are expected to be brought in by these new techniques.

Chapter 2 : Generating Wavy-Patterned Microstructures through Grayscale Direct Image Lithography

2.1 Introduction

The development of practical and cost-effective methods of producing patterned microstructures is currently of great interest, especially in the field of surface studies[30], cell adhesion[31], and microfluidic[32] . The wavy pattern is highly desirable features, as it is eminently useful for biological applications[33],[34] and for adjusting surface properties such as adhesion[35],[36], friction[35], and hydrophobicity[37]. A standard technique to create micro-wavy features is depositing thin metal films onto PDMS substrates with some degree of thermally-induced pre-strain[38]. Releasing of the strain is capable of generating wavy patterns with a uniform wavelength. Success has also been found in pre-straining substrates using mechanical force. Studies by Yang's group found that a sequential mechanical stretching and unstretching of an oxidized PDMS membrane was sufficient to induce a highly ordered, uniform herringbone pattern[37] (Figure 2-1(a)). However, methods which rely on pre-straining a substrate are inherently limited in the wave shapes, dimensions, and diversity of the pattern profiles. In particular, the sequential and unequal biaxial stretching method cannot produce features with a wavelength greater than 50 μm, which creates a clear barrier for making large-scale wavy patterns[37]. In addition, the ratio of amplitude to wavelength reaches a limit at approximately 30%, greatly restricting the wave shapes which can be created. Furthermore, there is a more obvious

limitation in that only select profiles, namely wavy and wavy-herringbone patterns, can be produced by the pre-strain method.

The standard method of applying thin metal films is also incapable of producing a pattern with a wavelength beyond the range of 20-50 μm[38]. This metal deposition method also has significant shortcomings in cost and complexity, as it typically uses electron beam evaporation to deposit 50-nm-thick layers of gold with a 5-nm adhesion interlayer of titanium or chromium, requiring a complex fabrication process and high material cost. There are a few other methods of creating micro-wavy patterns based on the lithography approach. Crosby's group has developed a method of generating wrinkled patterns in UV-cured polymer films, using a diffusion induced oxygen concentration gradient to inhibit polymerization during UV-curing and form an uncured liquid layer that spontaneously swells the film[39]. This approach has generated wrinkle patterns with controllable wavelength and amplitude, distribution of the wavy structures is random. Thus, the method is incapable of creating a micro-wavy pattern with specific profiles, such as wavy-herringbone patterns.

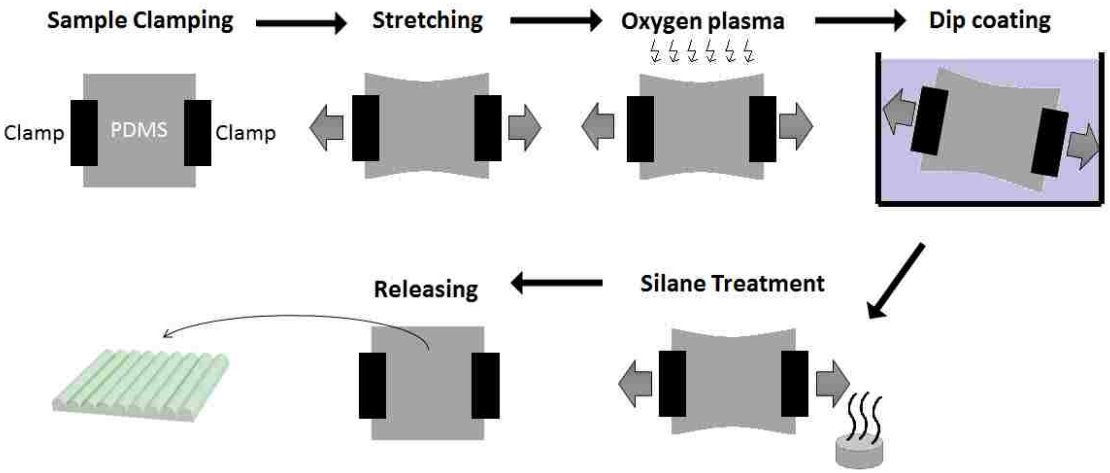

Figure 2-1 Wavy pattern generated by sequential stretching and unstretching of oxidized PDMS membranes (Yang's group).

As an alternative, the grayscale lithography method allows for the rapid fabrication of three-dimensional microstructures with greatly reduced complexity[40]–[42]. Whitesides' group used a grayscale mask in photolithography to create microlens[43]. However, generating the photomask is time consuming and not cost-effective, making it difficult and impractical to customize the patterns for a specific application.

Another method relies upon the use of digital micro-mirror devices (DMD), which can adjust the hue of each pixel in an image; this is known as Digital Light Processing (DLP). Using a standard grayscale color mapping, 256 different light levels are thus possible, creating a highly capable curing device when the DMD chip is combined with an appropriate light source[44]. As such, an image with multiple grayscale levels can be used to directly create three-dimensional features in a single exposure. Park's group achieved success in fabricating three-dimensional structures using this type of mask-free lithography method[45]. Kwon's group utilized a similar approach as an in situ polymerization technique to generate gradational micropatterning[46]. His group also developed a method that utilizes the light overlap to fabricate microstructures as polymer microtaggants for anti-counterfeiting of drugs.[47] However, to generate precisely customizable microstructures, both the light distortion effects and mathematical models need to be considered comprehensively to predict intended results.

Therefore, a direct image lithography technique was developed in this project. This method used grayscale mapping in conjunction with a mathematical model to create a wavy pattern with diverse geometries in a precise and controllable manner.

2.2 Method and Materials

2.2.1 Analysis of UV induced polymerization

UV curing is a chain-grow polymerization process including initiation, propagation, and termination. The UV light absorbed by the photoinitiator inside the photosensitive materials generates free radicals to induce polymerization and cross-linking. Based on the Jacobs model, the photosensitive material in a liquid form is cured only when the absorbed energy has reached the exposure threshold in polymerization. Meanwhile, Beer Lambert's Law shows the relation between exposed energy, curing depth, and the penetration depth of the photosensitive material, which makes the polymerization parameters controllable. In this method, a digital light fabrication approach that utilizes the UV induced polymerization is developed to achieve a single step fabrication of complex channels with circular cross-section. A key element in this approach is the digital micro-mirror device (DMD), which has an array of independently rotatable micro-mirrors can reflect the UV light and project a pattern to cure the photosensitive material. Each individual micro-mirror on the DMD controls a single pixel on the exposure image while the projected pixel size determines the theoretical resolution. In an ideal situation during the photolithography process, the energy of a projected pixel is uniformly distributed in the target area without affecting the surrounding areas (Figure 2-2(a)). In actual cases, the distribution of each single pixel's energy forms a Gaussian distribution and light is diffused to the surrounding region due to optical error (Figure 2-2(b)). Therefore, the polymerization situation of a pixel-sized area is determined by lights that are projected directly to the region as well as to the nearby regions.

Under a certain material and optical system, the curing depth is only determined by the exposure time and light intensity. The grayscale effect is introduced to control the light

intensity by projecting an exposure image with a grayscale value for each pixel. The grayscale value has a range from 0 to 255 with weakest intensity in black (grayscale value 0) and strongest intensity in white (grayscale value 255). The DMD will tune the rotating frequency of each micro-mirror to display a grayscale image with an accurate control of the grayscale level for each pixel. Under the same exposure time, projecting light with higher grayscale value will cause greater polymerization depth while a grayscale value less than a threshold level will not lead to any curing of the material. Therefore, the grayscale method can generate a unique curing depth for each pixel under a single exposure. The grayscale exposure can be combined with the Gaussian effect to create three dimensional objects with smoothly curved surfaces. Mathematical models can help to describe of the cross-section view of the cured objects. (Cross-section is parallel to the projecting light direction and perpendicular to the focus plane of the exposure pattern).

If multiple pixels are projected in a column array, the overall light energy of a certain point is contributed by directly projected light as well as the light diffused from nearby regions. When several white pixels (grayscale value 255) are projected in a row, the mathematical model is expected to predict a flat top surface. The overlapped energy from the bottom part makes up the energy gaps and the polymerization depths for all pixels are remained the same. If different grayscale values are properly introduced in the exposure image, wavy shapes can be formed. In this model, the wavelength is determined by the number of pixels, while the amplitude is determined by the difference between the maximum and minimum grayscale value in each wave. The shape of the wave can be specified by using a particular combination of grayscale values.

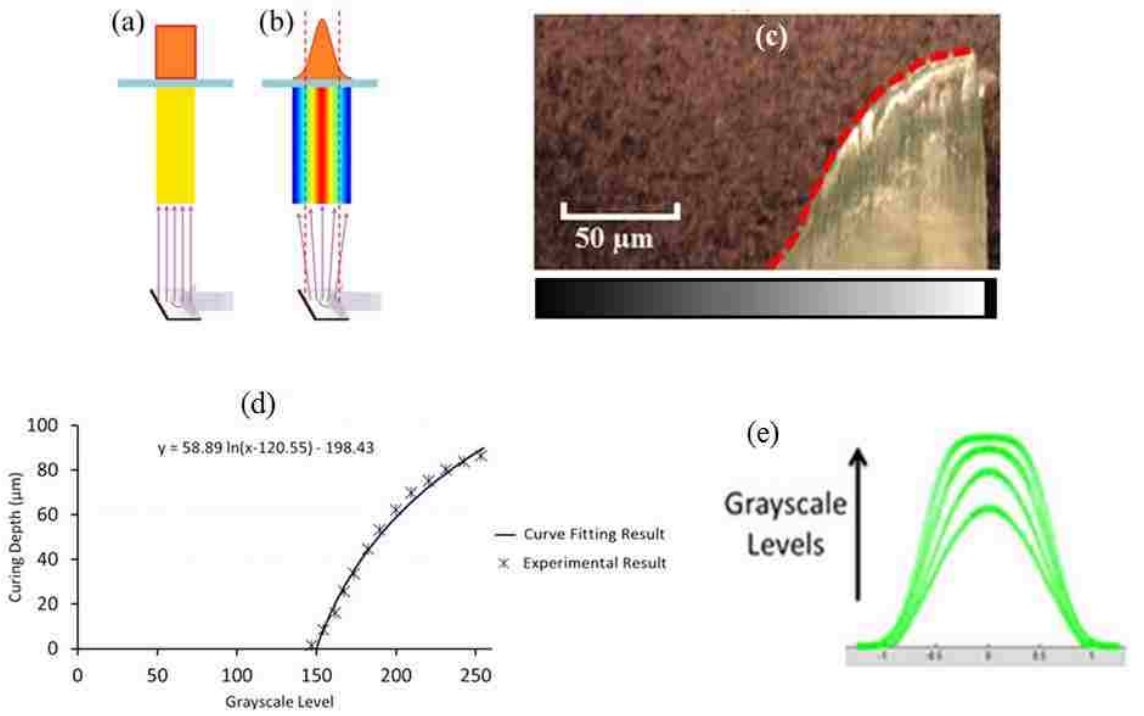

Figure 2-2 (a)Theoretical curing model of photocurable resin under the UV exposure of one pixel's area; (b)Actual curing model of photocurable resin under the UV exposure of one pixel's area; (c)Profile of photocurable resin cured under the exposure of grayscale gradient; (d) Curve fitting of the experimental result (e) Variation of single pixel curing models at increased grayscale levels.

2.2.2 Establishment of the grayscale mathematical model

To establish the relation between grayscale level and polymerization depth an exposure image with grayscale gradient from 0 to 255 is projected to the photocurable material. The polymerized object with the corresponding grayscale value is shown in Figure 2-2(c). A grayscale value under 150 will not lead to any curing while increasing the grayscale value (greater than 150) will lead to a greater the polymerization depth. Then the profile of the polymerized object is measured by a contact profilometer with stylus force set to 0.03 milligrams. Based on the experimental result (Figure 2-2(d)), the relation of grayscale level G and polymerization depth D_1 can be expressed as:

$$D_1 = k_1 \ln(G - k_2) - k_3 \quad (1)$$

where k_1, k_2, and k_3 are 58.89, 120.55 and 198.43, respectively. The values of k_1, k_2, and k_3 are dependent on the type of photocurable material and the exposure time. This equation provides a method of controlling the curing thickness by choosing proper grayscale values. Based on the optical system and photocurable material used in this method, the curing threshold grayscale value is 150. An image with grayscale level less than 150 will not polymerize the liquid resin regardless of how long the exposure time is.

In the mathematical model, a row of DMD micro-mirrors has been selected to study the curing shape generated under different grayscale levels. Side view of a single pixel's curing shape with increasing of grayscale level is illustrated in Figure 2-2(e). As the grayscale level increases, the curing depth increases and the top part of the cured shape gets flatter. A curing model of a single white pixel with grayscale value of 255 can be expressed as:

$$D_w = \sum_{i=0}^{n} \frac{k_0}{\sigma\sqrt{2\pi}} e^{\frac{-(x+\frac{i}{n})^2}{2\sigma^2}} \quad 2)$$

where D_w is the curing depth x is the horizontal coordinate position, and k_0 is a factor of proportionality related with the material system and exposure time. In the current system setup, the values of k_0, σ and n are 2.87, 0.15 and 10, respectively.

In Figure 2-3(a), a single wave is formed by five adjacent grayscale pixels. In Figure 2-3(b-d), three series of waves with various wavelengths and shapes are formed by introducing multiple grayscale pixels and values. Figure 2-3(e) shows a simulation of seven groups of wave shapes with different pixel numbers and grayscale values that decrease from the peak to the bottom.

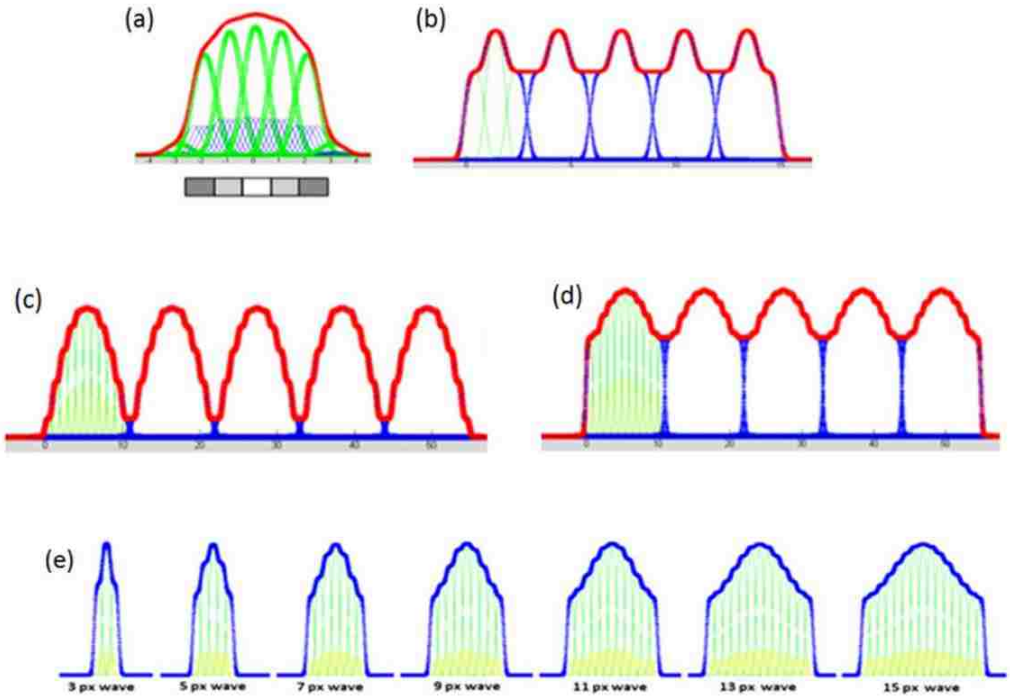

Figure 2-3 (a) The curing model of a single wave containing five grayscale pixels; (b–d) Curing models of wave series containing multiple grayscale pixels in each wave. The numbers of grayscale pixels in each wave are 3 in (b), 9 in (c) and 11 in (d), respectively; (e) Single wave curing models according to different pixel numbers in each wave.

2.2.3 Automatic Generation of Grayscale Exposure Images

To create an accurate grayscale image for exposure, a pattern generation program is developed. As shown in Figure 2-4(a) and Figure 2-4(b), a pattern of 2D lines is drawn using CAD software and saved as a .dxf format file. The distance between two lines determines the wavelength of the micro-features - the pattern generation code reads the .dxf file and creates a grayscale exposure image which is used in the lithography process to form the desired features. The exposure image can be created by inputting different combinations of grayscale values for different lines in the CAD file. Once the target wavelength and wave shape are decided, the mathematical model can provide grayscale values to be input into the pattern generation code. The output image, such as (a) CAD

drawings of uniformly distributed herringbone lines; (b) CAD drawings of a column of lines with the gradient determined by the gap distance; (c,d) The grayscale exposure image generated from drawing (a,b), respectively.(c) and Figure 2-4(d) can be directly used for exposure through the projecting system. This pattern generation program can generate complex grayscale images for a variety of desired shapes.

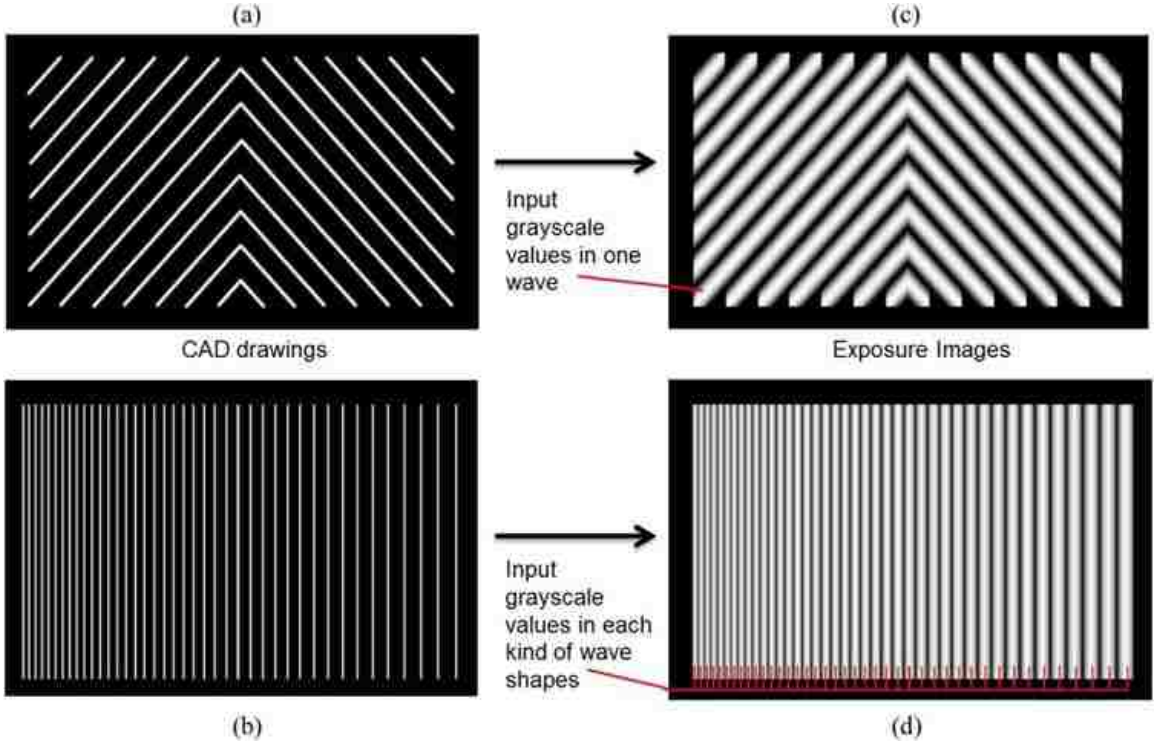

Figure 2-4 (a) CAD drawings of uniformly distributed herringbone lines; (b) CAD drawings of a column of lines with the gradient determined by the gap distance; (c,d) The grayscale exposure image generated from drawing (a,b), respectively.

2.2.4 Development of the Fabrication System

A micro-pattern fabrication system has been established to produce the micro-wavy patterns. This system has an optical platform including a light source, condensing lens, shaping lens, a DMD chip (digital micro-mirror device, SXGA+, Texas Instruments, USA), projection lens, and front lens as shown in Figure 2-5. The optical projection system is

designed for projecting grayscale images, and the SXGA+ DMD chip is capable of instantaneous exposure (with a minimum exposure time of 10^{-4}second). The front lens system is installed to fix the image distortion as well as adjust the printing resolution. A xenon lamp is used as the light source with a main wavelength ranges from 330nm to 580 nm. However, only the UV portion of the projection spectrum (ranging from 330nm to 390nm wavelength) is effective in the polymerization process, because the reaction range of the photocurable resin is less than 390nm. The optical system can reduce size of pixels projected on the glass substrate to a minimum size of 10μm, which determines the minimum wavelength of the wavy-pattern that can be fabricated with the apparatus.

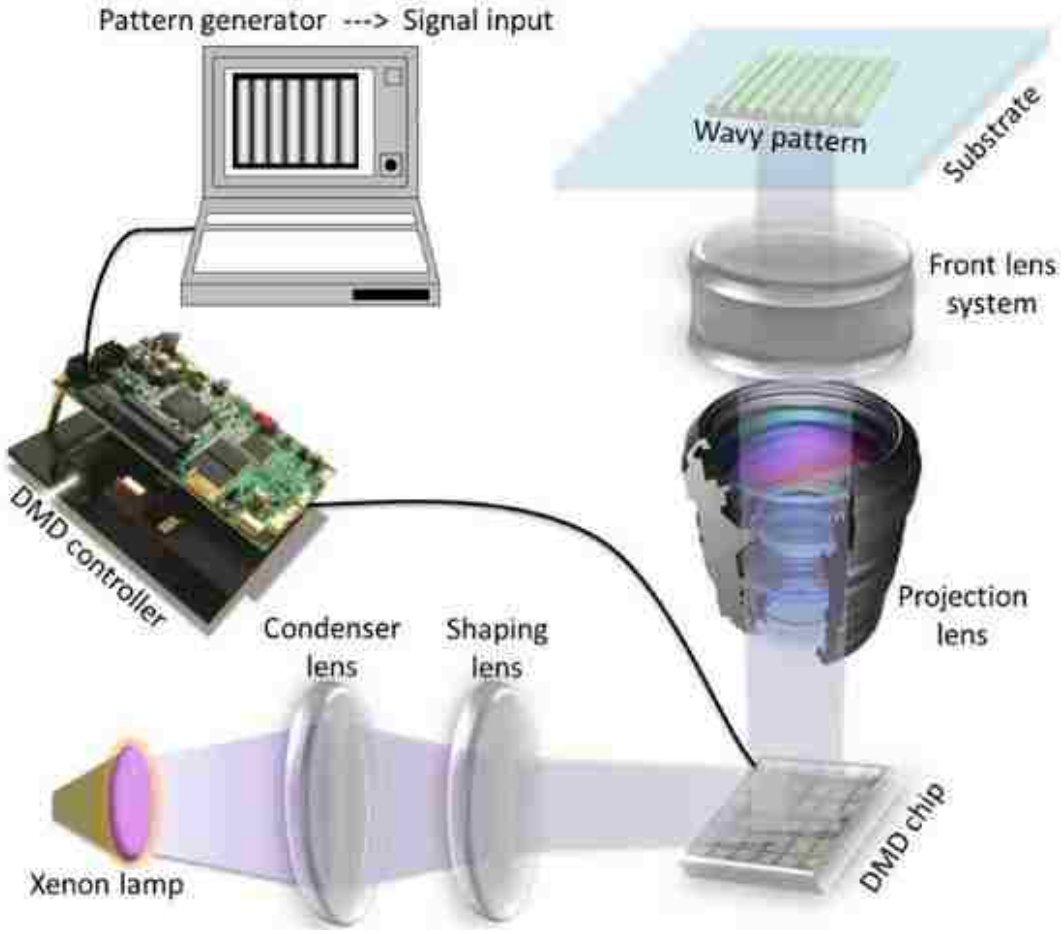

Figure 2-5 The schematic diagram of the wavy pattern projection system.

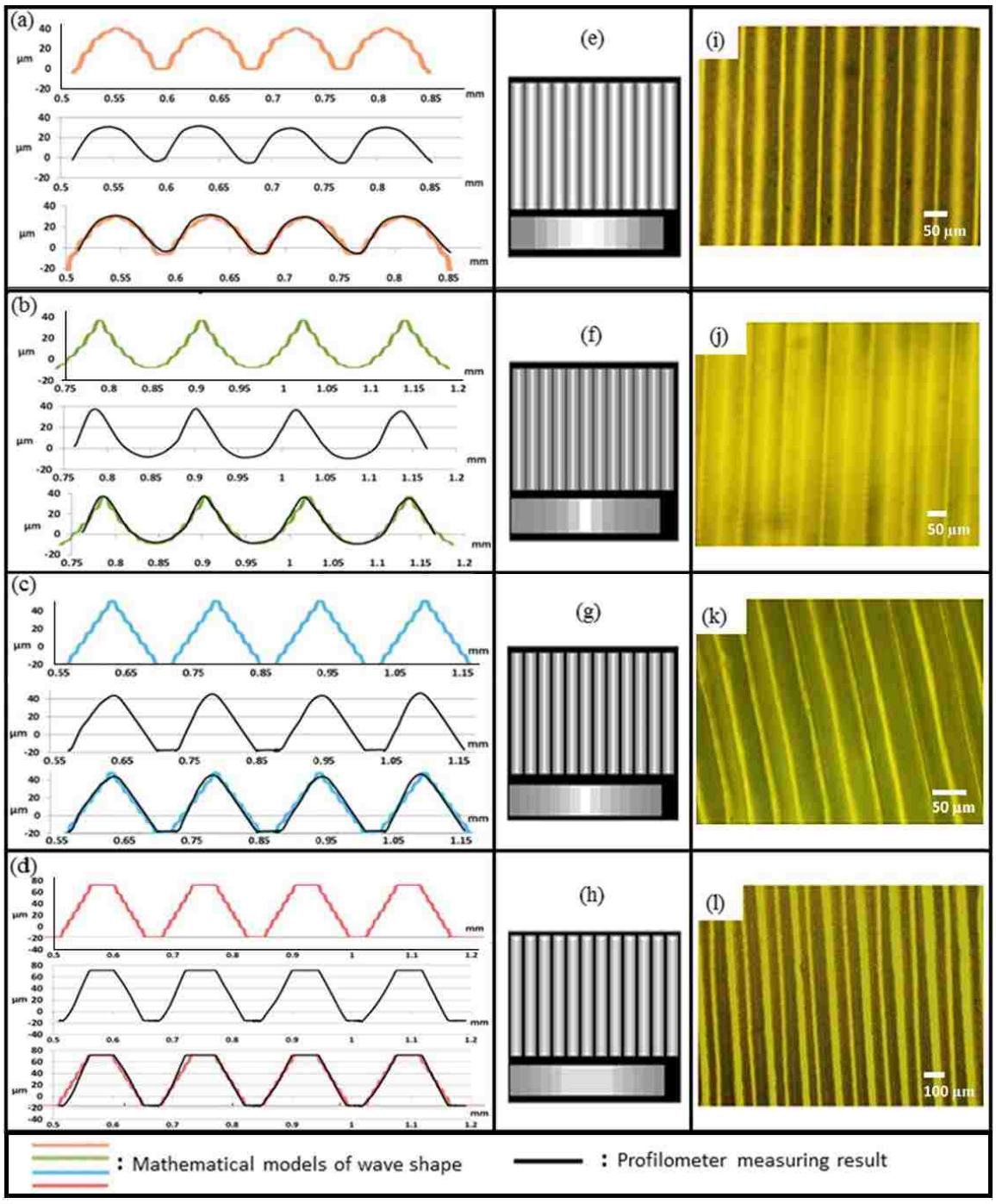

Figure 2-6 Mathematical curing models, profilometer measurement results, and the comparison between the exposure images in grayscale (e–h) and the digital microscope images of fabricated wavy patterns (i–l).

2.3 Results and Analysis

2.3.1 Comparison between Mathematical Models and Fabricated Profiles

To ensure the fabricated wave shape matches with the mathematical simulation, the wavy pattern is measured and compared with the theoretical result. A contact profilometer is used to obtain the profile of the fabricated micro-wavy patterns. After considering the surface properties of the material, the stylus force in the profilometer was set to the minimum value of to 0.03 milligrams. Four types of wavy pattern – semi-sinusoidal wave, inverse semi-sinusoidal wave, triangular wave and trapezoidal wave - were selected for testing purposes. Figure 2-6(a-d) show curves in four groups; each group includes the simulated curve based on mathematical model (top), the measured curing shape (center), and a comparison plot (bottom). The grayscale exposure images are shown in Figure 2-6(e-h). The digital microscope images of the corresponding wavy pattern are given in Figure 2-6(i-l). All of the wavy features shown in Figure 2-6 illustrate good agreement between the mathematical simulation and the actual surface measurements. Therefore, the established mathematical model and the corresponding grayscale exposure image can be used to accurately create a desired wavy pattern.

2.3.2 Characterization of Fabrication Parameters

The current experimental setup is capable of generating wavy patterns with wavelengths ranging from 12 μm (Figure 2-7(a)) to 2100 μm (Figure 2-7(d)). Wavy patterns with a wavelength within this range, such as 50 μm (Figure 2-7(c)), can be fabricated based on the current experimental setup. Wavy patterns of even larger wavelength could be achieved by modifying the optic system to adjust the projected pixel size. The ratio of the amplitude to wavelength has an approximate upper limit of 300%,

while most common method has an approximate 30% ratio limitation[37]. This method provides an easy way to fabricate three-dimensional wavy structures according to a customizable 2D patterns, such as herringbone (Figure 2-7(b)), and concentric circles (Figure 2-7(g-h)). Wavy patterns with different wavelengths can be fabricated simultaneously, such as a wavy pattern with a gradient of wavelength (Figure 2-7(e)). A customized exposure pattern for any profile can be created by simply making CAD drawings and selecting the target wave shape through numerical modeling. The UV curing process takes less than 20 seconds, which speeds up the fabrication process significantly compared to existing methods. The entire fabrication process -from a preliminary sketch to a ready-to-use micro-feature device can be accomplished in less than 30 minutes. Features generated using this method can be further embedded into microfluidic devices for more extensive applications. Our polymerized photocurable material is appropriate for FDTS-treatment, which facilitates the replication and separation of the PDMS molding (Figure 2-7(i)). As such, a completely customized microfluidic device with wavy patterns (Figure 2-7(f)) can be created within a few hours without access to clean room or commercial photolithography equipment using this method.

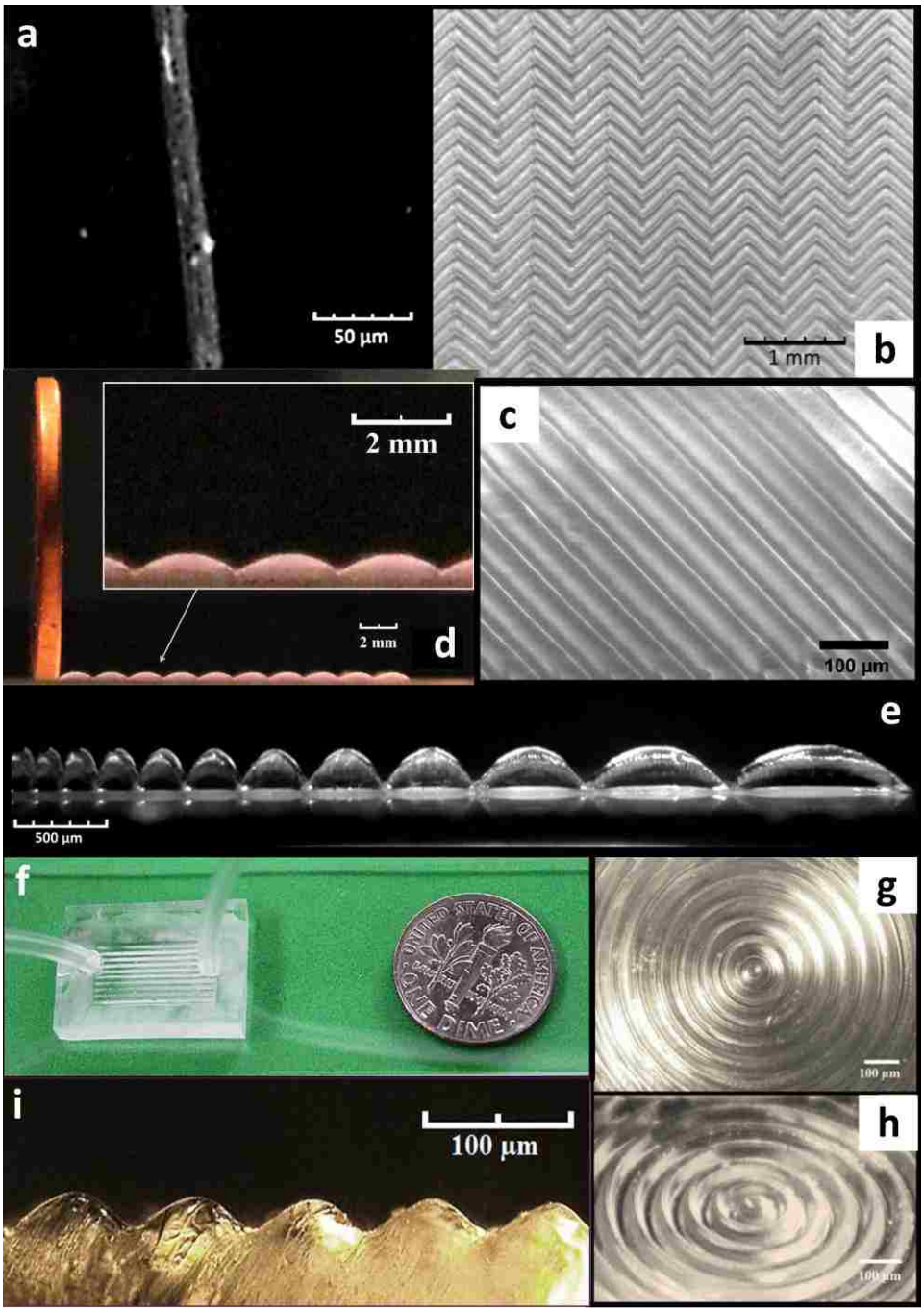

Figure 2-7 (a) The digital microscope image of a single wave; (b) The microscope image of the fabricated wavy-herringbone pattern; (c) The scanning electron microscopy image of the fabricated wavy-pattern with a wavelength of 50 µm; (d) Image of the wavy pattern with a wavelength of 2100 µm (Comparing with a penny in thickness of 1.52mm); (e) Microscope image of the wavy pattern with the increasing gradient of the wavelength (Ratio of the gradient change is 120%); (f) A microfluidic device with wavy patterns. The digital microscope image of the fabricated wavy concentric circles patterns in (g) top view and (h) oblique view, respectively; (i)The digital microscope image of the wavy pattern on PDMS after replication (Side view).

2.3.3 Application: Cell Capture Test

To demonstrate a potential application for this micro-feature fabrication technique, microfluidic devices with pure wavy and wavy-herringbone patterns were made to capture circulating tumor cells (CTCs). In the recent decade, microfluidic devices have been widely used for CTC detection, as summarized in several comprehensive review papers [48], [49]. In our lab, a microfluidic device with integrated with wavy-herringbone patterns has been developed for CTC isolation with highly efficient and selectivity. With the advantage of flexible design and short processing time, the mask-free grayscale lithography method fits the need of a vast array of varying designs for CTC detection. In the section below, the application of a wavy-herringbone pattern printed by grayscale method in CTC detection has been described.

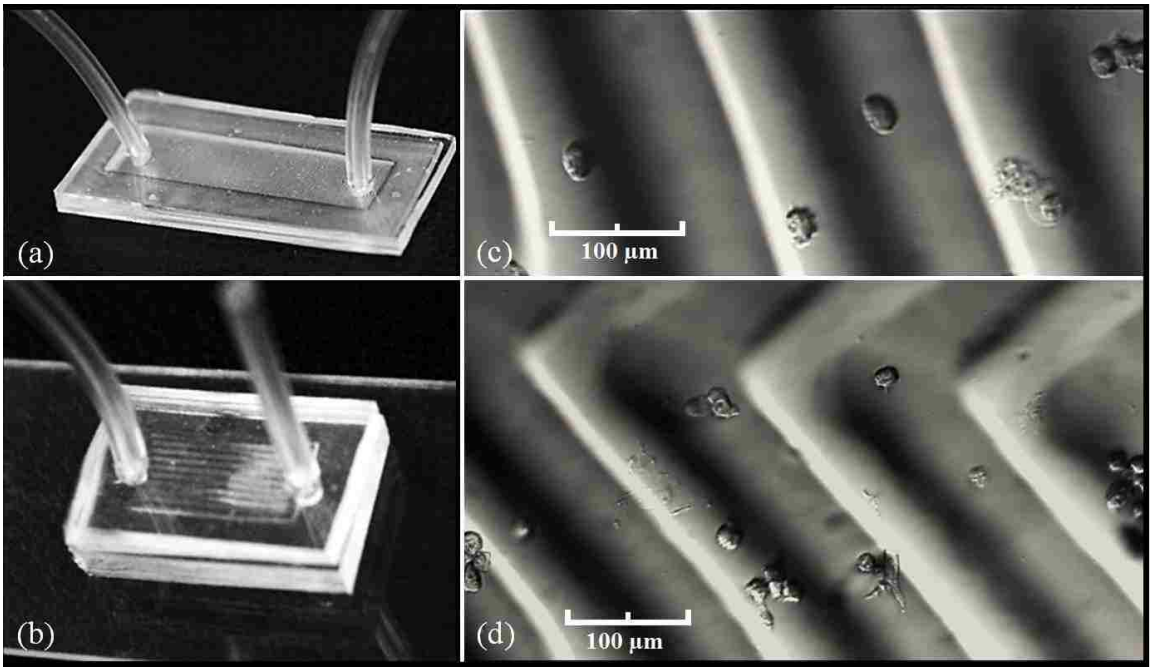

Figure 2-8 Microfluidic devices with (a) pure wavy pattern and (b) wavy-herringbone pattern, respectively. Microscope image of captured CTCs in microfluidic devices with (c) pure wavy pattern and (d) wavy-herringbone pattern, respectively.

HCT-116 cells were selected as the target CTCs for the microfluidic test. Cells were cultured with McCoy's 5a supplemented with 10% fetal bovine serum (FBS) and 1% Penicillin/Streptomycin. Incubation was obtained at 37 °C in 5% CO2 with media refreshed every 2-3 days. Before microfluidic tests, CTCs were detached from the flask through 5 minutes' incubation in 0.05% Trysin-0.53 mM EDTA. Cells were then diluted in 4 mg/ml alginated PBS solution with a concentration around 10^5/ml.

A standard protocol for coating anti-EpCAM was adopted to functionalize the microfluidic chip[50]. Before the cell flow test, the device was incubated with 5% BSA solution for 30 minutes and then flushed with PBS solution. Cell solution was then injected into the microfluidic chip under a certain flow rate through a syringe pump (Harvard Apparatus). After 5 minutes' flow at a rate of 2 ml/hr, PBS solution was used to flush out all free cells at 2 ml/hr. Both regular microscope images and fluorescent images DAPI staining images were used to identify if all captured objects were CTCs.

Figure 2-8(a) and (b) illustrate the flow system. The printed device is the typical size of a microfluidic device. Distributions of CTCs after the flow test in our pure wavy and wavy-herringbone patterns are shown in Figure 2-8(c) and (d), respectively. Due to the vortex induced in the microfluidic device, CTCs are captured both in the ridge and trough sections on the patterns.

Compared to previous methods in generating wavy patterns for CTC capture applications, this fabrication technique shows advantages of fast and precisely tuning the geometry parameters, as it is essential in determining the optimized settings of the CTC capture. In addition, the wavelength usually exceeds 100 μm in optimized CTC capture work[51],[52]. The method presented in this project is capable of fabricating wavy patterns

with a wavelength greater than 100 μm, which cannot be achieved by some standard techniques[37],[38].

2.4 Experimental Setups

The first step in fabrication of micro-wavy patterns using this method is to adjust the top surface of the glass substrate to the focus level of the optical projecting system. Then transparent photocurable resin is poured inside the substrate container. During the pattern exposure process, the exposed part of the resin is cured and will adhere to the bottom glass substrate. After exposure, the glass substrate, containing the printed pattern and any uncured resin, is immersed into acetone to develop for 15 minutes. Isopropyl Alcohol 99% can also serve as the developer, but it takes a longer time to dissolve the uncured resin (30 -45 minutes) and is unable to completely remove uncured resin if the wavelength of the features is particularly small. The substrate is then taken out of the acetone and dried off completely. A post-curing process uses a strong UV light source with a wavelength of 365 nm to further harden the polymerized patterns. The post-curing device in this experimental setup is an OmniCure s1500 that is capable of radiating 365nm-wavelength UV light with high intensity irradiance of 23W/cm^2.

To make a microfluidic device by replicating the fabricated features with PDMS, the pattern surface is oxygen plasma treated and coated with a layer of 1H,1H,2H,2H-Perfluorodecyltrichlorosilane (FDTS) (Alfa Aesar) to make it hydrophobic. PDMS devices are then replicated from the FDTS-treated substrates and assembled into an integrated microfluidic chip. If the target pattern is the inverse shape of the exposure pattern, only one PDMS replication process is necessary. If the target pattern is the same as the exposure

pattern, the final PDMS device needs to be formed from the PDMS substrate which has in turn been formed from the original device produced by the lithography process.

2.5 Conclusions

This study provides a method of generating highly customizable, precisely controlled micro-wavy patterns. Compared with current approaches[37],[38],[39], this method is capable of generating patterns with much wider range of wavelengths (12μm to 2100μm) and higher amplitude-to-wavelength ratio (up to 300%). Furthermore, since this method does not require a clean room or expensive lithography equipment, it brings not only high efficiency but great convenience and low cost to the fabrication of lab-on-a-chip devices with complex patterns. This grayscale lithography approach of generating surface patterns can also be developed as a versatile tool in surface studies. To achieve wavy-patterns with a wavelength shorter than 10μm, more precise optical systems need to be introduced to reduce the optical interference of the light reflected from the DMD micro-mirrors.

Chapter 3 : Fabricating Circular Microfluidic Channels through Dual-Projection Lithography

3.1 Introduction

Fabrication of microfluidic devices with complex microchannel structures is essential for many areas such as proteomics[53], tissue engineering[54], optics[55], drug tests[56] and disease diagnostics[57]. The prospect of accurate volume and time control in microfluidic devices allows for better mimicking especially for biological systems. Several devices were fabricated to mimic microvascular systems[58]–[60]. Currently, the majority of these microfluidic devices are produced by photolithography. However the current photolithography methods are only capable of generating rectangular cross-sections[16]. During replication of biological and biochemical systems, the cross-section of flow channel has a significant effect on the results[61]. For example, the differentiation state of luminal endothelial cells is affected by shear stress[62] which is directly related with the cross-section of the channel. Circular cross-sections generate a uniform stress distribution at the boundaries, while rectangular cross-sections generate an uneven distribution. As a result, rectangular cross-section creates unrealistic replications of luminal endothelial studies. Additionally, gradually changing channel diameter is also an important factor for accurate mimicking of biological studies such as cells under confinement and microvascular studies.

One method to fabricate microfluidic devices with circular microchannels relies on circular templates, such as metal wires[63], [64] (Figure 3-1(a)), plastic threads[65], and glass capillaries[66]. This method provides perfectly circular channel cross-sections.

However, this technique is not capable of fabricating complex microchannel patterns with junctions or bifurcations, which has been shown to influence flow patterns and particle transport in flow[67], [68]. Furthermore, uniform diameter of wires, threads, or capillaries cannot provide a desired gradual change of channel diameters and also limits the minimum microchannel diameter that can be fabricated. Another technique infuses gas into existing rectangular microchannel filled with liquid PDMS to reshape it into a circular one[69]–[71](Figure 3-1(b)). This method requires a complicated process and it cannot be controlled to produce channels with gradually changing diameters. A third method involves fabricating, aligning and bonding of two semi-circular microchannels. Researchers used photoresist annealing[72], [73] and micromilling[74], [75] to create molds to cast semi-circular channels. Although some methods are used to align the 2 halves of semi-circular channels, it is almost impossible or extremely complex to perfectly align them. Parker[76] used 3D printed molds to cast semi-circular channels. After aligning and bonding of two halves of circular channels, they utilized infusion of air stream with liquid PDMS to round and correct the alignment error. However, this approach still does not offer the control for desired gradual change of diameters and it is more complicated and time-consuming.

The methods described above are not sufficient to achieve complex circular patterns with junctions or bifurcations while providing different channel diameters within one channel network. The grayscale lithography offers an alternative approach by fabricating three-dimensional microstructures in a faster and simple way[40], [41], [77]. In our previous study, a Digital Light Processing (DLP) projector with grayscale effect was demonstrated to generate patterned surface microstructures, such as micro-wavy pattern[78], . In this study, a “grayscale dual-projectoion lithography” method was

developed as a new approach to precisely fabricate customized circular microfluidic devices with complex features.

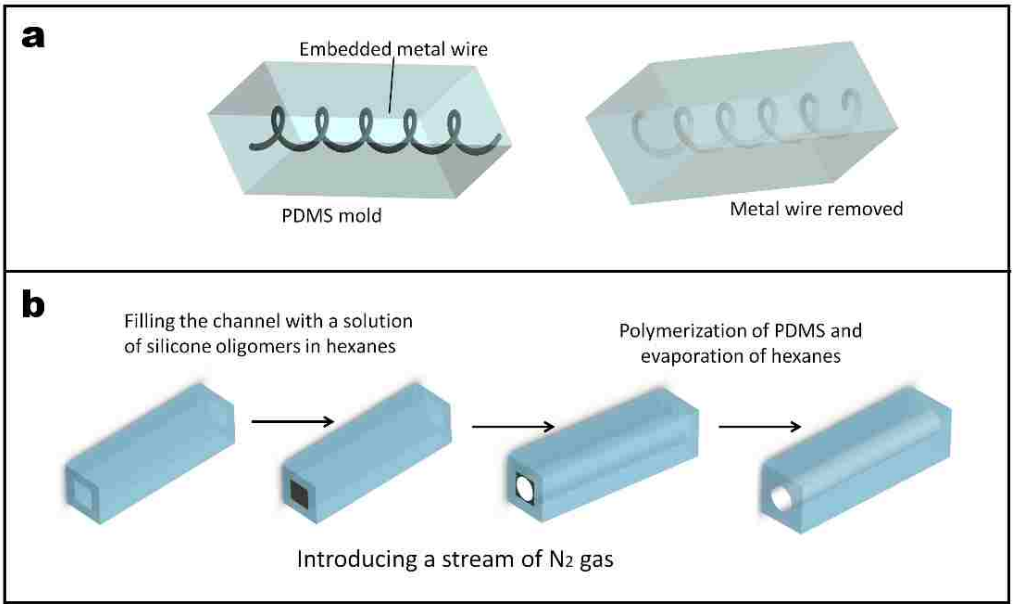

Figure 3-1 (a) Circular channel fabricated by metal wire removal process (Jung's group); (b) Circular channel fabricated by infusing gas into rectangular channels filled with liquid PDMS to reshape it into circular shape (Kumacheva's group).

3.2 Method and Materials

3.2.1 Establishment of the Polymerization Model for Dual-projection Lithography

A grayscale polymerization has been developed in our previous research of generating wavy patterns. However, projecting grayscale image from one direction can only generate concave channels and is incapable of creating full circular cross-sections. To generate channels with closed profiles in cross-section, a grayscale dual-projection lithography method that utilizes two projecting systems to expose grayscale images face-to-face and simultaneously polymerize the material is developed. Instead of generating a concave channel (mathematical model shows in Figure 3-2(a-b)), channels with closed cross-section profile, such as circular and elliptical, are created through polymerizing the

top and bottom parts by the corresponding UV light from two directions and bonding in the middle. Figure 3-2(c) shows the mathematical model of the polymerization profile in cross-section based on this technique. By setting the proper thickness of the photosensitive material, two concave parts can be polymerized separately and the overlapped energy in the middle (red color areas in Figure 3-2(c) forms a bonding between two concave parts. Therefore, by setting the grayscale values properly, the mathematical model can predict to generate a channel with circular or elliptical cross-section shapes.

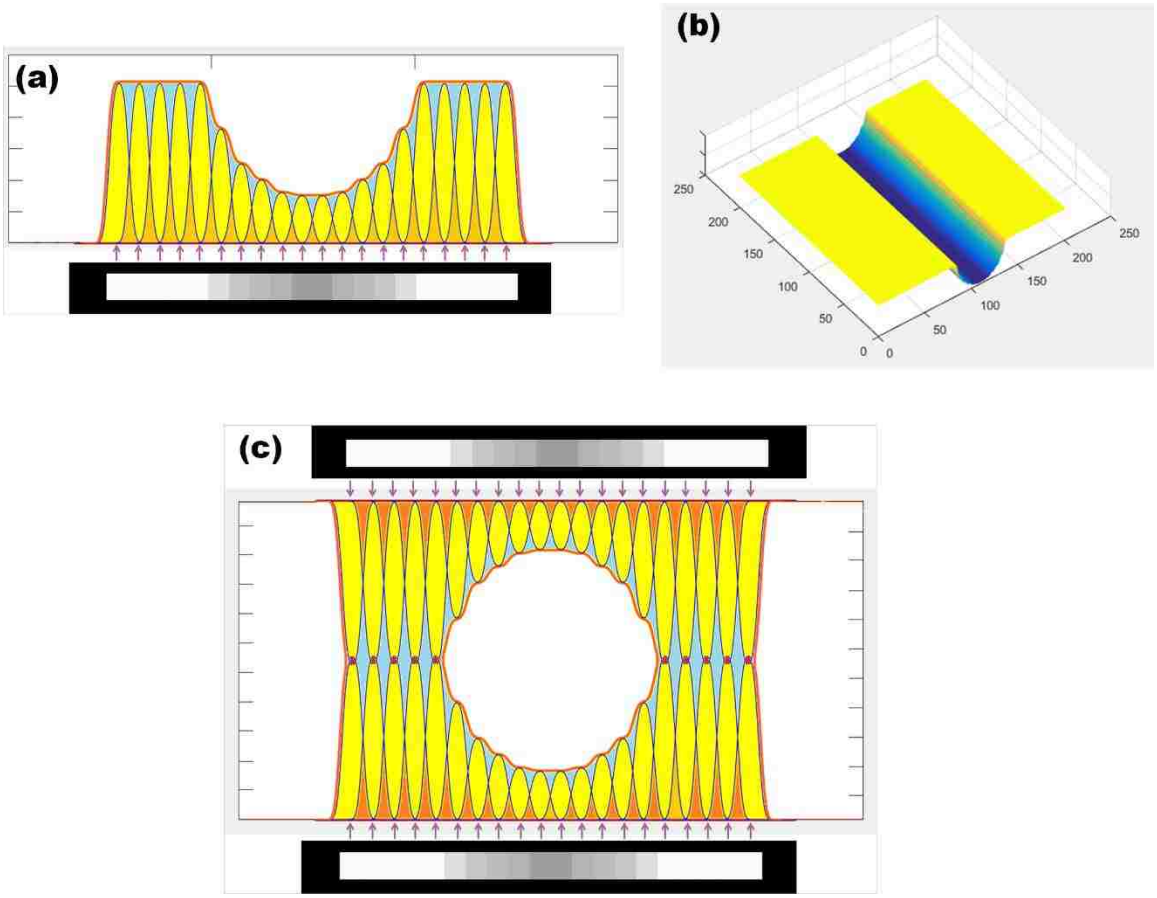

Figure 3-2 (a) The polymerization model under the exposure of 20 pixels with various grayscale values; (b) The 3D polymerization model based on the grayscale values used in (a); (c) A mathematical polymerization model of grayscale dual-projection lithography.

Since the material and projecting system are different from the setup in Chapter 2, an updated relation between grayscale level and polymerization depth is established by the

same method in Chapter 2. The polymerized object with the corresponding grayscale value is shown in Figure 3-3(a). A grayscale value under 145 will not lead to any curing while increasing the grayscale value (greater than 145) will lead to a greater the polymerization depth. Then the profile of the polymerized object is measured by a contact profilometer with stylus force set to 0.03 milligrams. A curve is given in Figure 3-3(b) based on the measure profile representing the relation between the grayscale value G and the polymerization depth D_0. This relation can be expressed by the following piecewise functions after curve fitting:

$$\mathrm{D}_0(G) = \begin{cases} 27.5\mathrm{e}^{0.024823(\mathrm{G}-145)} - 27.5 & (145 < G \leq 190) \\ 455.88\ln(\mathrm{G}) - 1947 & (190 < G \leq 255) \end{cases}, \quad 3)$$

Based on our Gaussian distribution model, the polymerization model for a single white pixel (grayscale 255) was given in equation (2) (in Chapter 2.2.2). Then the final polymerization model of one pixel can be expressed as:

$$\mathrm{D}_2 = \begin{cases} (\mathrm{k}_{\mathrm{r1}}\mathrm{e}^{\mathrm{k}_{\mathrm{r2}}\mathrm{G}} - \mathrm{k}_{\mathrm{r3}}) \sum_{\mathrm{i}=0}^{\mathrm{n}} \frac{\mathrm{k}_{\mathrm{r0}}}{\sigma_2\sqrt{2\pi}}\, \mathrm{e}^{\frac{-\left(\mathrm{x}+\frac{\mathrm{i}}{\mathrm{n}}\right)^2}{2{\sigma_2}^2}} & (145 < G \leq 190) \\ (\mathrm{k}_{\mathrm{r4}}\ln(\mathrm{G} - \mathrm{k}_{\mathrm{r5}}) - \mathrm{k}_{\mathrm{r6}}) \sum_{\mathrm{i}=0}^{\mathrm{n}} \frac{\mathrm{k}_{\mathrm{r0}}}{\sigma_2\sqrt{2\pi}}\, \mathrm{e}^{\frac{-(\mathrm{x}+\frac{\mathrm{i}}{\mathrm{n}})^2}{2{\sigma_2}^2}} & (190 < G \leq 255) \end{cases}, \quad 4)$$

where D_2 is the polymerization depth, G is the grayscale value, x is the coordinate position on the focus plane, and $\mathrm{k}_{\mathrm{r0}}, \mathrm{k}_{\mathrm{r1}}, \mathrm{k}_{\mathrm{r2}}$, and k_{r3} are factors determined by the photosensitive material properties, light wavelength and the exposure time. The values of $\mathrm{k}_{\mathrm{r0}}, \mathrm{k}_{\mathrm{r1}}, \mathrm{k}_{\mathrm{r2}}, \mathrm{k}_{\mathrm{r3}}, \mathrm{k}_{\mathrm{r4}}, \mathrm{k}_{\mathrm{r5}}, \mathrm{k}_{\mathrm{r6}}, \sigma_2$, and n are 1.43, 1.9065×10-3, 0.0248, 0.06973, 0.7303, 145, 2.4329, 0.07 and 10, respectively. The threshold of the grayscale value is 145, which is measured based on the UV light source (385nm) and the absorption properties of the

materials. Any exposure light with a grayscale value less than 145 will not lead to polymerization of the material.

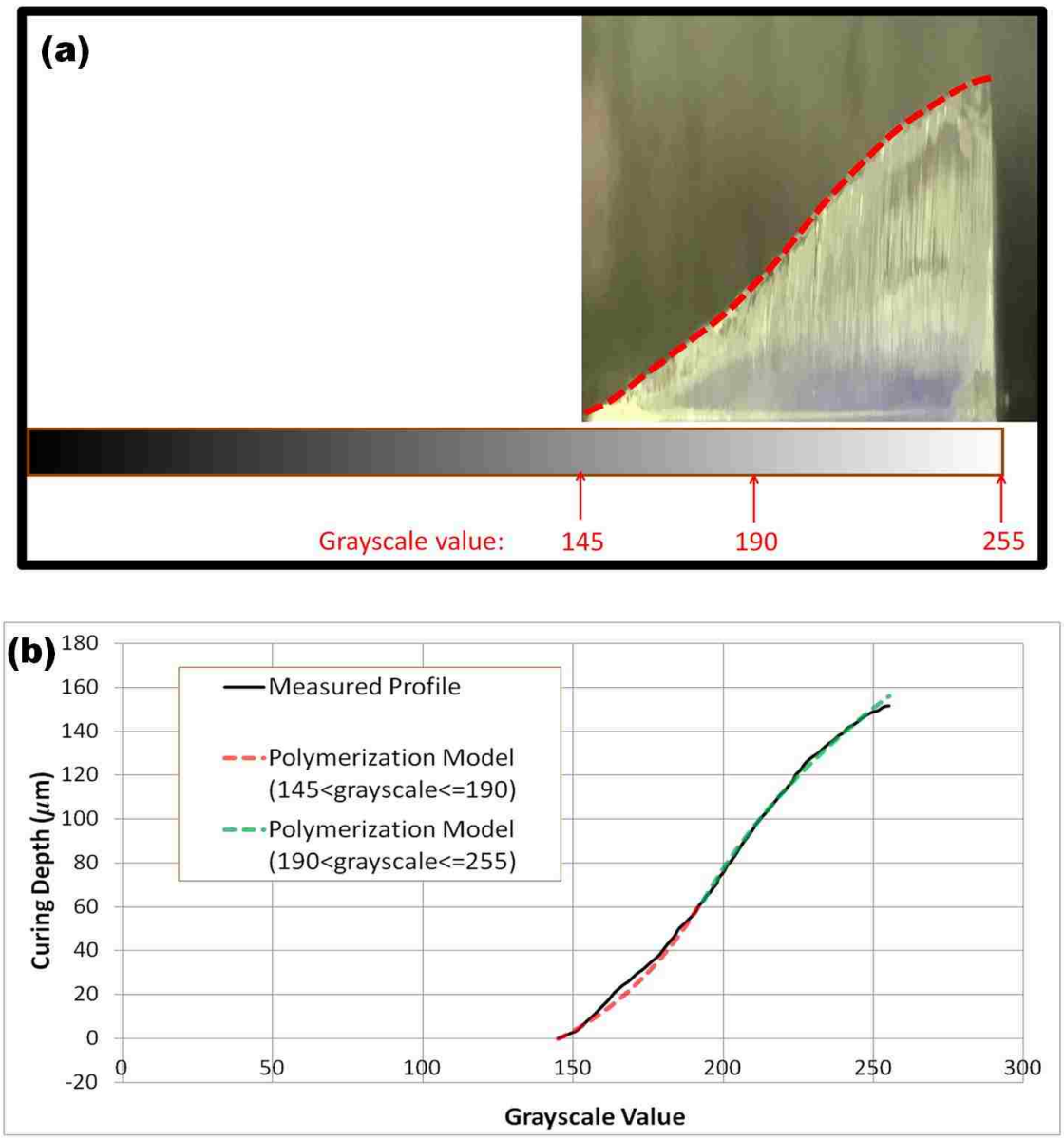

Figure 3-3 (a) Cured objected under the gradient of grayscale exposure; (b) Polymerization depth vs. Grayscale value based on measured profile and the curve fitting functions.

3.2.2 Development of the Fabrication System

This grayscale dual-projection lithography method relies on a fabrication system to produce precisely-generated channels. As the schematic shows in The system setup of

grayscale dual-projection lithography technology, this setup mainly consists of a fabrication platform, two UV projection systems, and four high-precision linear systems.

During the channel generation process, the photosensitive material is placed between two optically transparent substrates, and the thickness of the material is controlled by the spacers. The exposure light from top and bottom will focus on the upper and lower interface between the substrate and material. The fabrication platform serves as a holder for the substrates and is fixed. In each projection system, light from a UV light source (CWL 385nm) passes through the optical lenses, reflected the by the DMD chip (DLP6500FYE, Texas Instruments), and focused on the top surface of the bottom substrate by the projection lenses. Grayscale images are transmitted to the DMD from PC and exposed to the photosensitive material. Based on the optical setup, the smallest pixel size focused on the substrate is 10μm. The linear systems include two Z (upper and lower) stages which sets the focal length of the upper and lower projection, as well as X and Y stages which help to set the alignment of upper and lower projection by precisely tuning the position of the upper projection system. The Z stage has a minimum step of 10μm while the X and Y stages have a minimum step of 2.5μm. To calibrate the alignment of projections, exposure images with a cross pattern are projected at the same time from upper and lower projection systems. As the alignment calibration in Figure 3-4 shows, when the two cross patterns are completely overlapped, the projections are well aligned.

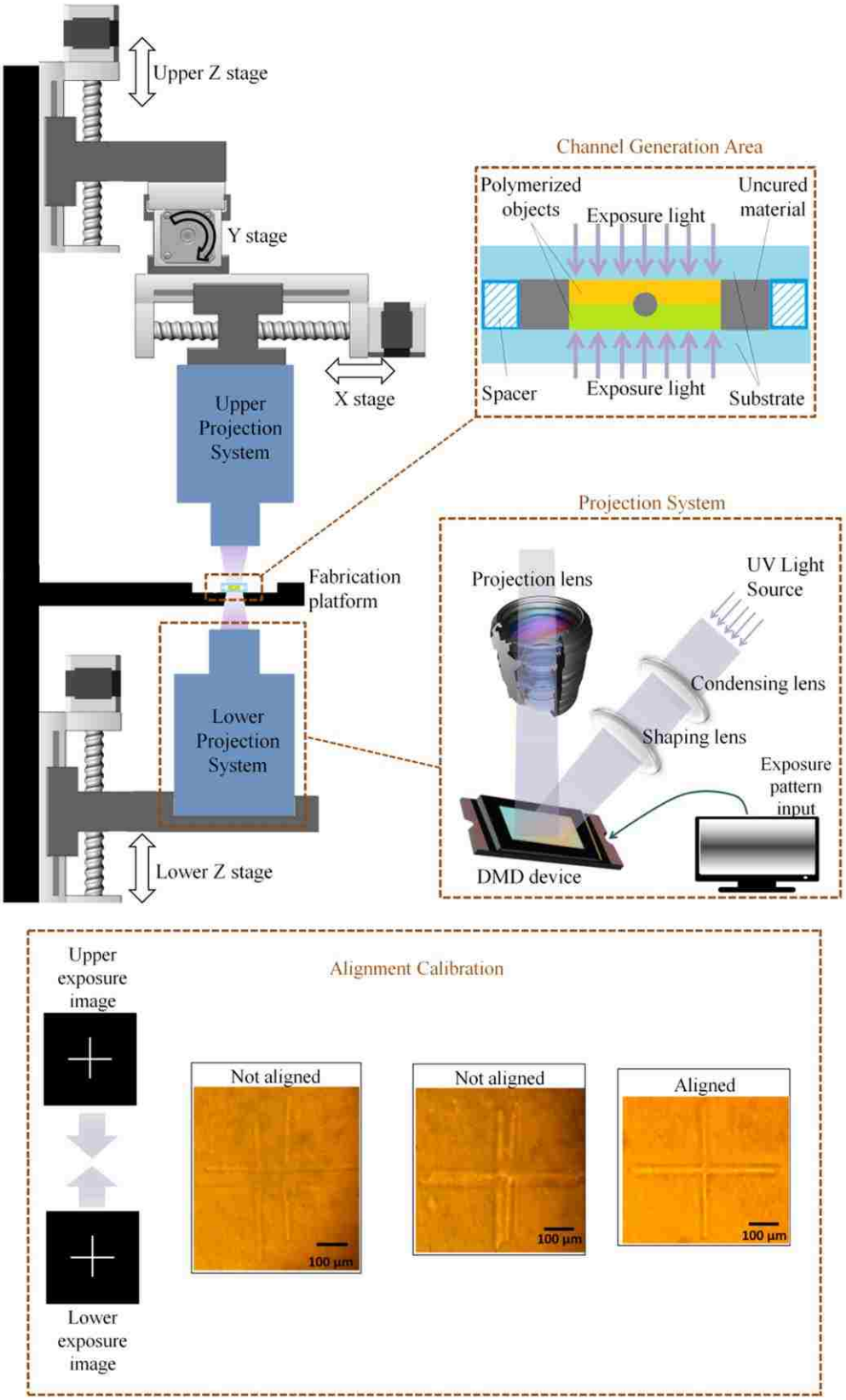

Figure 3-4 The system setup of grayscale dual-projection lithography technology

3.3 Results and Analysis

3.3.1 Comparison Results between Mathematical Models and Fabricated Profiles

The cross-section views of the fabricated channels are compared with the mathematical predictions to ensure the accuracy of the simulation. In Figure 3-5(a-c), the cross-section profiles of the fabricated channels are captured by a digital microscope. Using exposure images with different combinations of grayscales (Figure 3-5(g-i)), elliptical channels with major axis in horizontal direction and vertical direction, as well as a full circular channel can be generated. Figure 3-5(d-f) show the comparison between the profiles of three fabricated channels (dashed lines in red) and the mathematical predictions (black lines with yellow fill). All three features in Figure 3-5(d-f) show good agreements between the actual fabricated profiles and the mathematical predictions. Furthermore, the actual curing process helps in smoothing the original ripples in the mathematical models, which generates smoothly curved surface inside the channel. Therefore, the mathematical model can be utilized to provide the predictions of the shapes and the grayscale values of exposure images for fabricating channels with customized cross-section profiles.

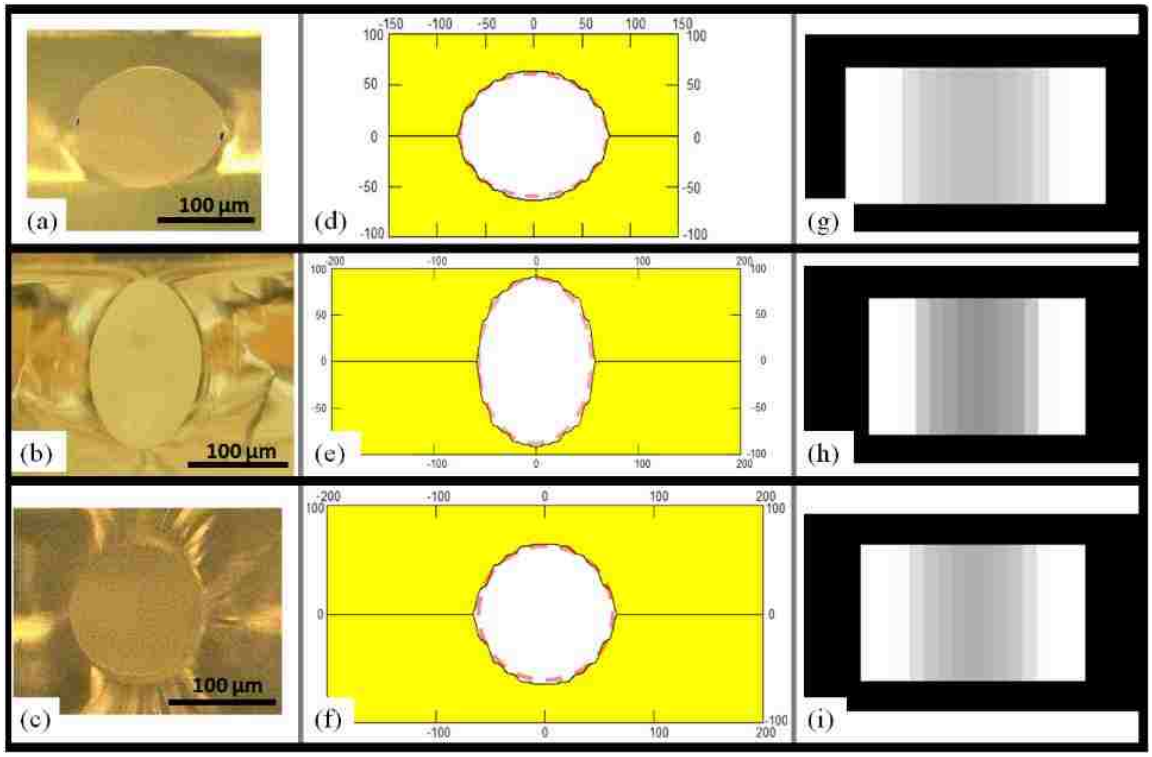

Figure 3-5 Comparison of the cross-section profiles between fabricated channels and mathematical predictions (a-c) Cross-section profiles of the fabricated microchannels under a digital microscope; (d-f) Cross-section profiles of the fabricated channels in (a-c) (red dashed lines), and mathematical predictions (black lines with yellow fill); (g-i) The corresponding grayscale exposure images.

3.3.2 Characterization of Fabrication Parameters

The image exposure time in the polymerization process is less than 30seconds. To generate completely through channels, firstly the substrate containing the polymerized object and uncured materials is immersed in acetone to develop for 15minutes. Next, Isopropyl Alcohol 99% is loaded into syringes and pumped through the channels via a syringe pump (Harvard Apparatus) to completely remove any uncured materials inside the channel. The second step takes 15-30 minutes, depending on the complexity of channel networks. Then the fabricated microfluidic device will be taken out from the developer and dried in oven in 60ºC for 10mins. The OmniCure s1500 curing system with an irradiance

intensity of 23 W/cm2 in 365nm wavelength is used to further polymerize the fabricated channels. The entire process, including image exposure, developing, oven drying, and post-curing, takes less than 1 hour. In a microscope image (Figure 3-6(a)), a straight channel with a 70μm circular cross-section (Figure 3-6(b)) is generated. The channel is completely though which allows the droplet to pass when injecting water inside (Figure 3-6(c)). By exposing a grayscale image with a gradient shrinkage along the channel direction, a circular channel with gradual change in diameter that ranges from 39μm to 60μm within 270μm distance is generated (Figure 3-6(d)). The current setup is capable of generating a circular channel with a smallest diameter of 39μm. Circular channels with smaller diameters can be potentially achieved by applying optical apparatus and linear systems with higher precision to reduce the optical errors and achieve better alignment of two projection systems.

Complex circular channels with features such as junctions, bifurcations, hierarchies and gradual changed diameters can be generated by the grayscale dual-projection method. Circular microchannels with complicated networks can be easily fabricated under one step exposure. In Figure 3-7(b-d), a microvascular network that has multiple bifurcations with a channel diameter of 120μm is fabricated through the exposure of the corresponding grayscale image (Figure 3-7(a)). In Figure 3-7(f-g), a capillary mesh with a channel diameter of 105μm is fabricated as a demonstration sample. Compared with the microvascular network, the capillary mesh has smoothly curved joints instead of joints with an angle. In Figure 3-7(i), two straight circular channels with a diameter gradient ranging from 70μm to 250μm are generated. To generate ready-to-use microfluidic devices with circular channels, the upper exposure image will have two black holes designed for the

inlet and outlet (Figure 3-7(j)). The areas where the black holes are exposed will remain uncured in order to allow the assembling of tubing, which serves as the input and output of liquid media. In this case, polydimethylsiloxane (PDMS) can serve as the substrate to directly contact the polymerization interface since the polymerized objects can separate from PDMS easily due to the oxygen inhibition effect[39], [79]. Therefore, this method can directly generate microfluidic devices with circular cross-section and complex networks (Figure 3-7(k)). With this grayscale dual-projection approach, a microfluidic device with completely customized circular channels can be generated within 1 hour without the need of clean room or expensive photolithography devices.

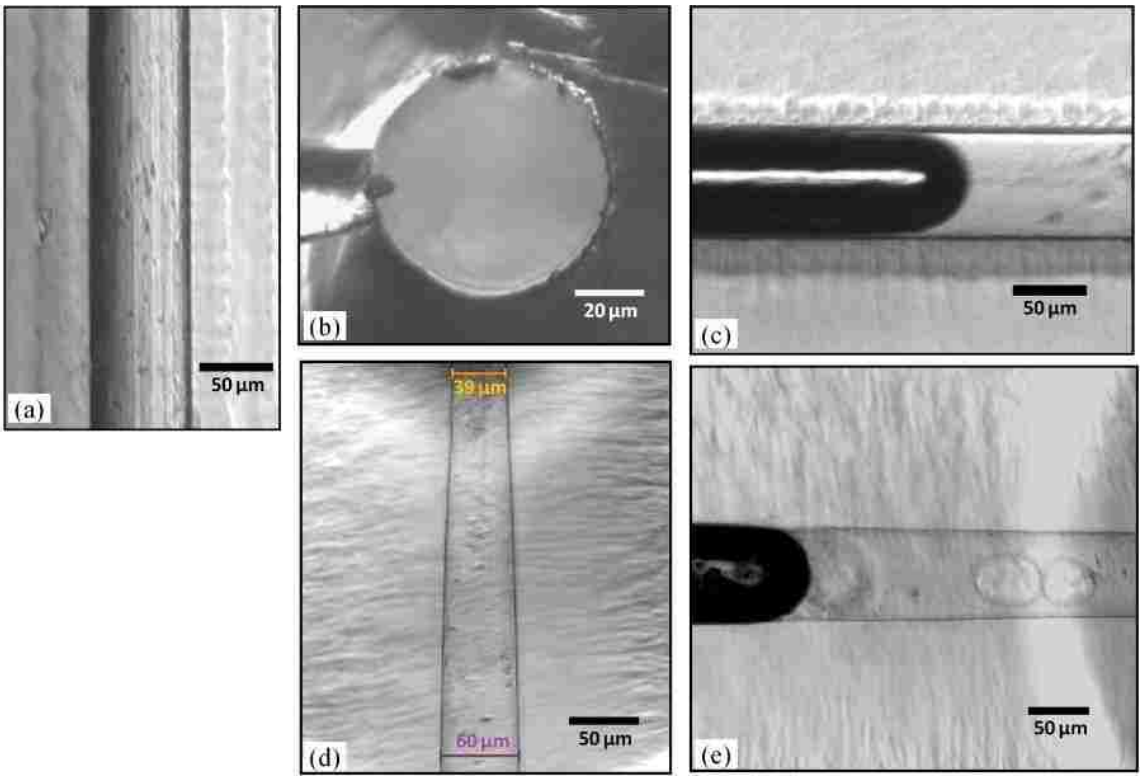

Figure 3-6 Microscope images of fabricated microchannels (a) A straight circular channel with 70µm channel width; (b) The cross-section view of the channel in (a); (c) A droplet passing the channel in (a); (d) A circular channel with gradual change in diameter; (e) A droplet passing the channel in (d).

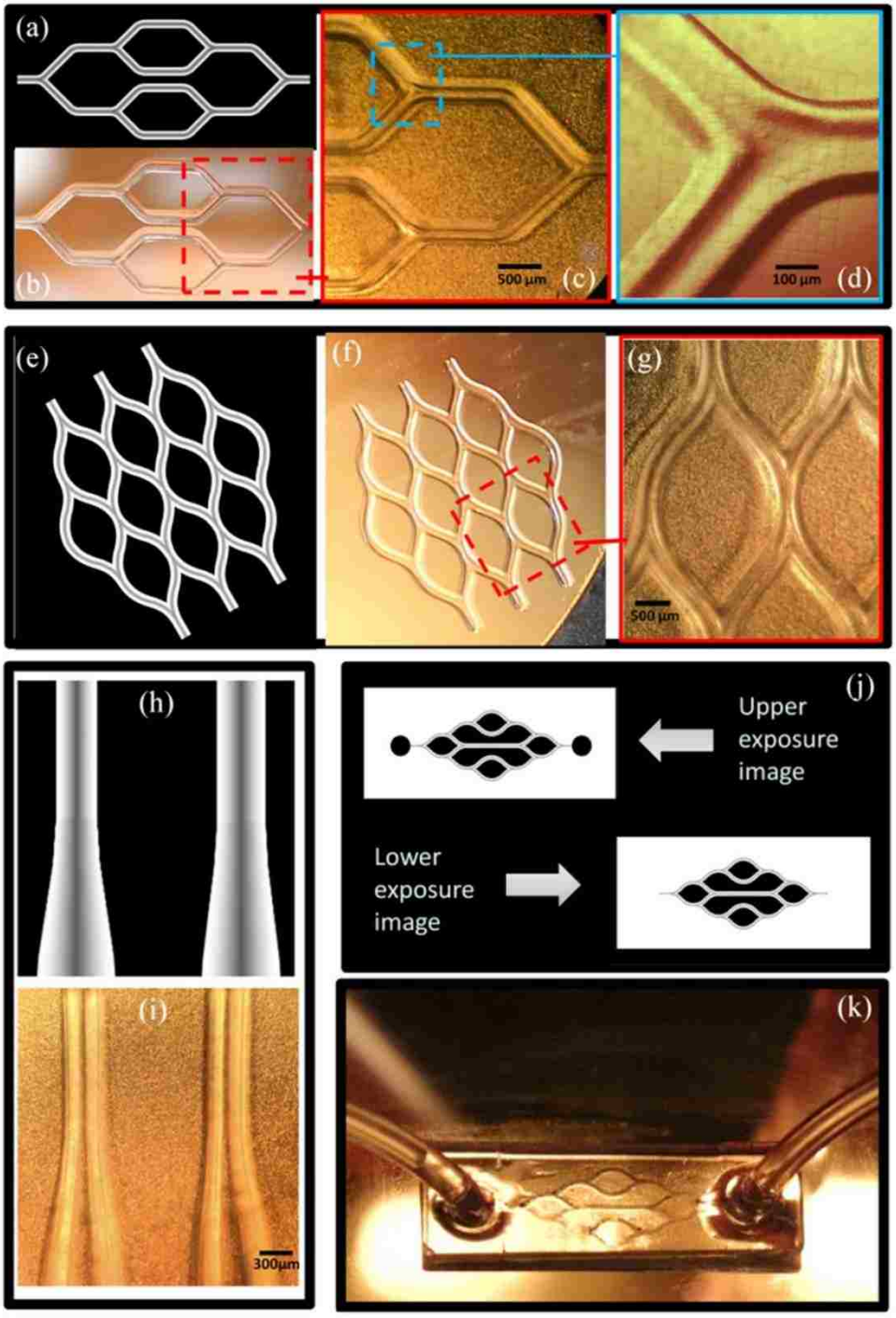

Figure 3-7 Fabrication of customized circular channels in various complexities (a-d) Corresponding grayscale exposure image and a fabricated microvascular network with multiple bifurcations; (e-g) Corresponding grayscale exposure image and a fabricated capillary mesh with smoothly curved joints; (h-i) Corresponding grayscale image and two fabricated straight circular channels with a diameter gradient; (j-k) Corresponding grayscale images and a fabricated microfluidic device with circular cross-section and complex channel networks.

3.3.3 Application: Nanoparticle binding distribution Study

To demonstrate a potential application for this technique, microfluidic devices with circular cross-section were made to study the binding and distribution of particles of various sizes. Nanoparticles have been widely studied as a multifunctional carrier in therapeutic drug delivery[80], [81]. Prediction of nanoparticle distribution has great importance in evaluation of therapeutic efficacy. Previous studies of characterizing nanoparticle delivery in microcirculation have been done in rectangular microchannels[82], [83],[84].However, since the geometry effect can lead to a non-uniform distribution of the nanoparticles and further affect the binding characteristics, circular microchannels can be more realistic in the study of nano and microparticle distributions within flow, as well as the characteristics governing their adhesion to the channel walls.

Fabricated microfluidic channels were prepared and flushed with DI water to ensure the channels were unobstructed. Fluorescent particle suspensions were prepared in 1X PBS solution using a 250 nm diameter particle stock and 3.2 μm diameter particle stock, to a concentration of 0.01125mg/mL for both particle sizes independently. The prepared particle suspensions were loaded into syringes and pumped through the channels via a syringe pump (Harvard Apparatus) at varying shear rates of 200/sec, 800/sec, and 1600/sec. Particle suspension flow times were varied to ensure the exact same volume of suspension was flown through each channel at the three shear rates noted previously. All of the fabricated microfluidic devices utilized for flow studies were secured onto the stage of a Nikon Eclipse Ti confocal microscope, using a Nikon C2 Si camera, for image acquisition during and after flows. The excitation and emission utilized to image the fluorescent particles was set for FITC (Fluorescein isothiocyanate) imaging. During the flow processes, the confocal unit was utilized to scan the entire cross-section of the channel to capture the

positions of the particles in solution under flow conditions. These distribution scans were run with a 310nm step size in order to capture the fine features associated with particle distributions within shear flow. After particle suspension flows were established for the pre-determined period of time, the confocal unit was used to scan the walls of the circular channels to capture the information of the particles which bound to the walls during the flow. All of the data collected from the confocal scans was later analyzed using the ImageJ (FIJI) software. The particle distribution information collected from the scans agree well with the expected results because a similar trend of peak particle distribution is observed[82], [83], demonstrating the practicality of devices fabricated by this presented technology.

Figure 3-8(a) illustrates the degree of particle binding based on particle size and the shear rate established within the fabricated channels. It can be observed that a higher degree of particle binding occurs for the smaller 250nm particles when compared to the larger 3.2μm particles. This is observed because the smaller 250nm particles have less surface area to be affected by the shear force, and as such they are better able to bind to the channel walls and remain adhered. In this case, the smaller particles stick better because they experience less shear force. Additionally, it is observed that the degree of particle binding decreases as the shear rate established in the channels increases, regardless of particle size. In Figure 3-8(b-c), the particles concentration in flow show distinctive peaks near the wall of the channel, and drops to nearly zero directly next to the wall. The core of the channels is observed to have a baseline level of particle concentration lower than that of the peaks formed in close proximity of the channel wall. The distribution of the particles is also influenced by shear rate in such a manner that increased shear rates lead to peaks in

the particle distribution closer to the channel walls. Figure 3-8(d) shows a section of the circular channel with a diameter of 76µm used in the particle binding experiment. The channel was filled with FITC dye with a concentration of 0.625mg/ml and scanned via confocal microscopy at a resolution of 310nm to identify the overall cross-sectional shape the channel.

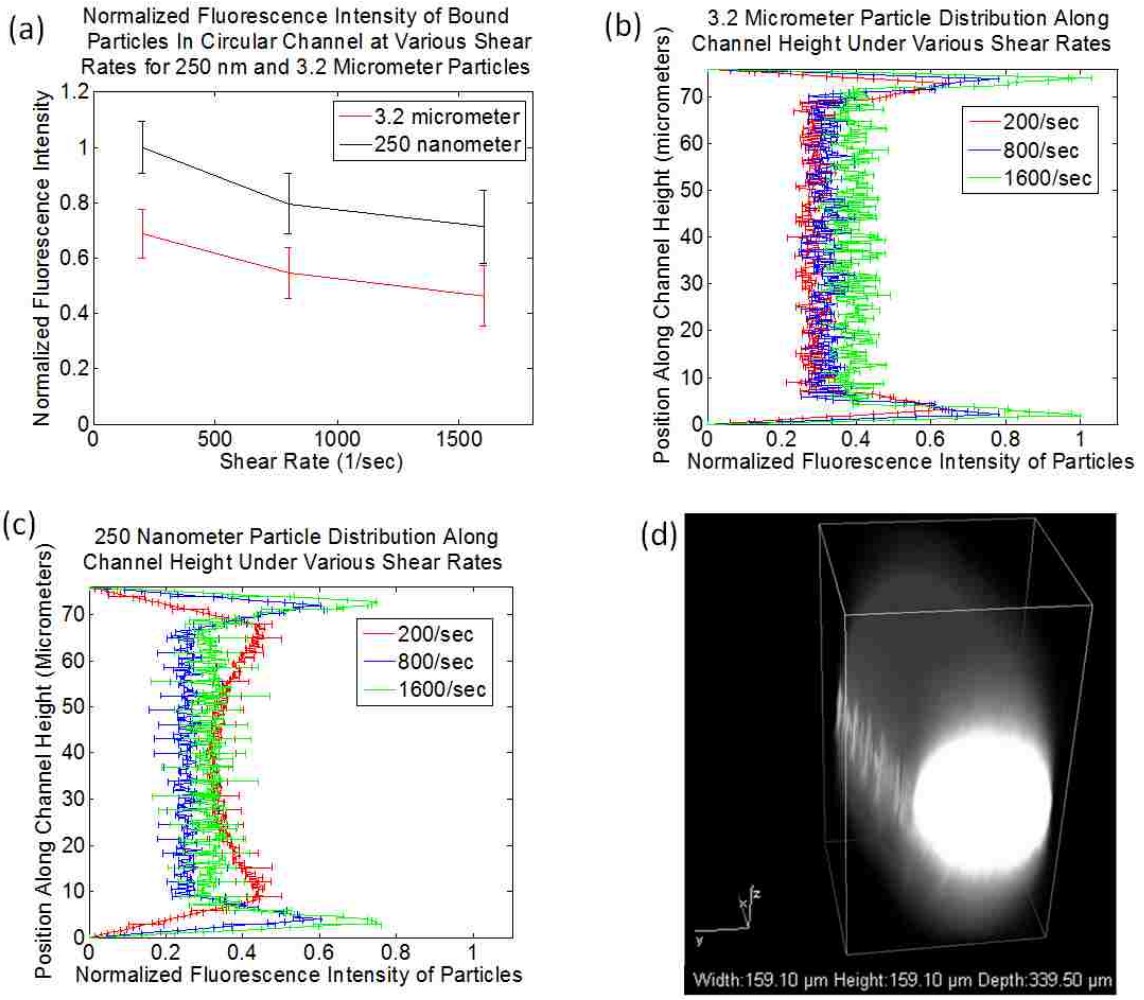

Figure 3-8 (a) The degree of particle binding based on particle size and the shear rate established within the fabricated channels; (b) 3.2µm particle distribution along channel height under various sheer rates; (c) 250nm particle distribution along channel height under various sheer rates; (d) A confocal scanned 3D image of a section in the microchannel used for the experiment.

Compared to other fabrication techniques[69]–[76] for the production of microfluidic devices, this grayscale dual-projection method provides a better alternative for quick, production of microfluidic channels at a reduced cost and capable of handling a much wider variety of channel properties and geometries. This grayscale microfluidic fabrication technique will allow for more advanced and complicated channels to be produced allowing for improved scientific testing and experimentation while overall serving as a more cost effective and time saving tool for nanomedicine and therapeutic studies.

3.4 Experimental Setups

The photosensitive material used in this research is a mixture of Laromer 8986 (an aromatic modified epoxy acrylate, BASF Co.), Laromer TPGDA (Tripropylene Glycol Diacrylate, BASF Co.), ethoxylatedtrimethylolpropanetriacrylate (TMP3EOTA, Eterner Chem. Co.). Irgacure 754 (a mixture of Oxy-phenyl-acetic acid 2-[2-oxo-2-phenyl-acetoxy-ethoxy]-ethyl ester and Oxy-phenyl-acetic acid 2-[2-hydroxy-ethoxy]-ethyl ester) and Irgacure 4265 (a mixture of Diphenyl (2,4,6-trimethylbenzoyl-phosphine oxide and 2-Hydroxy-2-methyl-1-phenyl-propan-1-one)) from BASF Co. was used as photoinitiators. 0.2%wt. Tinopal OB (BASF) is used as a UV absorber.

3.5 Conclusions

This research provided a novel method of generating circular channels with highly customizable networks based on grayscale dual-projection lithography. Compared with prior arts, this method has advantages in producing circular channels with a wide range of diameters (39μm to 2mm), and elliptical channels with a major-to-minor axis ratio up to 600%. Meanwhile, complex channel geometrics (such as junctions, bifurcations,

hierarchical structures, and different channel diameters) that are incapable to be fabricated by other approaches can be easily generated through this technology. Furthermore, this method brings high efficiency as well as low cost to fabricate highly customized lab-on-chip devices. This technique can potentially provide great convenience for researchers in microfluidic areas and improve scientific experimentation for biological and medical applications, especially in nanomedicine and therapeutic studies.

Chapter 4 : In Situ Generating Microfluidic Controllable Actuators Based on Two-Color Inhibited Lithography

4.1 Introduction

Microfluidic actuators and movable microstructures are widely used in microelectromechanical systems[85], biochemical areas[86] and biomedical engineering applications[87]. In particular, wireless controlled actuators and microstructures are helpful in microfluidic applications such as mixing[88], pumping[89] as well as studies of microdroplets and microparticles[90]. Researchers have made significant advances in producing and actuating microstructures. Among all these methods, in situ fabrication of the actuated microstructures inside the microfluidic channels is of great interest. UV polymerization method is an easy way to generate complex structures in situ. However, the typical UV curing technique will create adhesion between the polymerized structures and the substrates, which prevents the mobility of the fabricated structures. Some researchers used oxygen as the inhibitor to create an uncured layer in separating the polymerized objects and the substrates[79][91]. Oxygen molecules can react with free radicals in the photocurable material to generate oxidized radical, which are ineffective in the polymerization process. Then PDMS, a commonly used microfluidic materials with high oxygen solubility, is widely used to fabricate movable microstructures in situ.

Doyle's group utilized the oxygen-aided inhibition near the PDMS surface to fabricate polymeric particles in a continuous flow[91]. It gave an easy approach to

synthesize polymeric particles of varied shapes with a high-throughput (400,000 particles /hr). However, this approach is not capable of generating particles with highly controlled three dimensional shapes and the motion of fabricated particles cannot be further controlled. Kown's group developed an in situ magnetic actuator fabrication technique to fabricate three-dimensional free-floating microstructures with magnetite embedded[92]. Magnetic nanoparticles were mixed with UV curable polymers as the material system. The oxygen diffused through the PDMS walls formed an oxygen inhibition layer that prevented the adhesion between the polymerized structures and the PDMS substrate. This method allows the creation of various structures such as cantilever, motor, and rail-guided actuators. The motion of these structures can be controlled under magnetic field. However, in order to allow the control of fabricated actuators, this approach requires the pre-fabrication of auxiliary structures, such as a pre-fabricated PDMS post as the axle for rotatable gears and a prefabricated PDMS groove as the rail for sliding valves. Another method developed by Huang's group used similar oxygen inhibition effect to fabricate suspending microrotors in microfluidic channels and actuated mircorotors by acoustic streaming flows[93]. High rotation of the microrotors can be achieved with special designed structures. However, this control method is only capable of actuating specific structures in certain flow conditions. Furthermore, a pre-fabricated PDMS axle is also required in order to rotate the microrotors. These prefabricated posts require extra steps (normally use clean room lithography) in fabricating microfluidic devices and need to be pre-aligned before UV exposure, which make the whole process not completely "in situ". Another method created by Yue's team fabricated both the polymerized gear and post in two regions inside the microfluidic device[94]. A laser served as optical tweezers was applied to carry the polymerized gear

and assembled it with the post. The laser also used to manipulate the rotation of the gear after assembly. Although this approach does not require the pre-fabrication of the axle for gears, it still needs specifically fabricated microfluidic devices made from both glass and PDMS. This method also requires an expensive laser setup for the manipulation of optical tweezers and a complex assembling process, which makes the operation process costly and less efficient.

Therefore, a novel method to in situ fabricate microfluidic actuators and controllable microstructures based on light inhibition, acoustic particle alignment and magnetic manipulation is developed. This method is expected to achieve a true in situ fabrication and easy manipulation in a cost-effective manner.

4.2 Method and Materials

4.2.1 Inhibition and Initiation Mechanism

In regular polymerization process, photocurable materials always contain monomer and photoinitiator to generate free radicals and react with monomer to form polymer chain. The photoinitiator can be initiated under the expose of light with the wavelength in the range of the absorbed spectrum. On the contrary, the photoinhibitor generates noninitiating radicals under inhibition light to couple with the growing polymer chain, terminate polymerization and prevent chain growth. In this presented technology, we use a photoinhibitor that can be inhibited under the expose of light, just like the typical UV inducible photoinitiator[95]. The inhibiting radicals are very-short lived since they are small molecular that remain unbound to the polymer chain and diffuse rapidly. If the photocurable material containing both photoinitiator and photoinhibitor is exposed under

both initiation light and inhibition light, the polymerization condition is determined by the contrast between the initiating and inhibiting radicals.

In this project, the monomer, photoinitiator and photoinhibitor used are triethylene glycoldimethacrylate (TEGDMA), camphorquinone (CQ) and tetraethylthiuram disulfide (TED). CQ and TED are chosen as a combination because CQ has a visible-light initiation system (peak around 473nm) and does not absorb near-UV light (around 365nm), while TED is activated by UV light (around 365nm) and does not absorb most visible light (above 470nm). Figure 4-1 shows the absorbance spectra of CQ and TED. The complementary absorption spectra of the photoinitiator and the photoinhibitor will be used to apply simultaneous control of both inhibition and initiation of the polymerization.

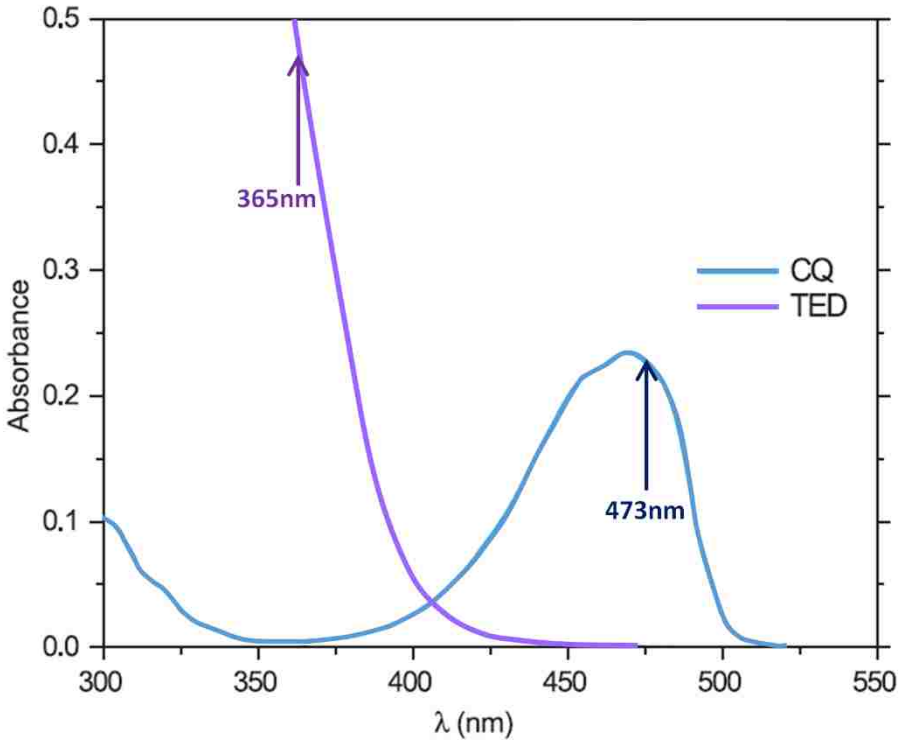

Figure 4-1 UV-visible absorption spectra of CQ and TED, demonstrating the complementary absorption spectra of the photoinitiator and the photoinihibitor, respectively[95].

4.2.2 Development of the two-color lithography system for microfabrication

One main target is to selectively create inhibition layers when fabricating microstructures inside the microfluidics, which requires the initiation light penetrates deeper into the photocurable resin compared with the inhibition light. UV dye is added to the resin in order to control and limit the penetration depth of the inhibition light. While the initiating light, with longer wavelength and does not absorbed by UV dye in the resin, can penetrate deeper into the resin to induce polymerization. Therefore, a two-color lithography system has been established as shown in Figure 4-2. A microfluidic device made by optical transparent substrate material is filled with the formulated photocurable resin inside the microfluidic channel. A dichroic longpass filter is applied to allow both inhibition and initiation light project bottom up to the lower substrate. Another inhibition light is projected from the top to the upper substrate. The initiation light has a 473nm wavelength while the inhibition light has a 365nm wavelength. The contrast of the initiation and inhibition light determines the thickness of the inhibition layer and the polymerization parts. Under a certain light intensity and microfluidic channel height, thick inhibition layer can be formed by projecting 365nm light in high intensity. Thinner inhibition layer will be generated by reducing the light intensity of the 365nm light. When the inhibition light is too weak to be compared with initiation light, the inhibition layer will disappear and polymerization will occupy the entire channel in the 473nm light projected region. When the inhibition light is projected to a portion of the area under the exposure of initiation light, inhibition layers only exist in those regions where inhibition light is involved. The polymerized objects sandwiched between two inhibition layers become free suspended structures inside the microfluidic channels while the polymerized parts without

any contact with the inhibition layer will adhere to the upper and lower substrates and become fixed microfluidic structures. Therefore, in situ fabrication of portable microstructures as well as fixed structures can be achieved by the selective exposure of inhibition light.

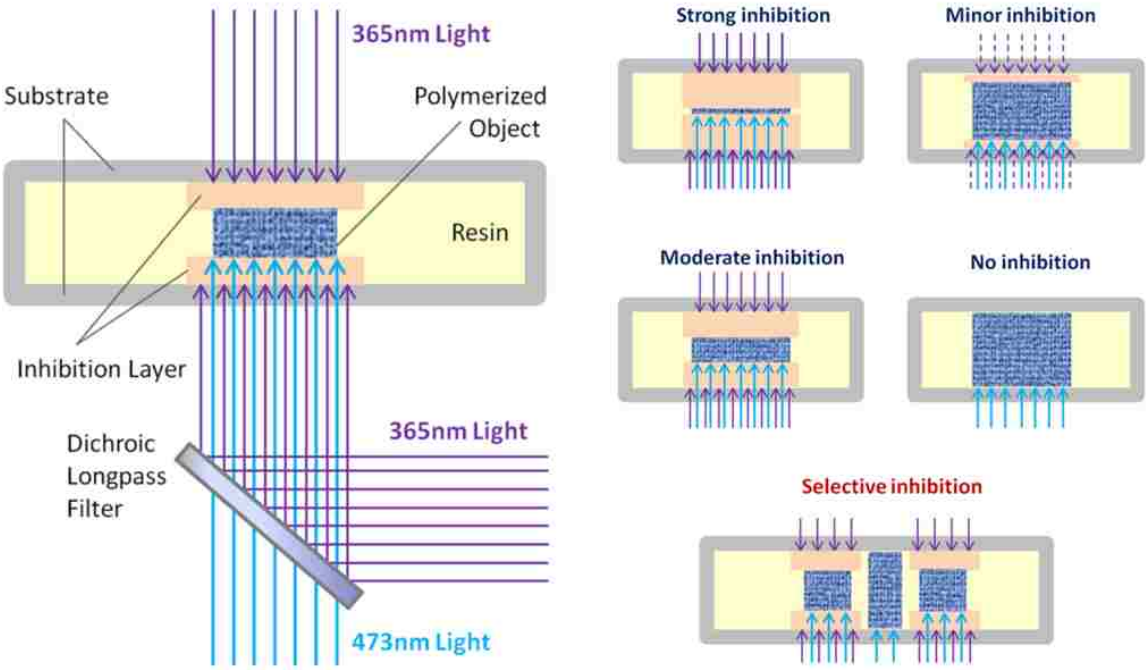

Figure 4-2 Schematic of two-color lithography system and the relation between polymerization condition and inhibition level.

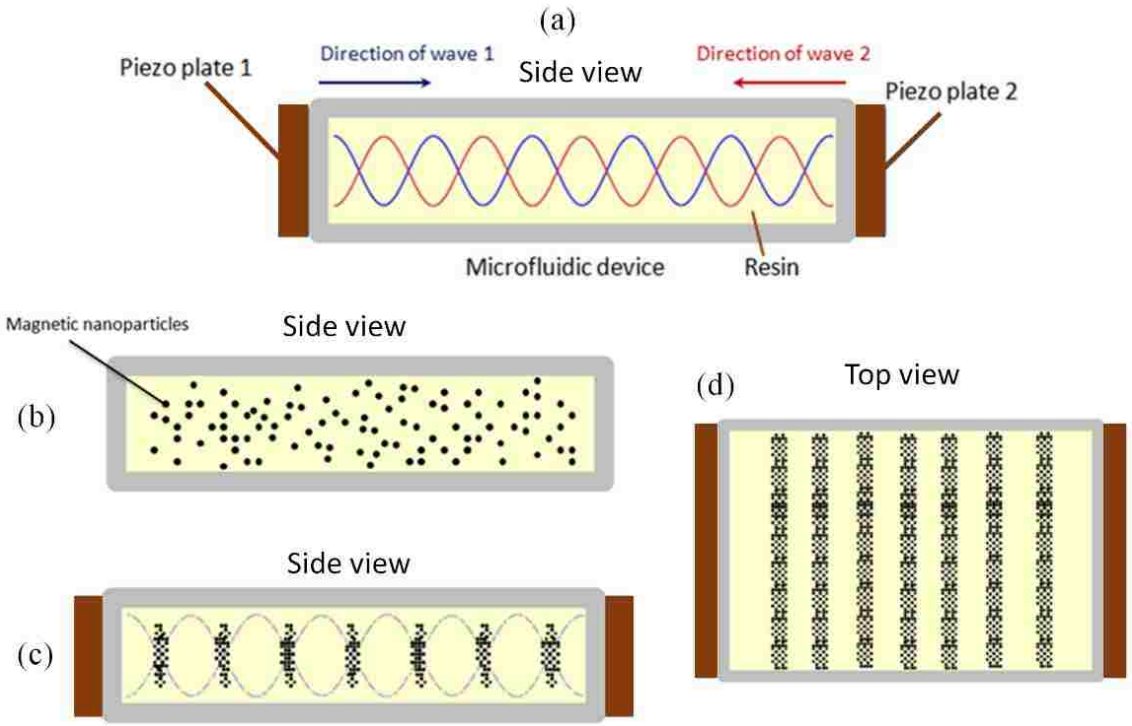

Figure 4-3 Schematic of piezo induce acoustic alignment of magnetic nanoparticles in microfluidic devices filled with resin (a)Generation of standing waves; (b)A microfluidic device with resin and magnetic nanoparticles before alignment;

4.2.3 Acoustic alignment of the magnetic nanoparticles inside microfluidic devices

To allow the polymerized parts controllable under remote magnetic field, magnetic nanoparticles are introduced into the photocurable material. Instead of placing the magnetic particles randomly, these particles will be aligned in order to be precisely controlled under the magnetic field. Two piezo transducer plates are attached to the two sides of the microfluidic device (device is made in glass, or similar transparent rigid material). When two piezo transducer plates with a certain resonant frequency are actuated, bulk acoustic waves are created inside the microfluidic channels. These two waves travel in opposite directions with the same amplitude and wavelength. Therefore, standing waves are produced by the interference of these two periodic waves (Figure 4-3(a)). Particles located

at a displacement node, a location where the amplitude of the displacement always zero, do not move at all. Other particles will move to the closest node under the driven force of acoustic radiation. As shown in Figure 4-3(b), magnetic nanoparticles are initially placed randomly inside the photocurable material. Once the two piezo plates are actuated simultaneously, the particles are accumulated near the closest nodes (Figure 4-3**Error! R eference source not found.**(c)). From the top view in Figure 4-3(d), the particles are aligned into parallel lines with a space of half acoustic wavelength.

4.2.4 Magnetic actuation of fabricated microstructures

The entire fabrication process starts with the injection of the photosensitive materials (including monomer, initiator, inhibitor and UV dye) along with magnetic nanoparticles. Next the magnetic nanoparticles are acoustically aligned to form parallel lines with equal spacing. Before the gravity force sinks the nanoparticles, two-color lithography is applied with selective inhibition. The 473nm initiating light will project the target pattern and the 365nm inhibition light from both top and bottom directions will only inhibit the area of the portable structure part (In Figure 4-4(a)). After the polymerization is finished, Isopropyl alcohol is injected into the microfluidic device to wash the uncured material and remained nanoparticles. Then a portable gear with well aligned magnetic particles embedded and a fixed post axis is fabricated as shown in Figure 4-4(b). Magnetic field will be applied to remotely control the rotation of the gear. Other microfluidic actuators, such as hinged values, mixer, and carrier, can be also fabricated and remotely actuated via this approach.

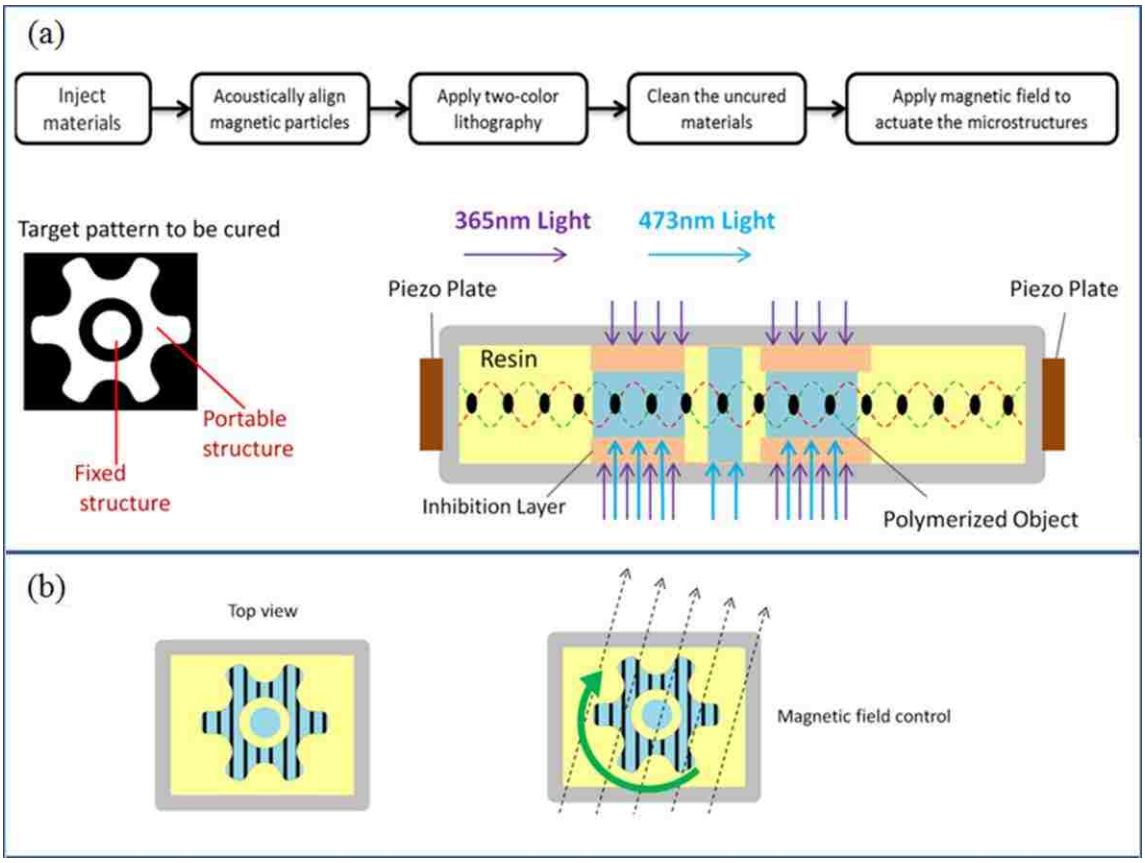

Figure 4-4 (a) Schematic of the fabrication process of a microfluidic actuator (a gear); (b) Remote control of the fabricated microstructures via magnetic field.

4.3 Results and Analysis

In this two-color lithography system, the inhibiting radicals are very short-lived and consume very fast. Therefore, both the inhibition light and curing light need to be fined tuned in a proper contrast ratio to prevent the exhaustion of the inhibiting radicals. The inhibition light has a fixed 3W/cm^2 irradiance in 365nm wavelength, while the curing light has an adjustable irradiance range from 0 to 250mW/cm^2 in 473nm wavelength. In a pure resin material without the introducing of magnetic particles, a floating object with 300μm thickness can be cured under the exposure time of 3500ms and curing light irradiance of 250mW/cm^2. In this situation, the inhibited layer has a uniform thickness of ~150μm.

When magnetic nanoparticles are introduced into the resin, the exposure time needs to be extended to cure an object with the same thickness level. Material with 6.0 wt% magnetic nanoparticles takes 6000ms (same light irradiance) to be cured in a thickness of ~500μm. Meanwhile, the inhibited layer thickness under the lines of aligned particles are in a range of 50-100μm.

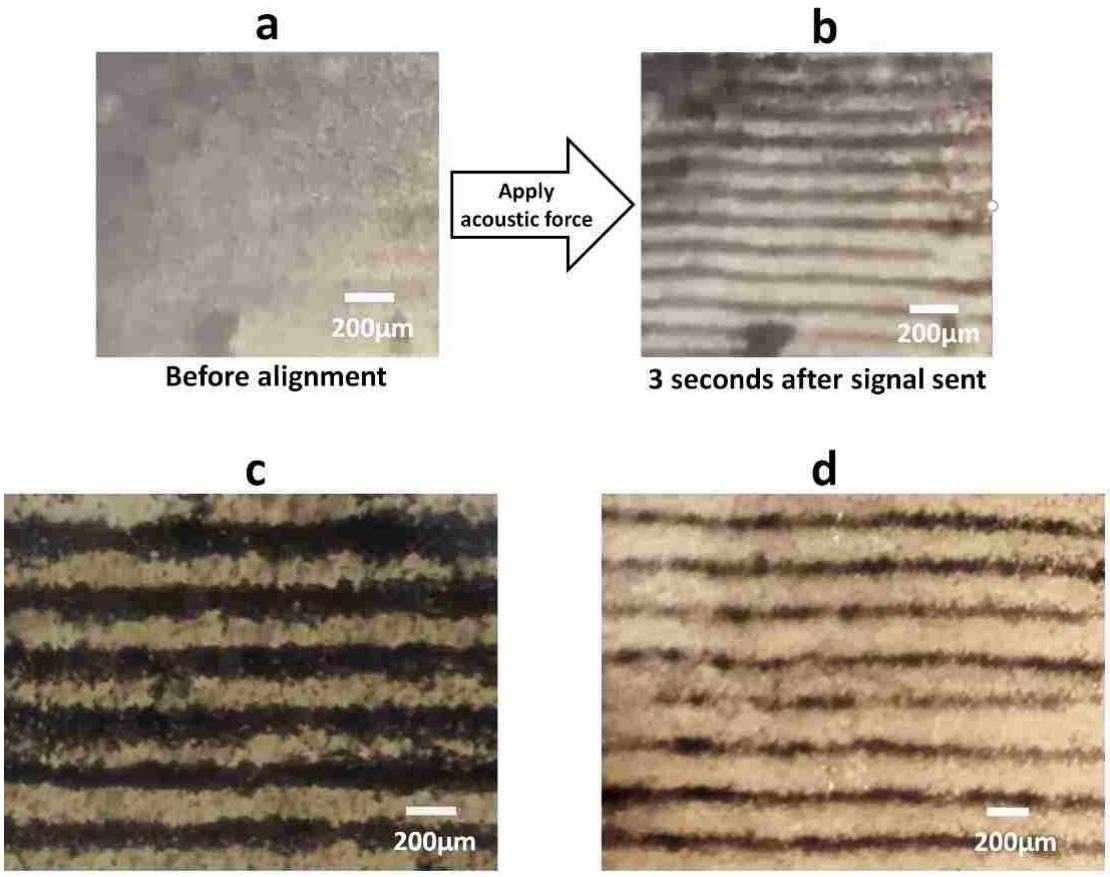

Figure 4-5 (a) Material with 2 wt% magnetic nanoparticles before alignment; (b) Material with 2 wt% magnetic nanoparticles aligned under acoustic force; (c) Material with 6 wt% magnetic nanoparticles are aligned into 105 μm lines (240μm line distance); (d) Material with 1 wt% magnetic nanoparticles are aligned into 30 μm lines (240μm line distance).

Based on the experimental setup, there are three working frequencies founded, 5.95 MHz, 3.125 MHz and 1.97 MHz. The wavelength $\lambda = c/f$, where c is the speed of sound

and f is the resonant frequency. The speed of sound c in the experimental material is ~1500 m/s. This gives two corresponding wavelengths, 252 μm, 480 μm, and 760 μm. Therefore, distances of two nearby lines of accumulated particle can be 126 μm, 240 μm, and 380 μm, which is half of the corresponding wavelengths. The amplitude of the signal is 70V. As shown in Figure 4-5(a-b), magnetic nanoparticles that are randomly distributed in the resin (2 wt%) can be aligned within 3 seconds at a resonant frequency of 5.95MHz. The concentration of magnetic nanoparticles will affect the width of the lines and influence the working frequencies (±0.5 MHz). As shown in Figure 4-5(c), particle lines in 105 μm width are generated with 6 wt% magnetic nanoparticles, while particle lines in 30 μm width are generated with 1 wt% magnetic nanoparticles (Figure 4-5(b)). The maximum width of lines can be generated in this experimental setup is 180μm with 10 wt% magnetic nanoparticles.

Using this method, a microfluidic portable gear with a fixed post axis are in situ fabricated in a glass microfluidic channels (Figure 4-6(a)). The gear has aligned magnetic nanoparticles embedded. The distance of lines is 240 μm and the average line width is 180 μm. A neodymium magnet is applied to generate the magnetic field for controlling the rotation of the gear. The magnet is in a rectangular shape with north and south poles on opposite side, and it is placed right below the microfluidic device. Driven by a stepper motor, the magnet can rotate along the Z axis and manipulate the rotation of the gear inside the microfluidic device. The rotation angle of the gear follows the same as the magnet's when the spinning speed is slow (less than 90rpm). A minimum rotation angle of 5 degree can be accurately controlled when the microfluidic device is filled with Isopropyl Alcohol 99%. The minimum rotation angle is related with media inside the microfluidic device. As

shown in Figure 4-6(b), the gear rotation is remotely controlled by the magnet field. When the spinning speed of the magnet is too fast, the gear cannot follow the speed, and the rotation will be messed up by the continuous spinning of the magnet. To achieve a faster spinning speed, the magnet can rotate fast and give the gear an initial actuation. Then the magnet is quickly removed to avoid the influence on the gear. This can potentially provide a faster rotation for a short period of time. However, the later method is hard to be accurately controlled.

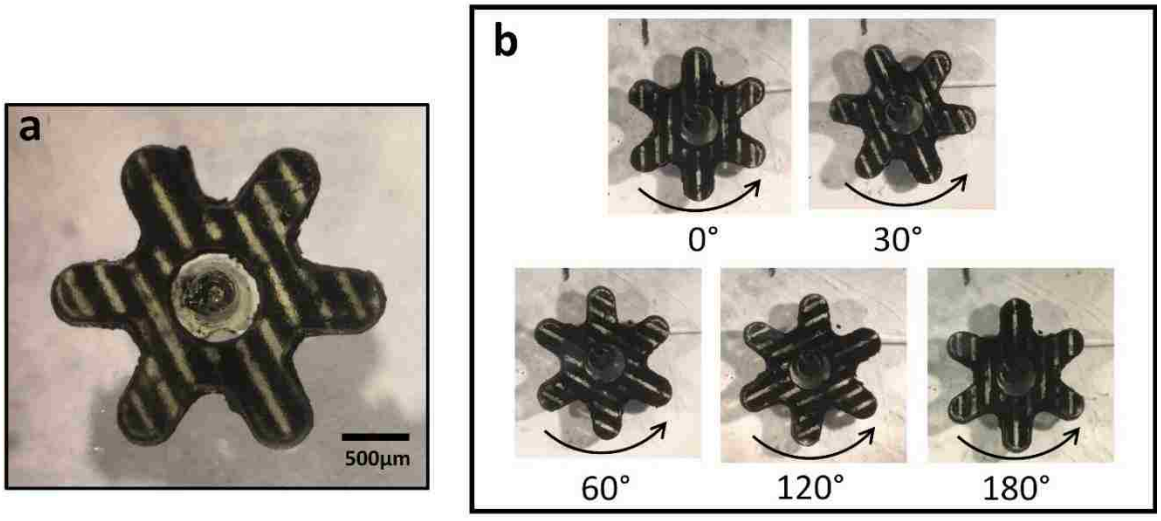

Figure 4-6 (a) An in situ fabricated microfluidic gear with a fixed post axis inside a microfluidic device; (b) Remotely control of the rotation by the magnet field.

This presented technique provided more advanced ways in fabricating microfluidic actuators, including in situ fabrication, remotely controlled actuating, and precise control of the rotation angle. These three unique features are highly desired in microfluidic fields and they are hard to be fabricated from techniques in prior arts[92]. The combination of these three features offers a complete novel technique to in situ fabricate microfluidic actuators with precisely controlled movement, making it suitable for many potential

microfluidic application including micromixers[96][97], sorting[98][92], and micropumps[99]. As the technique can provide customized actuating structure, not only limited by the gears, various of micro-actuating systems can be potentially generated, such as microvalves[100].

4.4 Experimental Setups

The diameter of the magnetite nanoparticles used in this research is ~300 nm (from Alpha Chemicals). The inhibition light source is an OmniCure S1500 curing system with 365nm filters. The initiating light source is a LED with 473nm wavelength. The signal generator used in this research is Agilent 33120A with 15MHz sine and square wave outputs. The signal was then amplified by a NMR-300L amplifier. The piezo elements used are a pair of piezoelectric ceramic plates from Steminc (Steiner & Martins, Inc.). The monomer, photoinitiator and photoinhibitor used in this project have described in 4.2.1.

4.5 Extensions

In recent years, 3D printing has gained significant interest due its capability in fabricating complex and customized structures that cannot be simply fabricated by other approaches, such as 3D objects with internal structures. However, in microfluidic area, it has been a dream to directly apply 3D printing inside the microfluidic channels. None of the 3D printers are able to allow the entire 3D printing process happens within a microscale closed region. To achieve layer by layer fabrication, 3D printing normally requires at least one linear system, which cannot be embedded within such a small microfluidic channel. On the other hand, due to the increasing application in microfluidics, especially in

biological fields that require geometric manipulation, in situ 3D printing in microfluidics can be a versatile tool to boost the research work.

Derived from the light inhibition principle developed in Chapter 4, there are potentials for a novel approach which can enable the in situ 3D printing in microfluidic devices. Instead of using any mechanical motion system, the additive manufacturing process is control by gradually reducing the intensity of inhibiting light. Since this method can be 3used in microfluidic devices with any optical transparent materials and does not require any mechanical actuation systems, it will have great potential in fabricating various complex 3D microstructures in situ, which cannot be achieved by any current technologies.

Figure 4-7(a) shows the schematic of in situ microfluidic 3D printing method based on the two-color lithography system. This method also utilizes a dichroic longpass filter to allow both the 473nm initiation light and 365nm inhibition light to project from the same direction towards the photocurable resin. As the inhibition theory described in 4.2.1, the initiation light will penetrate deeper into the resin while the inhibition light can form an uncured (inhibition) layer between the polymerized object and the substrate. If the initiation light intensity and photocurable material properties remain the same, the inhibition layer thickness is determined by the intensity of the inhibition light. In the first curing status shown in Figure 4-7(b), the majority of the area has been inhibited under the strong inhibition light. Only a thin layer can be polymerized by the penetrated initiation light. Next the intensity of the inhibition light is reduced, creating a new layer that can be cured by initiation light (beyond the inhibition range). Then this layer is exposed under the 473nm curing light and the polymerized structures can bond tightly with the previous cured object. This reducing light intensity and polymerization process continuous until a target 3D object

is completely fabricated inside the device. By tuning the inhibition effect, fresh new layers (able to be polymerized layers) can be gradually generated. This replaces the vertical mechanical actuators which is necessary for all the 3D printer devices. While reducing the inhibition light intensity to create a fresh new layer, the initiation light will also be slightly reduced, because the initiation light can cure more than the thickness of the fresh new layer if the initiation light intensity is not reduced. Otherwise the 3D structures that are able to be printed will be limited.

This method has potential to achieve layer-less 3D printing. The first step of a typical SLA-DLP based 3d printing is to slice a 3D model into layer-by-layer images. The number of images created depends on the layer thickness selected. The thinner the layer thickness, the more layers as well as images will be used to expose during the 3D printing process. More details of the 3D model can also be fabricated by using thinner sliced layer. In this method, the sliced layer thickness can be set very thin, such as 1μm. During the printing process, instead of exposing these sliced images one by one, an animated movie that is composed of these images is displayed and projected to the photocurable resin along with the initiation light. At the meantime, the inhibition light intensity is gradually decreased. The decreasing rate of the light intensity will be synchronized with the frame rate of the movie. The smooth transitions of exposure images can potentially eliminate the layer-by-layer effect on the fabricated 3D objects. This extension is expected to provide a potential innovation based on the theory developed in this chapter.

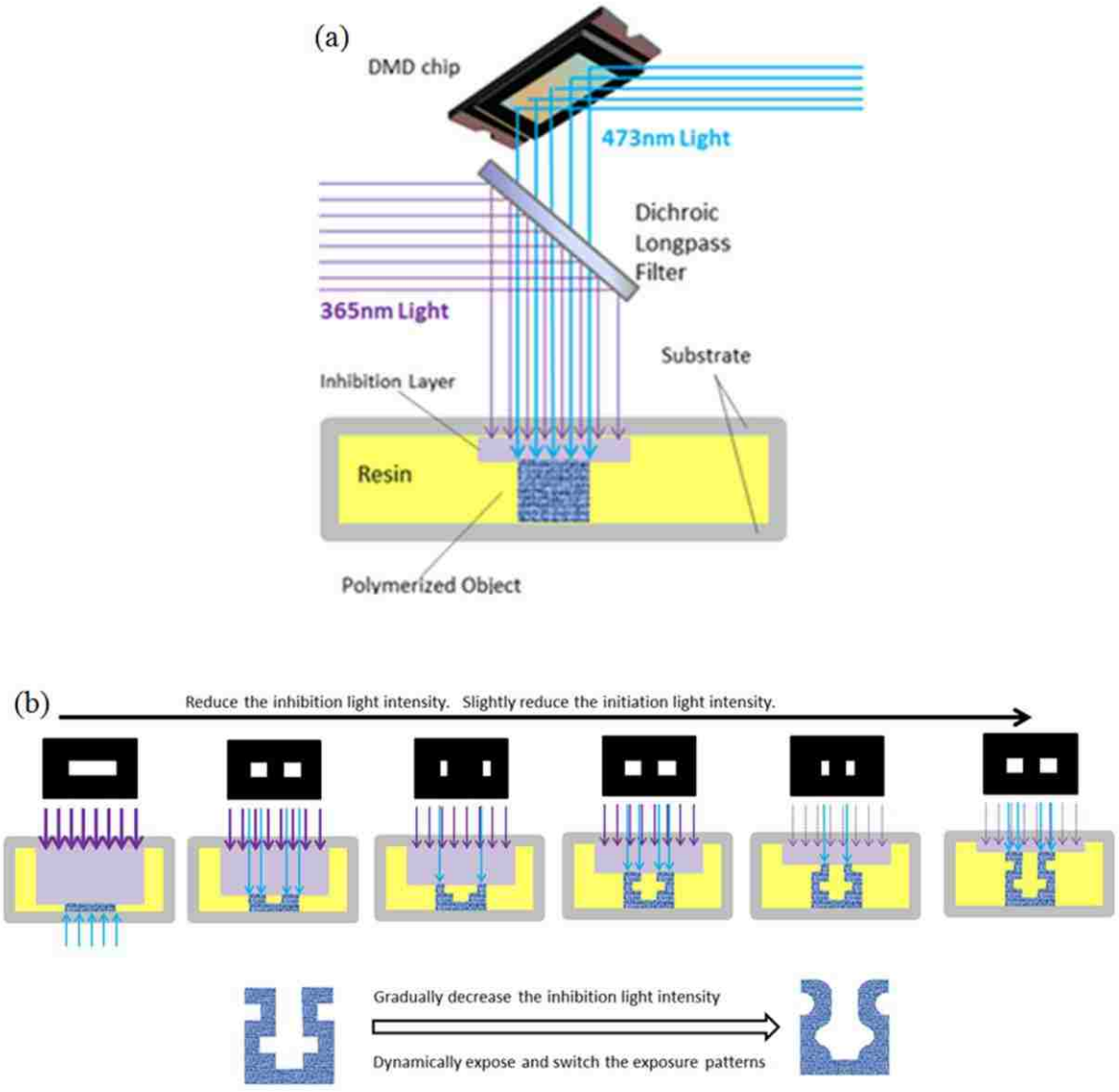

Figure 4-7 (a) Schematic of the in situ 3D printing setup; (b) Remote control of the fabricated microstructures via magnetic field.

Chapter 5 : Additive Manufacturing of Large-Scale Three-Dimensional Structures Based on Scanning Lithography

5.1 Introduction

The recent explosion of the 3D printing market has made fast and low-cost prototyping possible[101][102]. However, consumers desire improvements to the performance metrics of these machines, mainly printing speed, resolution, size and material choice[103][104][105][106][107][108]. While the most common printing methods, fused deposition modeling (FDM)[109] and SLA[110], work well for rapid prototyping, they must be improved upon to keep up with market demands[111]. Advancements to the technology extend the reach of potential applications to include biomedical[112], dental[113], jewelry[114], and production-level uses[115].

Improving upon the developments in laser based SLA printing, digital light processing (DLP) based on Digital Micro-mirror Device (DMD) enables faster fabrication[20][116][78]. The disadvantage of laser based SLA printing is that the laser must focus on a small area and follow a specific path to draw the image of each layer. The laser pathway is observable and therefore not smooth on the printed body. Therefore, the traditional laser based SLA slows down the printing process and lowers the X-Y resolution. Lu's group uses a projector with a UV light source and a DMD chip instead of a laser[117]. The projector exposes an image onto the build area to polymerize the entire layer at once. Such a method avoids drawing the image through a specific path, which eliminates the

surface scars seen with SLA printing. As a result, the DLP method yields faster print times and higher print resolution. Based off of the DLP developments, DeSimone's group developed the technique of Continuous Liquid Interface Production (CLIP) [118]. The machine projects a continuous sequence of UV images through an oxygen-permeable membrane which inhibits polymerization at the border. The build plate is continuously pulled out of the resin (a bottom-up approach), where the speed is only inhibited by curing times. The technology increases printing speed due to the continuous movement. Despite these improvements, these machines are still limited in size of their build area. On the other hand, the fabrication of large objects with intricate details have increasingly demands. In biological and medical areas, microfluidic devices with more complex control system and structures are expected to further facilitate the research work[5][6]. Therefore, the large-scale microfluidic system, which allows more components and independents control operations to be embedded in a single device, becomes a problem. For example, a complex microfluidic logic circuit for arbitrarily controlling flows is composed of several pieces of small devices that are fabricated separately[7]. However, the connection and alignment can be an issue which requires more complicated process and can affect the experimental results. As another example, microfluidic devices fabricated by traditional clean room lithography has limited inlets numbers to allow multiple injections[6]. If more inlets and channels are required, creating an integrated large-scale microfluidic device is a better way to solve the problem.

To increase the build area for large-scale printing, Lee et al. produced a DLP-based printer with motors for two-dimensional (X and Y) axial movement[119]. The printer incorporates the basics developed by Lu et al., but divides the layer image into overlapping

sub-region images. In this system, the projector exposes the resin underneath to the sub-region image, and then sequentially moves to the next sub-region. The technology greatly enhances build area size and is also scalable, as the algorithm is capable of processing larger parts than the current printer can handle. However, this technique is still lacking in speed and quality. In particular, the algorithm requires the projector to expose each sub-region individually. The projector must decelerate, stop, and re-accelerate for each sub-region, wasting time during projector movement. Since larger objects require more sub-regions, scaling up the system further increases the amount of wasted time. Also, division of images into sub-regions inherently creates flaws in the resolution, as the borders of each sub-region must be stitched together creating seams between each sub-region.

In this research, a technology has been developed to allow smoother and faster large-scale printing. Printing resolution is improved by slicing each layer image into large sub-region "strips" and transforming it into an animated image. The motor and animated image move synchronously and as a result, a still image appears on the build plate as the projector smoothly passes over and exposes. The algorithm greatly reduces the amount of stitching needed, improving print resolution. It also utilizes the time during scanning projection more efficiently, requiring fewer pauses than previous technologies. The printer and algorithm are both scalable technology; printing size and resolution can be improved for even larger prints with even higher resolution. Our technology is designed for industry professionals, research scientists, and even DIY users—anyone who needs large parts with fine resolution.

5.2 Method and Materials

5.2.1 Theory and Algorithm

DLP based 3D printing methods require two key elements: a build platform which holds the printed objects, and a projecting system that utilizes the DMD to reflect light and expose patterned images. The DMD used in this research has 1200 × 800 micro-mirrors, which individually rotate to reflect the UV light and polymerize the photocurable resin.

The pixels projected on the resin, corresponding to the individual mirrors of the DMD, determine the theoretical resolution of the projected pattern. During the light exposure process, traditional DLP printing methods fix the position of both the projecting systems and the build platform to enable steady polymerization in target area. The technology presented in this project utilizes a unique scanning lithography technology that allows the projecting device to move continuously and project animated patterns when printing objects (Figure 5-1). The area exposed to UV light in the printing layer gradually cures during the scanning of the projecting device. When the photocurable resin is exposed to the UV light in the oxygen-rich environment of the air, a thin layer of uncured resin remains on the top of the cured surface due to the oxygen inhibiting effect of UV induced polymerization. To cure the photocurable resin with a preset thickness, a certain exposure time of UV light is required in an environment of fixed light intensity and oxygen concentration. In this printing technology, the target curing area is exposed continuously and repeatedly by the UV light reflected by the DMD array. The overall exposure time, light intensity, monomer reactivity, oxygen solubility and diffusivity into the photocurable resin are considered to ensure a sufficient and proper curing thickness.

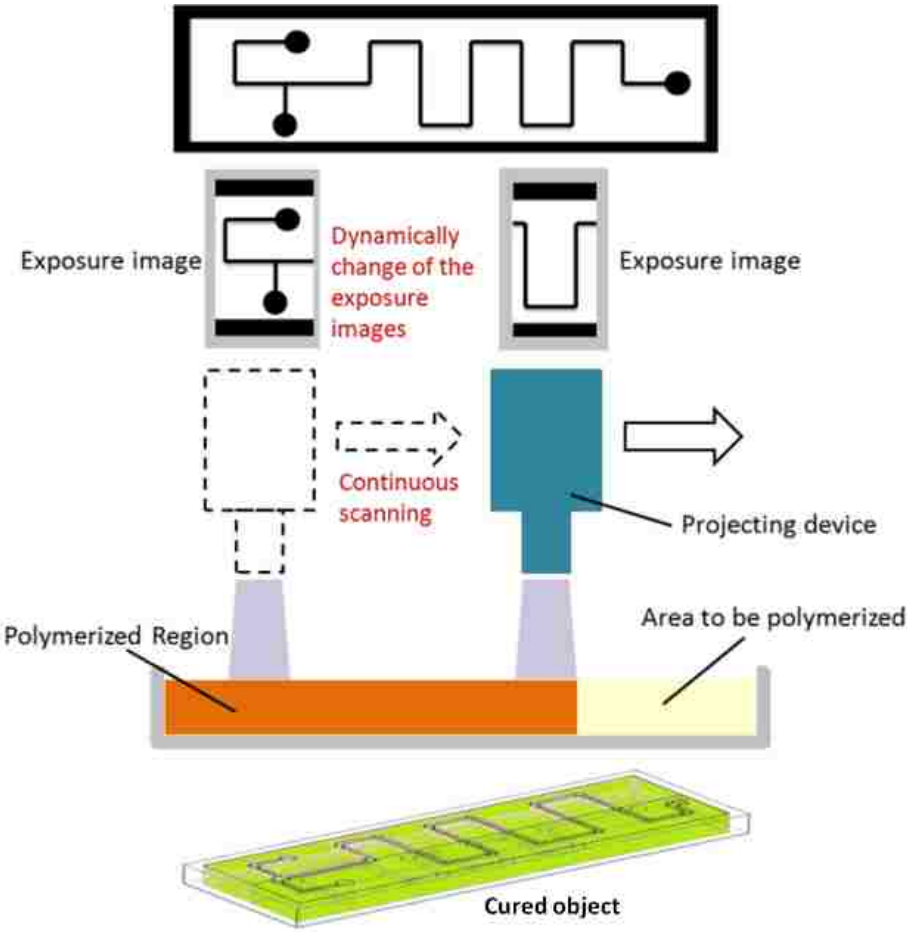

Figure 5-1 Schematic of scanning projection method.

The key aspect of the technology is the dynamic shifting process of pixels. A micro-mirror is activated when the reflected UV light enters the target printing area. Traditional DLP printing methods are static—controlling each pixel by activating the single corresponding micro-mirror on the DMD once per layer. Our pixel shifting process, however, controls each pixel by sequentially activating micro-mirrors as the projecting system scans along a pathway. Each pixel in the pattern is exposed under the UV light in sequence, reflected from micro-mirrors in the corresponding column array. The projecting image changes when the projecting device moves one pixel's distance as it scans over the build platform. These projecting images can be regarded as individual frames of a "movie"

that play at the same speed as the movement of the projecting device. The total frames and frame rate of the "movie" depend on the scanning speed of the projection device, pixel size, and printing area size.

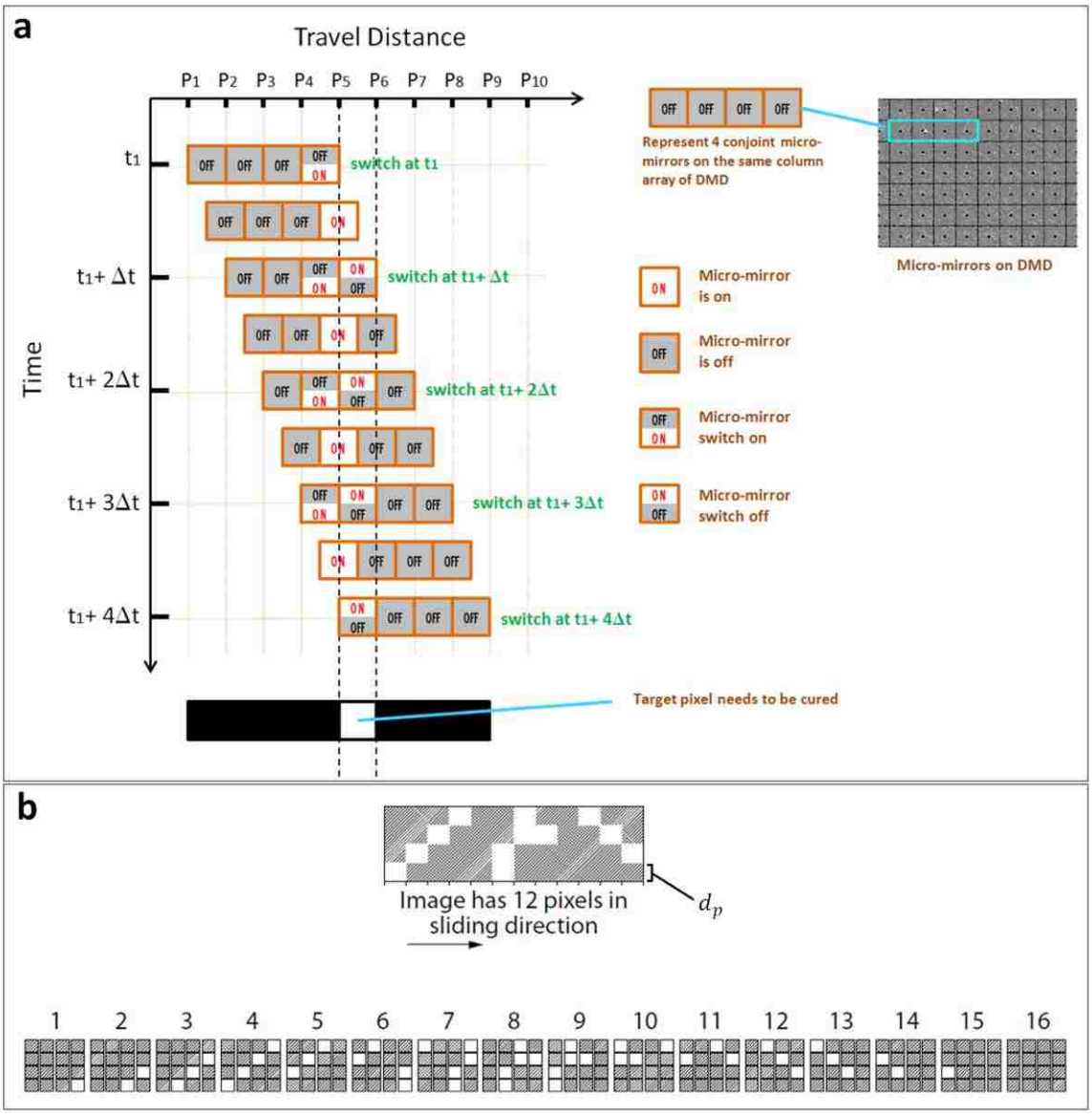

Figure 5-2 (a) The illustration of dynamic shifting process of pixels; (b) An example of frame divisions.

For example, as Figure 5-2(a) shows, to cure a certain pixel's area, one mirror on the first row of DMD is activated (i.e., starts to reflect the light) just before entering the

target curing area. After the projecting device moves one pixel's distance, the second mirror is activated and the previous activated mirror is disabled. This process of activation and deactivation of the mirrors continues until last mirror passes over the target area. Figure 5-2(b) shows an example of how the frames are chosen to cure the target patterns. In this instance, the DMD has 4x4 mirrors and the target printing pattern can be regarded as an image of 4x12 pixels. The printing pattern is therefore divided into 16 frames. The projector will sequentially expose each frame, and then move a distance of one pixel. The equations for one-directional scanning of the projecting device can be expressed as:

$$t_f = \frac{d_p}{v_d} \tag{5}$$

$$t_0 = t_f \times n_p \tag{6}$$

$$n_f = n_d + n_p \tag{7}$$

where t_f is the exposure time of each frame, d_p is the printing resolution (the size of each pixel when projected onto the built plate with units of μm), v_d is the DMD scanning speed, t_0 is the total exposure time of each printing pixel (curing time), n_f is the number of frames needed to be created for each printing layer, n_p is the number of micro-mirrors on DMD (in scanning direction), and n_d is the number of pixels arranged to the overall printing pattern on each layer (in scanning direction). For the example in Figure 5-2(b), n_p, n_d, and n_f are 4, 12, and 16, respectively.

To enlarge the total printing area, the projection device travels in the Y direction after the completion of scanning in X direction (Figure 5-3(b)). It then starts another scanning process on this new area. The algorithm overlaps the borders between the sub-regions to ensure polymerized patterns printed in different scanning areas are connected as

an integrated piece. As Figure 5-3(c) shows, the overlapped region has a width of one pixel and grayscale is applied to avoid over-curing. The grayscale value of an image determines the light intensity of the pixels, varying from black at the weakest intensity (grayscale value =0) to white at the strongest intensity (grayscale value =255). For this printing material, the grayscale value in overlapped regions was set to 210.

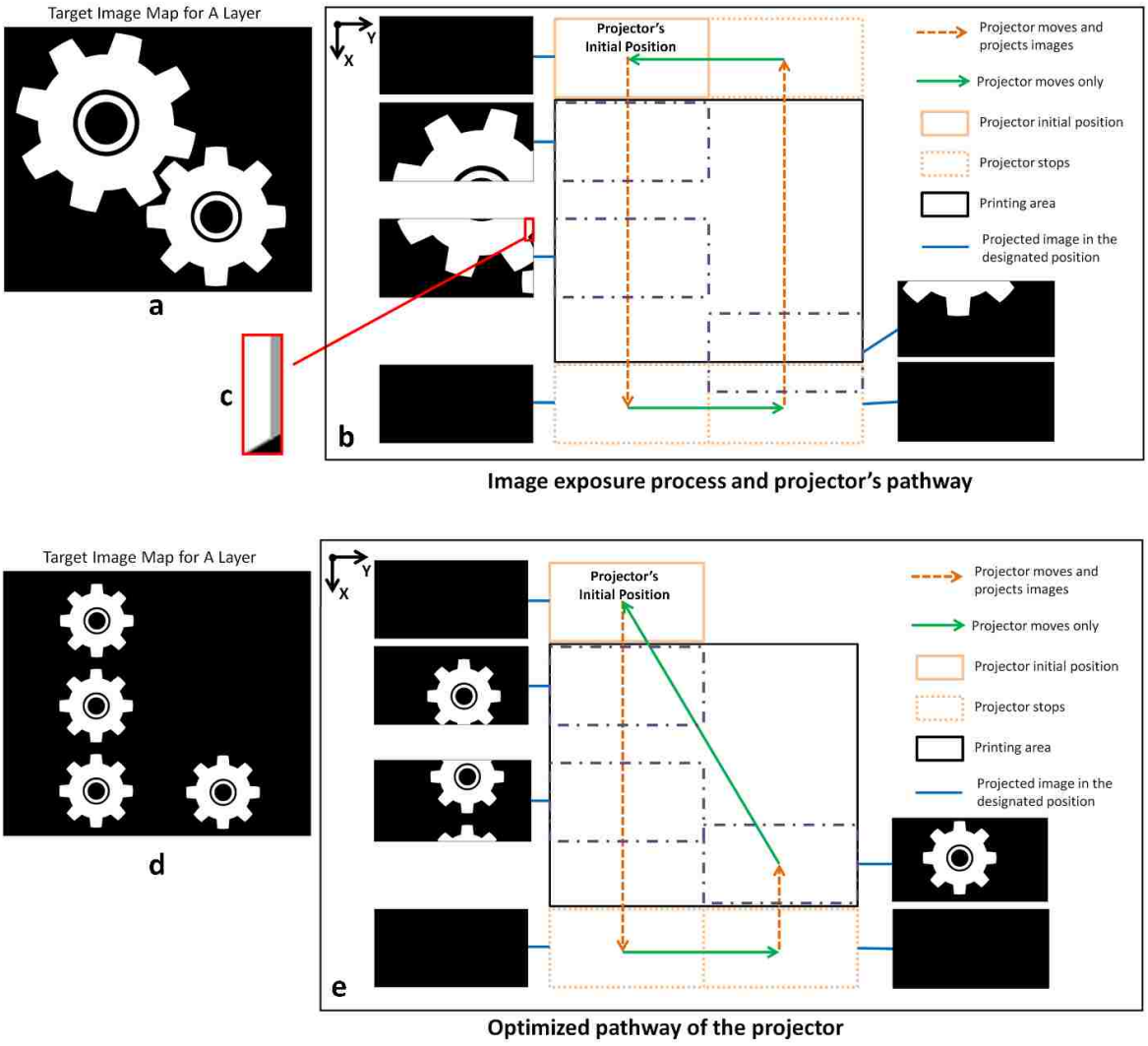

Figure 5-3 (a) A target image map for a layer; (b) Illustration of the image exposure process and projector's pathway; (c) The illustration of the grayscale region; (d) A target image map where the printing object only occupies part of the entire build area; (e) The optimized pathway of the projector for the image map in (d).

To further improve the printing efficiency, the scanning pathway is altered when then the printing pattern in a layer only occupies part of the entire build area. To print the pattern in Figure 5-3(d), the projecting device follows the pathway shown in Figure 5-3(e) to greatly enhance the printing speed due to the shorter travel distance. To print a 3D object, the size and shape of each layer image can vary greatly. Therefore, this method provides a highly efficient algorithm that optimizes the scanning pathways for each unique printing layer.

Although grayscale is applied on the overlapped bonding regions, bonding lines still exist in X direction because the two regions are not polymerized at the same time. These lines make the printed object easier to fracture under bending stress. To mitigate this issue, the projector pathway differs slightly between two sequential layers. As shown in Figure 5-4, the projector pathway is shifted in layer N+1 when compared with layer N. Then in layer N+2, the projector pathway returns to the same as the pathway used in layer N. This method avoids the generation of bonding layers in the same location for all layers. The printed objects, as a result, can be regarded as a single, integrated piece.

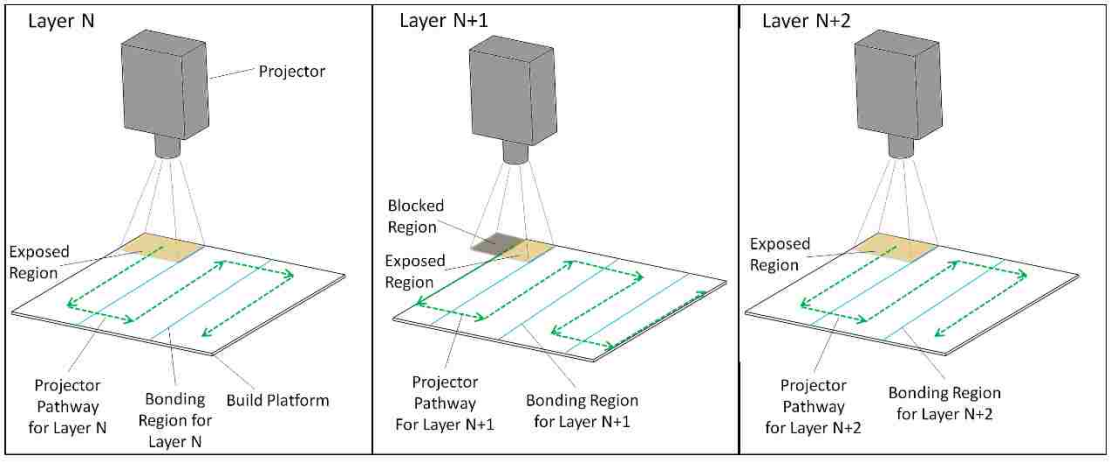

Figure 5-4 An illustration of pathway shifting method.

5.2.2 Prototype of a scanning lithography 3D printer

An illustration of the printer's prototype is shown in Figure 5-5. The structure of our prototype is 900mm wide by 600mm deep by 850mm tall. Inside the structure is a build plate capable of producing prints 500mm wide by 450mm deep by 400mm tall. The projecting device is a light engine with the DMD (WXGA 1280x800 chipset) from Texas Instruments. The light source is a 25W LED at a wavelength of 405nm. Original lenses in the optical system of the light engine were replaced with heat resistant lenses. The final output power is greater than 1.5W in the 405nm wavelength. The pixel size, which determines the printing resolution, can be adjusted by the optical system on the projecting device. The current printer can achieve a pixel size ranging from 36μm to 160μm. The scanning speed can be adjusted from 5mm/s to 30mm/s, depending on the material. The level of the projector, the wiper and the build platform can all be tuned to ensure accurate relative positions. Lastly, at the bottom is a 135-liter resin tank and supporting features. As a result, this printing technology provides a scalable approach to achieve a printing resolution of 36 μm with a build volume of 500mm×450mm×400mm.

To ensure high resolution of the printed part, there must be a smooth, even layer of resin on the top surface. In this printing method, the newly exposed layer bonds to the previous layer below it; without an even coating of resin, the printed part is subject to surface roughness, drooping layers, and curling of the part (especially in the beginning layers). These flaws are both aesthetically and functionally unacceptable. The problem with the approach of submerging in and reemerging the part from the resin is that surface tension creates an uneven layer on the surface; more viscous resins exacerbate the issue. To resolve this problem, the printer includes a wiper that moves across the build plate after it

reemerges to the surface. The blade of the wiper sits below the surface to break the surface tension of the resin and wipe an even and smooth layer of resin. As a result, higher viscosity resin can be used in printing. In our printing process, the projecting system first cures a layer of resin on the build platform. Next, the platform moves to submerge and re-emerge from the resin tank to form a new layer on top of the cured layers. Due to the surface tension of the resin, a convex layer of liquid resin forms above the cured resin level. The wiper then travels over the platform to flatten the surface prior to curing and the process repeats.

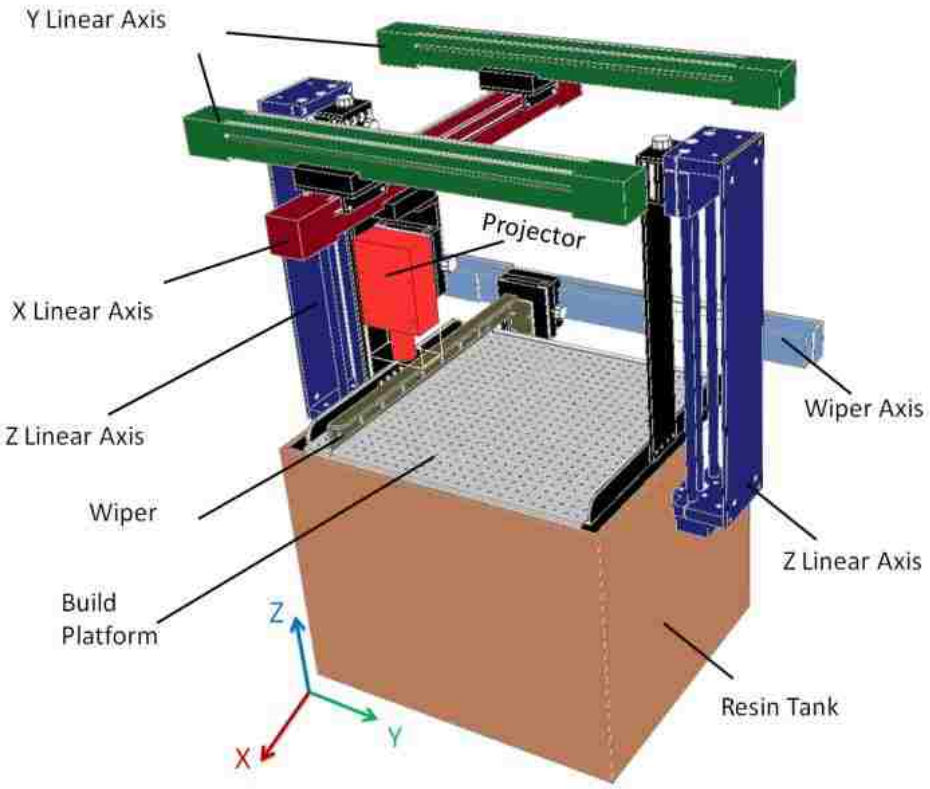

Figure 5-5 An illustration of the prototype of the 3D printer.

5.2.3 Control Software Development

The control software is developed using Java and the JavaFX platform. The main purpose of the software includes: creating an exposure sequence based on loaded 3D

models and user specifications; operating the linear actuation system including X, Y, and Z stages as well as the wiper; controlling other electronic elements such as fans, heaters and sensors; and reading and displaying sliced images onto the projector during the printing process. During the exposure sequence creation, user-selected STL files of the 3D models are loaded into the software and sliced into horizontal slices. The slicer then converts these slices into PNG image files where white (grayscale value = 255) corresponds to structured areas and black (grayscale value = 0) corresponds to void spaces. The user can manually adjust the printer settings or load pre-made settings from a file. When the print sequence begins, the sliced images are manipulated so that the projector displays the image layer as a "movie". The printing process is described in the flow chart in Figure 5-6.

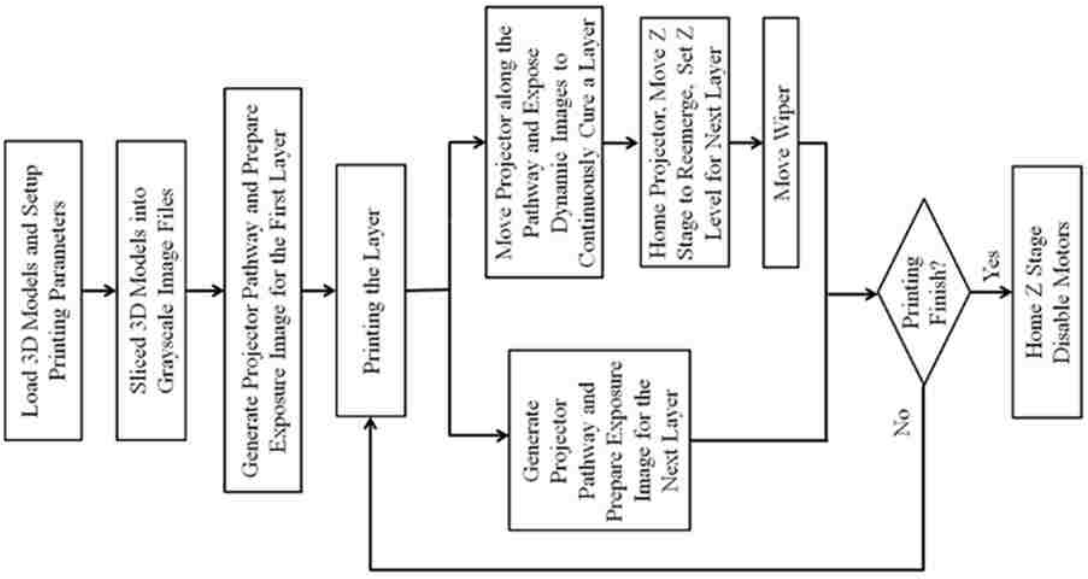

Figure 5-6 Flow chart of the printing process.

5.3 Results and Analysis

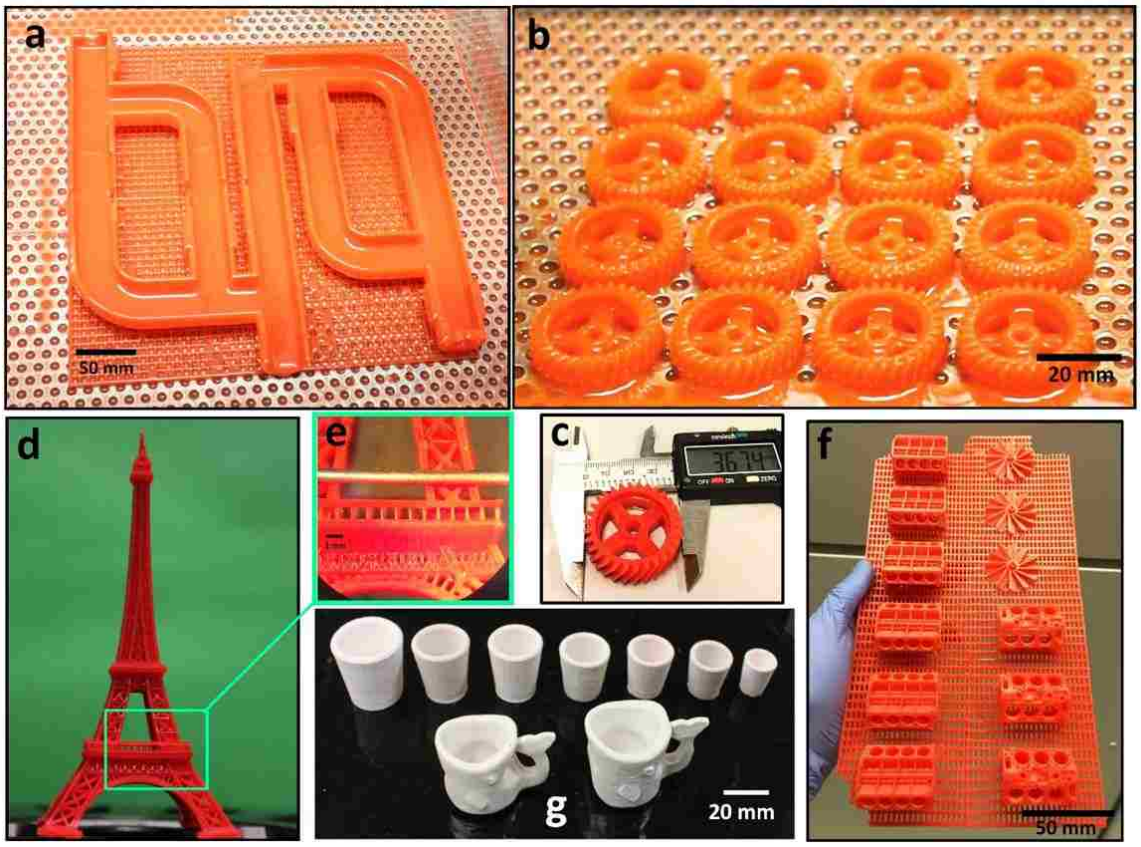

Figure 5-7 Printed samples: (a) A pipe network; (b) Batch of gears; (c) The measured size of a single gear from (b); (d) An Eiffel Tower; (e) The detailed features of the printed Eiffel Tower in (d); (f) A set of engine models; (g) Samples of the 3D-printed ceramic parts.

Using this technology, we managed to print parts with a wide range of sizes. Shown in Figure 5-7(a) is a pipe network with a size of 400mm×380mm in the XY plane. This sample demonstrates the large-volume capabilities that otherwise cannot be achieved by most DLP-based 3D printers. In Figure 5-7(b)-(c), a batch of gears with an outside diameter of 36.74mm are produced within 1 hour, showing this technology's superior performance in large volume production. A movie that shows the printing process of the gears is shown in Supplemental 1. In Figure 5-7(d), the Eiffel Tower—a typical 3D printing model—is

printed with intricate details, including microscale parts. The vertical posts, for instance, in Figure 5-7(e) have a width of 150μm. This Eiffel Tower model proves the capability of printing complex structures and strong bonding of layers. In Figure 5-7(f), a set of engine models are printed within 2 hours.

Furthermore, this printing method is capable of printing ceramic suspension material, which is a mixture of ceramic powders and photocurable resin. Dense ceramic objects can be generated after the 3D printed parts are post-processed. This is typically accomplished by burning out the organic materials in photocurable resin and high-temperature sintering. Achieving a uniform resin layer thickness for each printing layer is a key challenge for ceramic suspension printing due to the increased viscosity of the material[108]. By utilizing a wiper, the technology is capable of producing a 150μm layer thickness before post-processing. Samples of the 3D-printed ceramic parts are shown in Figure 5-7(g).

To characterize various minimum-sized features that can be printed by the technology, objects with microscale features are printed as shown in Figure 5-8. Figure 5-8(a) shows vertical walls with varying gap distance; a minimum gap 72μm with clear boundaries is achieved. Also, a single pillar with the width of 74μm is printed (Figure 5-8(b)); the pillar is straight and clearly distinct. This achievement is significant because small- scale circular features are normally hard to produce in large scale 3D printing. Figure 5-8(c) demonstrates the ability of this method in producing small scale circular walls, in this case, a blood vessel sample is printed. The cross-section microscope image illustrates that a uniform circular channel with wall thickness around 84μm is well formed (Figure

5-8(d)). The layer thickness set in these printed objects is 25 µm and the pixel size set from the projecting system is 36µm.

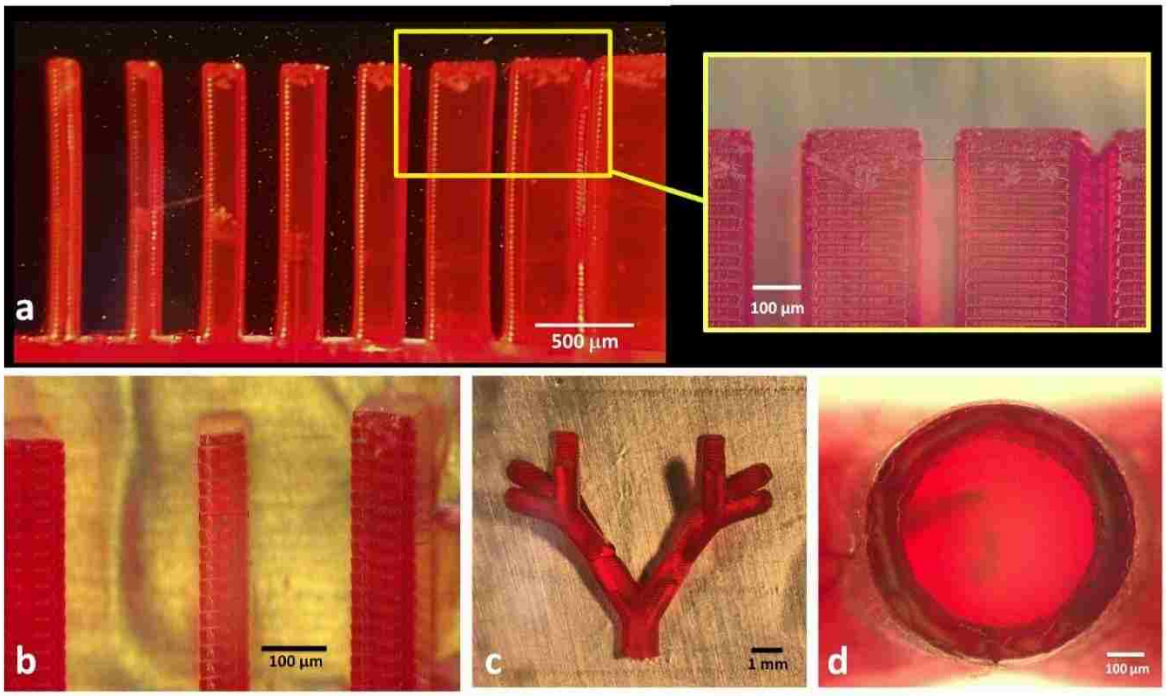

Figure 5-8 Characterization of minimum printable features under microscope: (a) 3D printed vertical walls with a minimum gap of 72µm; (b) 3D printed pillars with the minimum width of 74µm; (c) 3D printed blood vessel sample with through channels; (d) The circular cross-section of the blood vessel in (c) with 84 µm wall thickness.

Our scanning lithography method can produce more integrated polymerized objects when compared with other large scale DLP printing method. The one developed by Lee's group[119] has inevitable bonding lines in both X and Y travel pathways (shown in Figure 5-9(a)). Such bonding lines make the printed object easier to fracture under bending stress, in regard to material properties. To characterize the Young's modulus of printed objects based on different printing methods, a standard three-point loading system is utilized to measure the flexural properties (shown in Figure 5-9(b)). In the flexural property tests, we used printed samples from three different printing methods, our scanning lithography

printing, regular DLP printing and sequential step-by-step printing. The data of "before post-cured" are obtained based on 100μm layer thickness without additional treatment. The data of "after post-cured" are obtained after exposing printed samples under 18W UV light source with four UV LEDs (two 405nm ones and two 365nm ones) for 90 minutes at 50ºC. The dimensions for the printed specimens are 5mm wide, 2mm thick, and 12.7mm long. These specimens are tested flatwise on the support span. The flexural stress σ_f can be calculated by the following equation:

$$\sigma_f = \frac{3PL}{2bd^2} \quad (8)$$

where P is the maximum load(force) before fracture, L is the support span, b is the width of the specimen, and d is the depth of the specimen. In this measurement, L, b, and d are 10mm, 5mm, and 2mm, respectively.

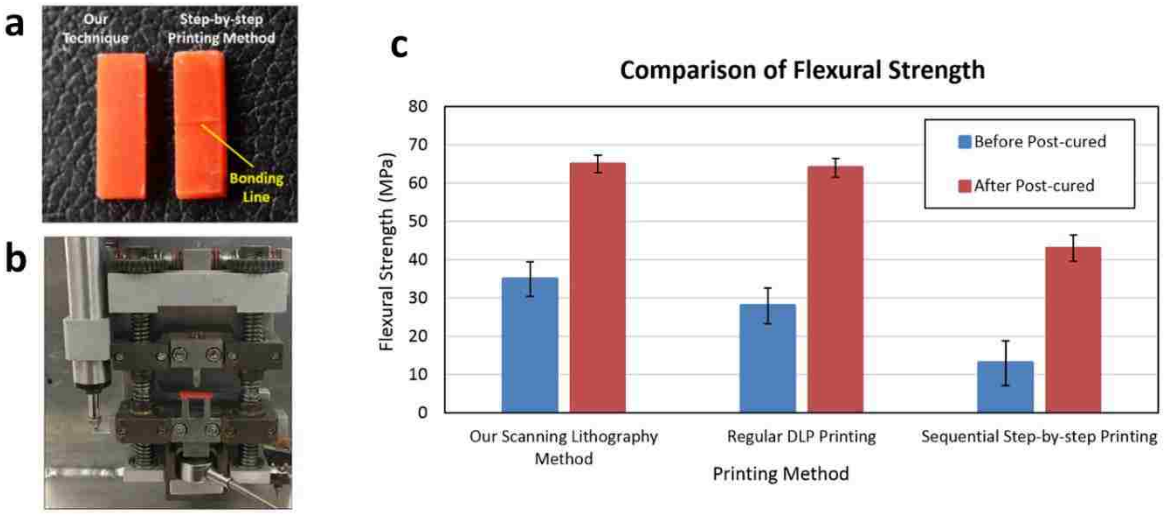

Figure 5-9 (a) An illustration of the bonding line; (b) A three-point loading system with a test specimen of rectangular cross-section rests on two supports in a flat-wise portion; (c) Comparison of mean flexural strength.

The comparison of mean flexural strengths between each printing method are shown in Figure 8. All specimens are printed using the same prototyping resin. Above, it was observed that our continuous scanning technology is capable of printing large objects that otherwise cannot be printed by regular DLP printing methods. Here, a 50% increase in flexural strength is observed when compared with the method developed by Lee's group. These results demonstrate that our technology has the capability of producing not only larger, but also stronger parts.

5.4 Materials

The prototyping resin is a mixture of Laromer 6210G (an aromatic modified epoxy acrylate, Eterner Chem. Co.), Laromer TPGDA (Tripropylene Glycol Diacrylate, BASF Co.), Laromer HDDA (Hexane-1,6-diol diacrylate, BASF Co.), ethoxylatedtrimethylolpropanetriacrylate (TMP3EOTA, Eterner Chem. Co.), and Lauryl acrylate (Esstech Inc.). Irgacure 754 (a mixture of Oxy-phenyl-acetic acid 2-[2-oxo-2-phenyl-acetoxy-ethoxy]-ethyl ester and Oxy-phenyl-acetic acid 2-[2-hydroxy-ethoxy]-ethyl ester) and Irgacure 4265 (a mixture of Diphenyl (2,4,6-trimethylbenzoyl-phosphine oxide and 2-Hydroxy-2-methyl-1-phenyl-propan-1-one)) from BASF Co. was used as photoinitiators. 0.2%wt. Tinopal OB (BASF Co.) is used as a UV absorber. The resin was pigmented by Microlith Red 3630 K (BASF Co.).

5.5 Conclusions

Through this research, a scanning lithography technology that enables the printing of large objects with intricate details is developed. A minimum feature of 74 μm and a build size of 400mm×380mm in the XY plane is achieved. This 3D printing method can serve as a scalable technology that enables larger, customized build volumes (greater than

1 m3). Meanwhile, the micro-scale features and smooth finish retained. With the application of a wiping system, our 3D printing technique is compatible with various materials, such as ceramic resin, leading to the direct manufacturing of final parts from photocurable materials. Furthermore, this technique matches the flexural properties of other smaller-sized DLP 3D printers, showing advantages over existing large-scale DLP printing methods regarding both printing speed and material properties. Our method can be further improved by adding more projectors and moving them simultaneously, further increasing the overall printing speed. This 3D printing technology with the capabilities of large-scale fabrication and mass production is expected to provide ideal solutions in medical, dental, jewelry, automotive, and aerospace industries.

Chapter 6 : Continuously Additive Manufacturing of Unconventional Structures through Oxygen Inhibited Lithography

6.1 Introduction

3D printing or additive manufacturing market is rising rapidly with the growing demand in various applications. As 3D printing techniques have been more and more adopted by industries such as aerospace[120], medical[121], dental[122], jewelry[123], consumer[124], and etc, there are increasing needs of printing high-quality parts in a faster speed[125]. Conventional additive manufacturing techniques involve forming the object by building layers on top of layers[126]. These layer-by-layer printing process typically requires a platform relocating process or a layer recoating process between each layer. The purpose of these processes is to create a new layer of fresh materials that is ready for the printing of next layer. However, the platform relocating or layer recoating processes significantly increase the overall printing time. In SLA based 3D printing, the platform relocating process for each layer can take up to minutes. No real printing work are carried on during the relocating process, Therefore, a few hours are wasted over the entire printing process. Furthermore, layer-by-layer printing will also induce stepping lines on surface, which reduce the smoothness and quality of printed parts. There are methods to eliminate the surface lines, such as spraying micro-sized alcohol droplets, applying coating and machining. However, additional post-processing steps and certain printing materials are

required to make these methods applicable. None of the methods can solve the issue of stepping lines fundamentally.

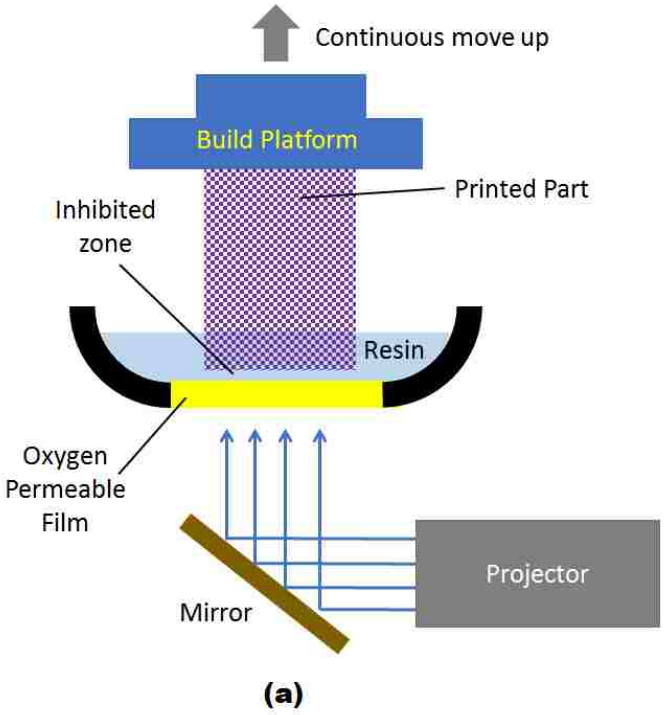

Figure 6-1 (a) Carbon Inc continuous liquid interface production method; (b) Printed samples of M2 3D printer from Carbon Inc.

DeSimone's group invented the technique of Continuous Liquid Interface Production (CLIP) [118] and founded the Carbon Inc. that developed M1 and M2 3D printers (Figure 6-1). Their printers utilize the "bottom-up" (inverted) DLP printing method and allow the build platform to be continuously pulled out of the resin vat. The bottom of the resin vat is an oxygen-permeable membrane that allows the oxygen to inhibit the polymerization on the interface of resin and membrane during the printing process. The technology has the capability to increase the printing speed and achieve layer-less 3D printing. However, even though oxygen can form an inhibition zoon that prevents the

adhesion between printed object and bottom of the vat, vacuum force is still an obstacle when the printed parts has large cross-sections. Since the inhibition zoon is thin, the vacuum force is generated when the build platform is moving up. When curing a layer with large cross-section, the vacuum force can prevent the build platform from continuous moving up, separate the printed parts from the build platform, break the current printed objects and deform the oxygen-permeable membrane. On the other hand, the oxygen-permeable material Carbon Inc. used (PTFE AF 2400[127]) was expensive to be applied in the 3D printing technologies with the same level of build volume. It cannot be re-used once damage is caused.

To provide a solution that can allows the continuous 3D printing with more diverse shapes in an affordable manner, a technology has been developed in this research to achieve fast, layer-less, delicate and large cross-section printing.

6.2 Method and Materials

6.2.1 Basic Principles of Oxygen Inhibition Effect in Photo-induced Polymerization

Initiation, polymerization, and termination are the three stages of reactions in an acrylate-based, free-radical polymerization process, which can be represented by the following equations[128]:

Initiation: $\text{initiator} \xrightarrow{h\nu} R^{\bullet}$ (9)

Polymerization: $R^{\bullet} + M \rightarrow RM^{\bullet}$ (10)

$RM_n^{\bullet} + M \rightarrow RM_{n+1}^{\bullet}$ (11)

Termination: $RM_n^{\bullet} + RM_m^{\bullet} \rightarrow RM_{m+n}$ (12)

where $R^{\bullet}$ is the initiator radicals, M is the acrylic monomer.

The oxygen inhibition effect forms when the free radicals meet the oxygen molecules. In this situation, the oxidized radicals, which are ineffective in the polymerization process, are formed. The reaction between radicals and oxygen molecules can be represented as:

$$R^{\bullet} + O_2 \rightarrow ROO^{\bullet} \quad (13)$$

$$RM_n^{\bullet} + O_2 \rightarrow RM_nOO^{\bullet} \quad (14)$$

$$ROO^{\bullet} + RM_nOO^{\bullet} \rightarrow \text{termination} \quad (15)$$

where $ROO^{\bullet}$ and $RM_nOO^{\bullet}$ are not capable of initiating the polymerization process.

In SLA based 3D printing, the photocurable resin is normally composed by oligomers, monomers, initiators and additives such as pigments, dyes, etc. Initiators can generate radicals after initiation by certain wavelength of light. The radicals can either activate functional groups in oligomers and monomers to lead to polymerization or be inhibited by inhibitors. Oxygen can act as one of the inhibitors, which can contact the initiating radicals to form oxidized-radicals. The UV induced polymerization has the principal advantage of curing solvent-free formulations in a matter of seconds with spatial control. Because of the inhibiting effect of free radical photocuring process, oxygen is normally regarded as a problem. On the other hand, the oxygen inhibition can also be an advantageous when being utilized to control the formation of polymer surface.

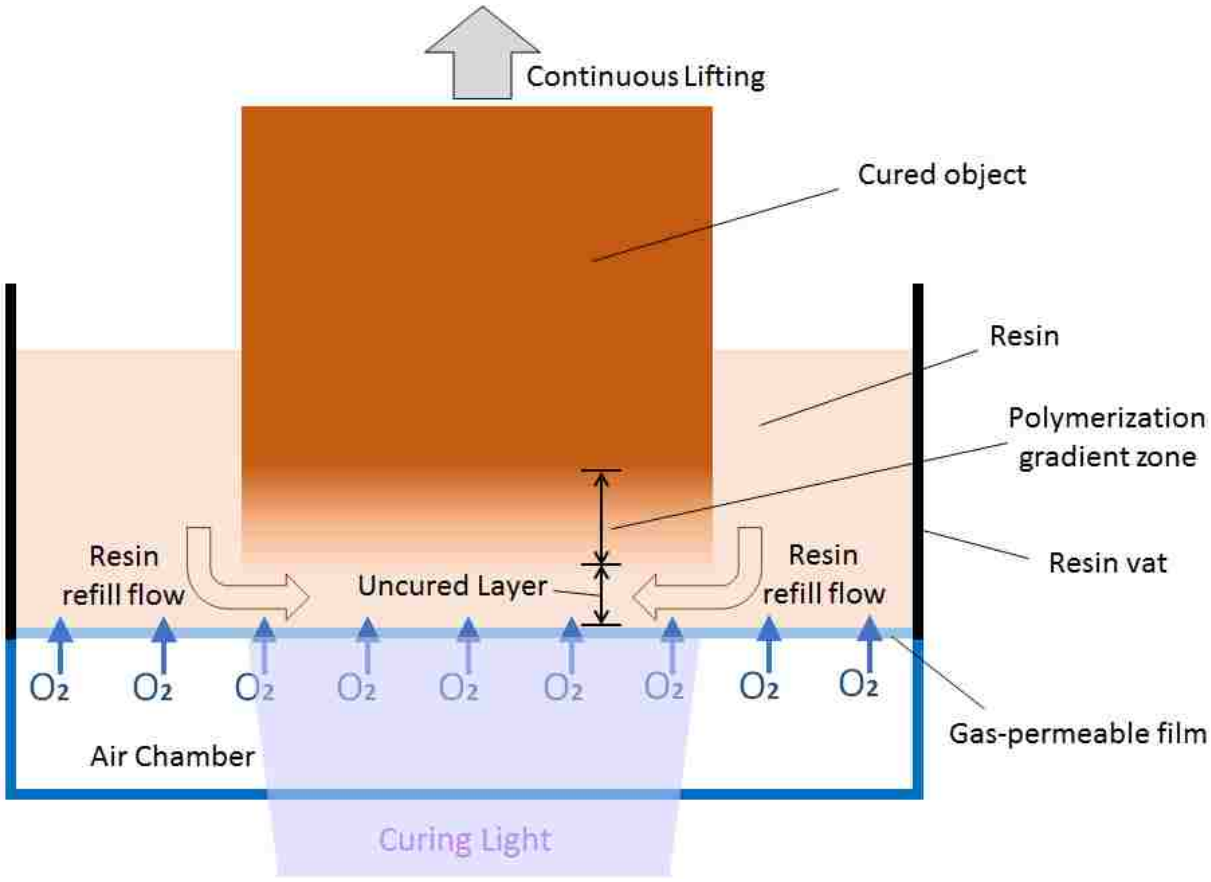

Figure 6-2 Schematic of the formation of the polymerization gradient and inhibited layer.

6.2.2 Continuous additive manufacturing based on oxygen inhibition effect

Most SLA based 3D printing methods requires a platform relocating process after printing each layer. All the relocating processes have a general purpose, which is to create a space that are filled with fresh resin. This fresh liquid layer is required every time before the printing of a new layer. In “bottom-up” (inverted) SLA 3D printing, the newly printed layer can adhere to resin vat. In this case, platform relocating processes are also be applied to help separating the cured layer and resin vat. In some cases, during the platform relocating process, vacuum force is generated between the printed layer and resin vat. To

solve this, the printed object needs to be separated from the vat with a distance far enough to eliminate the vacuum force, and then moves back with a pre-defined speed to create a uniform space for next layer. The relocating process in "bottom-up" SLA 3D printing affects the printing resolution in Z direction and significantly reduces the printing speed. Therefore, oxygen is introduced in this research to create an uncured layer that helps to eliminate the relocating process and achieve continuous fabrication of 3D objects.

To utilize the oxygen inhibition effect in "bottom-up" SLA 3D printing, a silicon based gas-permeable film serves as the substrate that holds the liquid resin and allows the oxygen on the other side to penetrate through. Figure 6-2 shows the diagram of the principles. Because of the concentration difference from two sides of the gas-permeable film, the oxygen in the air chamber can penetrate through the film and diffused into the resin, forming a decreasing oxygen concentration gradient. As the height increases, the concentration of oxygen decreases. Under the exposure of UV light, a thin layer of uncured resin can be remained above the film. Polymerization gradually happens from a height where the oxygen concentration is lower than a threshold that oxygen cannot suppress the majority of the radicals. Right above the threshold plane, the number of active radicals is not sufficient to fully cure the resin since oxygen are still affecting the polymerization. Therefore, a polymerization gradient zone is formed. As the height increases, the degree of polymerization increases, and eventually closes to fully cured. In comparison with fully cured resin, partially cured resin has potential to form stronger internal bonding with the following polymerized resin, since there will be more unreacted functional groups participate in the following polymerization. While The regular DLP/SLA 3D printing approaches use fully cured layer by layer approach, which has weaker bonding between

layers and inconsistent mechanical properties in printed objects. Unlike the typical "bottom-up" SLA 3D printing, there is no adhesion between the polymerized the object and the vat bottom due to the isolation of the uncured layer. Therefore, the platform can carry the curing object and continuously move up. Along with the continuous lifting of the platform, fresh resin enters the inhibited area from nearby regions, providing constant refill of the material for the following printing process.

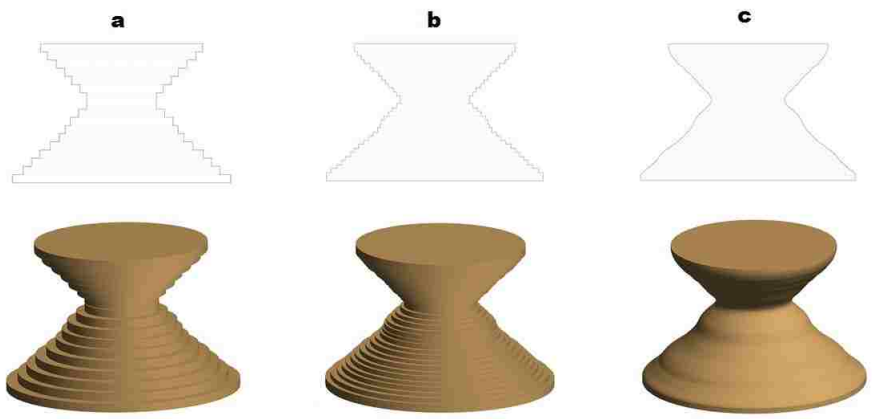

Figure 6-3 Comparison of printing qualities based on different sliced thickness. (a)100μm sliced thickness; (b)50μm sliced thickness; (c)1μm sliced thickness. (Top parts: cross-sections in vertical plane; Bottom part: predicted view of printed models)

In DLP based 3D printing processes, the first step is to slice a 3D model into layer-by-layer images. The number of images created depends on the layer thickness selected. The thinner the layer thickness, the more layers as well as images will be used to expose for the 3D printing. As shown in Figure 6-3 by using smaller layer thickness, higher details of 3D objects can be fabricated. In regular DLP 3D printing methods, the smallest layer thickness is limited by the Z linear system resolution and minimum thickness that can be cured under UV exposure. In the continuous 3D printing method developed from this research, there can be no layers generated by the mechanism since objects are drawn out of the liquid resin continuously. One the other hand, generating sliced layer-by-layer

images are still necessary since 3D models need to be transferred into 2D exposure. Sliced images will be non-stop exposed, forming an animation during the printing process. Theoretically, this continuous printing allows the sliced layer thickness to be extremely thin. Based on the capability of the software we developed, the sliced layer thickness can be as thin as 1μm.

6.2.3 Development of the continuous 3D printer

The gas-permeable membrane applied in this technology is a silicone based film that is highly elastic, and has constant mechanical and electrical properties over long period of use. The film is resin and water repellent, but selectively permeable to gases. Based on the setup in our printing method, the film has an oxygen permeability greater than 300 barrers. To ensure the flatness, the film needs to be highly stretched. The typical uniaxial stretching can cause a mixed state of compressive, shear and tensile strain. In this case, nonuniform tensile strain distribution can be generated in the membrane, which has greater potentials to result in membrane breakage. Stretch-induced mechanical wrinkling behaviors can also be observed. In a uniaxial stretching process with both ends clamped, remarkable wrinkles that are perpendicular to the stretching direction can be observed and the amplitudes of the wrinkle decay toward free edges[129]. Therefore, a method that can be used for equiaxial stretching is developed. This approach is used to strain a circular membrane radially. As Figure 6-4(a) shows, the film is designed in a circular shape with radial cuts to eliminate tangential forces between the clamped positions. Holes need to be cut at the ends of the radial cuts to reduce the risk of breakage. The number of holes is 16 in our research experiments. Figure 6-4(b) shows the schematic of the stretching mechanism. 16 clamps hold the film edges between cuts. A mechanism stretches the 16 clamps according to directions of the corresponding arrows. Figure 6-4(c) shows the finite

element (FEA) analysis of the film deformation under stretching. The FEA result predicts that the middle region has uniform deformation, which is beneficial to be assembled in the vat system. Constant strain and stress around the edge of the membrane will generate an equiaxial state of strain and stress in the membrane.

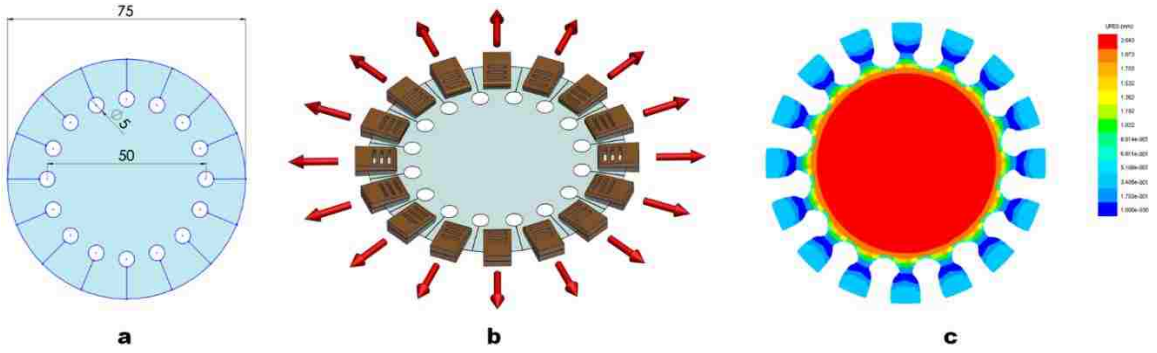

Figure 6-4 (a)Outline and dimension of the gap-permeable film before stretching; (b)The schematic of the equiaxial stretching mechanism; (c)Finite element analysis of the film deformation under the designed stretching mechanism.

As shown in Figure 6-5(a), to better match the shape of the tensioned film, the resin vat was designed in a circular shape, including a resin reservoir on the top, and an air chamber in the bottom. The top part and the bottom part are isolated by the tensioned gas-permeable film, which is also clamped by the structures to maintain the tension state. During the printing process, the curing happens right above the tensioned film. The air chamber underneath provides a close-loop control of the film status, including maintaining flatness and being concave. A pressure sensor inside the air chamber returns feedback of the pressure status, indicating the shape of the film. The air chamber has an inlet and an outlet, providing controls of the pressure inside the air chamber. A miniature vacuum pump can selectively add pressure or apply vacuum in the chamber. The bottom of the air chamber is an optical clear glass, which allows the penetration of exposure lights. Figure

6-5(b) shows the prototype of the 3D printer. The build platform was also designed in a circular shape to match the resin vat. All the rest of the hardware are placed inside the main box.

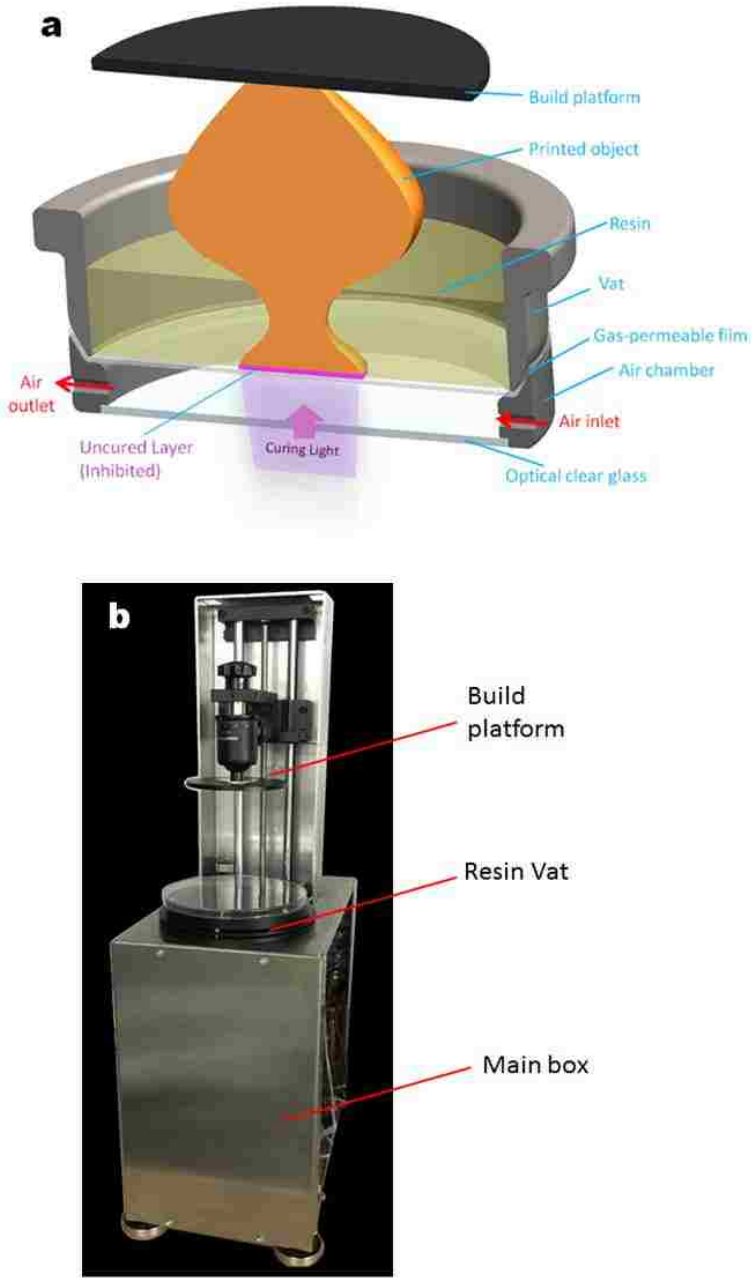

Figure 6-5 (a)A simplified schematic of the vat and air chamber system; (b)A prototype of the continuous 3D printer.

The pressure controlled air chamber is a unique system that overcomes some difficulties in current "bottom-up" SLA printing. The first problem is the deformation of the vat substrate. PDMS is generally used as the anti-adhesion material and is coated on the bottom of the resin vat. Since PDMS is elastic, it is easy to deform under external force or pressure. For example, when the build platform is lowered down to print the first layer, a pre-determined uniform layer thickness between the build platform and the PDMS substrate is expected. However, since the build platform has a large surface area, the volume of resin that is trapped between the build platform and the PDMS can be more than the volume that fits the first layer. Therefore, the PDMS will deform and turn into concave shape because of the pressure generated from the resin. This situation also happens when the previous printed layer has a large surface area. In our printing method, this problem can be solved by apply positive pressure in the air chamber, balancing the pressure generated on top of the film and maintaining a flat status of the membrane. Another key problem for most continuous 3D printing methods is the limitation of printing objects with large cross-sections. Even though a few continuous printing techniques are able to generate an uncured layer to achieve nonstop printing, printing objects with large and solid cross-section can hardly be achieved. As mentioned in the previous paragraph, this is caused by the vacuum force is generated between the printing object and the gas-permeable film when the platform is moving up. In our approach, a series of printing algorithms are developed according to the size of the surface area. When printing objects with small cross-sections, continuous mode with high speed printing is applied since neither adhesion force nor vacuum force exists due to the oxygen inhibited layer. When the cross-section becomes larger, continuous mode with reduce printing speed (build platform lifting speed) is applied

to eliminated the vacuum force effect. When the printing comes to the large and solid cross-section that simply reducing the printing speed cannot eliminate the vacuum force, the printer will start printing layer-by-layer, which is called sequential mode. Between the printing of two layers, negative pressure is applied in the chamber to eliminate the vacuum force. The separation process takes less than 2 seconds. No extra displacement of the build platform is required.

During an entire printing process, the printer switches over to the optimal modes according to the cross-section. The example in Figure *6-6* shows how the printing modes are selected during the printing process. To start printing, the build platform moves down to the initial position, which is one layer above the gas-permeable film. The film will concave down due to the pressure created by the resin trapped in between the film and the platform. Next, positive pressure is applied to level the film and maintain the flatness (Figure 6-6(ii)). Then UV light is exposed to the resin and the build platform continuously move up. In this stage, the pressure in the air chamber gradually decreases until reaches a balanced status (Figure 6-6(iii)). If the cross-sections are always small, the printing speed will remain constant. On the other hand, in many situations, the size of cross-sections varies, and the printing mode needs to be changed accordingly. As the cross-sections become larger (Figure 6-6(iv)), the lifting speed of the platform will be reduced to provide enough time for the resin to refill the inhibited layer. However, when the cross-section of the target object is too large that the vacuum force will suck and deform the film along with the lifting of the build platform. In this situation, simply reducing the speed cannot solve the problem. Therefore, the printer will switch over to sequential mode. As shown in Figure *6-6*(v), the sequential mode is a step-by-step printing process generating negative pressure in the

chamber to separate the film and the printed object. Once software returns large cross-section warning or the sensor gives film deforming alert, the exposure light will be turn off, the platform will move up with a pre-determined layer thickness, and negative pressure is applied in the air chamber. After the separation of the film and the printed object, pressure will be added to the air chamber to level the film. Such processes repeat until the cross-section size is good for continuous printing again.

In this continuous printing technique, the oxygen inhibited layer thickness is mainly related with the oxygen concentration, diffusion rate of oxygen into the resin, photoinitiator concentration, exposure light intensity, exposure time. The diffusion rate of oxygen into the resin is also related to the thickness and permeability of the film. Therefore, based on the certain oxygen concentration in the air chamber and thickness of the gas-permeable film, the inhibited layer thickness (IL) can be expressed as function of UV dose d, which is the product of exposure time t and incident light intensity I_0. Thus, d = t I_0. Also, the uncured layer thickness can be tuned by choosing the functionality or the main chain of photocurable materials. Other impacting factors can be regarded as constant once being set. Therefore, the uncured layer thickness can be represented as:

$$\text{IL thickness} = C d^{-\gamma} \tag{16}$$

where C is the coefficient of proportionality for a certain material, which depends on the monomer reactivity, the oxygen solubility and diffusivity into the liquid resin. The IL thickness can become thicker by either decreasing the monomer reactivity or increasing the oxygen permeability, which can be tuned by reducing the thickness of the gas-permeable film or increasing the oxygen concentration inside the air chamber. By applying

90% oxygen concentration with a film thickness of 100 μm, a maximum inhibited layer thickness of 80 μm can be achieved in the resin we use.

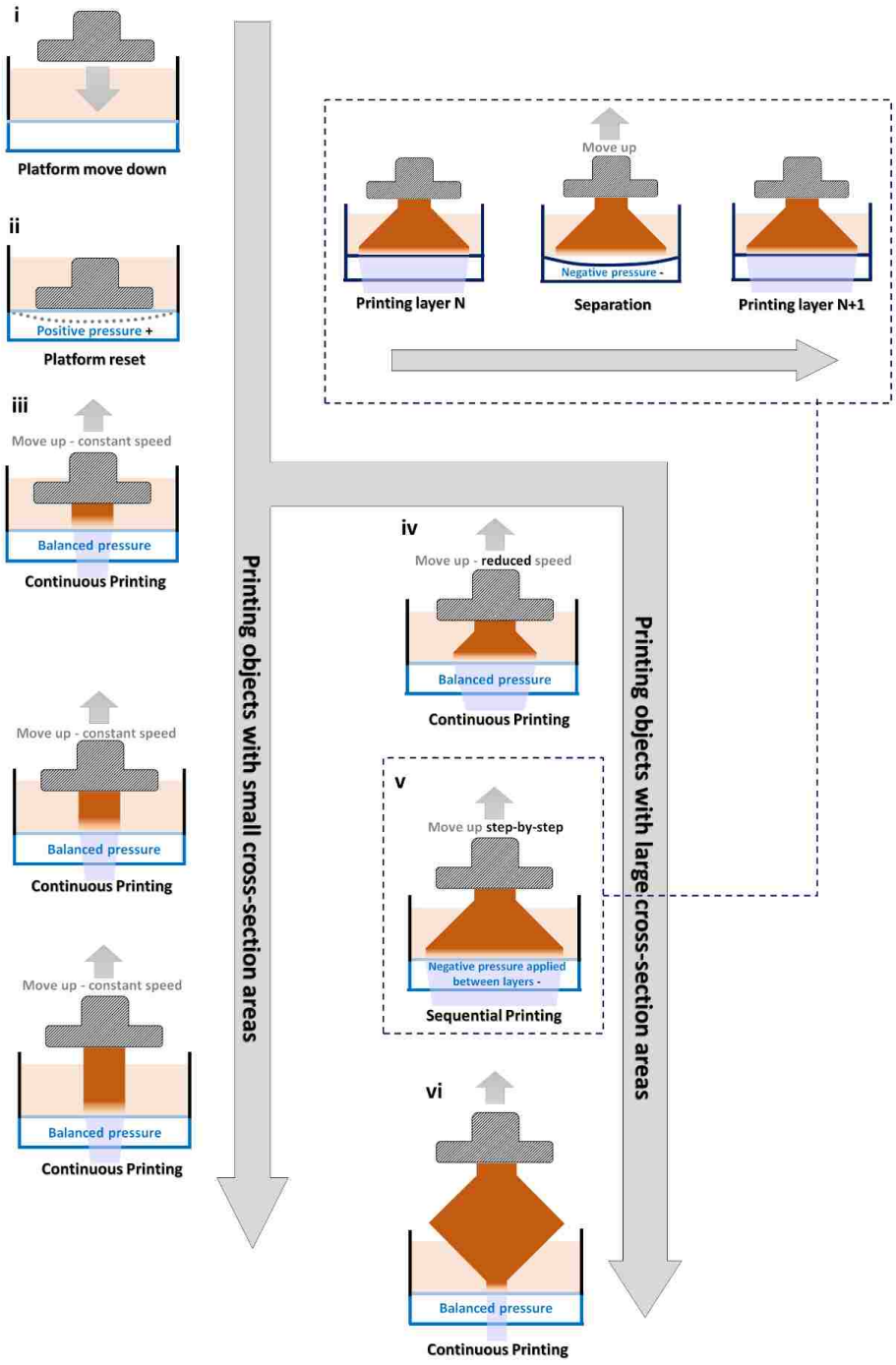

Figure 6-6 A diagram of printing process and printing modes.

6.3 Results and Analysis

Using this continuous 3D printing method, printed parts with ultra-smooth surface can be generated. Figure *6-7* shows comparisons between parts 3D printed by different approaches. Figure *6-7*(a) shows a microscope image of an object printed by regular layer-by-layer DLP-based 3D printer. Figure *6-7*(b) is a microscope image of an object printed by our continuous printing technique. Compared with (a), (b) in Figure *6-7* shows a noticeable difference regarding the surface finish, even though both samples are printed with 25μm sliced layer thickness. Figure *6-7*(c-e) show the microscope image of objects printed by regular DLP-based printing method, our continuous printing method under sequential mode, and our continuous printing method under continuous mode, respectively. Continuous printing method under continuous mode clearly shows the best surface finish. On the other hand, even the sequential mode (Figure *6-7*(d)) shows obviously better finish compared with the regular printing method (Figure *6-7*(e)). On explanation for this result is the removal of the build platform relocating process (platform moves up and down). The build platform relocating can create slightly displacement of the printed object in XY plane, especially for thin and delicate parts, and thus the layer-by-layer lines are more obvious on the surface. Figure *6-7*(f-g) show 3D printed porous balls printed by regular DLP printer and our continuous printer. The result printed by our continuous printing technique shows a better surface with smooth finish. Therefore, through the directly comparisons, this continuous 3D printing technique shows great advantages in surface quality.

Using this continuous printing method, Figure 6-8 shows a series of 3D printed results with unconventional structures. In Figure 6-8(a), a 3D meshed structure with diamond cell are printed. The measured diameter of the meshed wire is 50μm. Figure

6-8(b-c) show a 3D printed rose with hollow inner structure and a 3D printed kitten with solid inner structure. Both the rose and the kitten shows a shining finish, indicating a good surface quality. Figure 6-8(d) shows a 3D printed Reims Cathedral model with delicate details. To characterize the speed of this continuous printing technique, a typical 3D printing model, Eiffel Tower, with 106mm tall was printed in 18 mins. Based on the resin used in this project, the max printing speed in continuous mode is 12mm/min, which is over 20 times faster than the regular SLA 3D printers. (The speed is calculated regarding the height of the model)

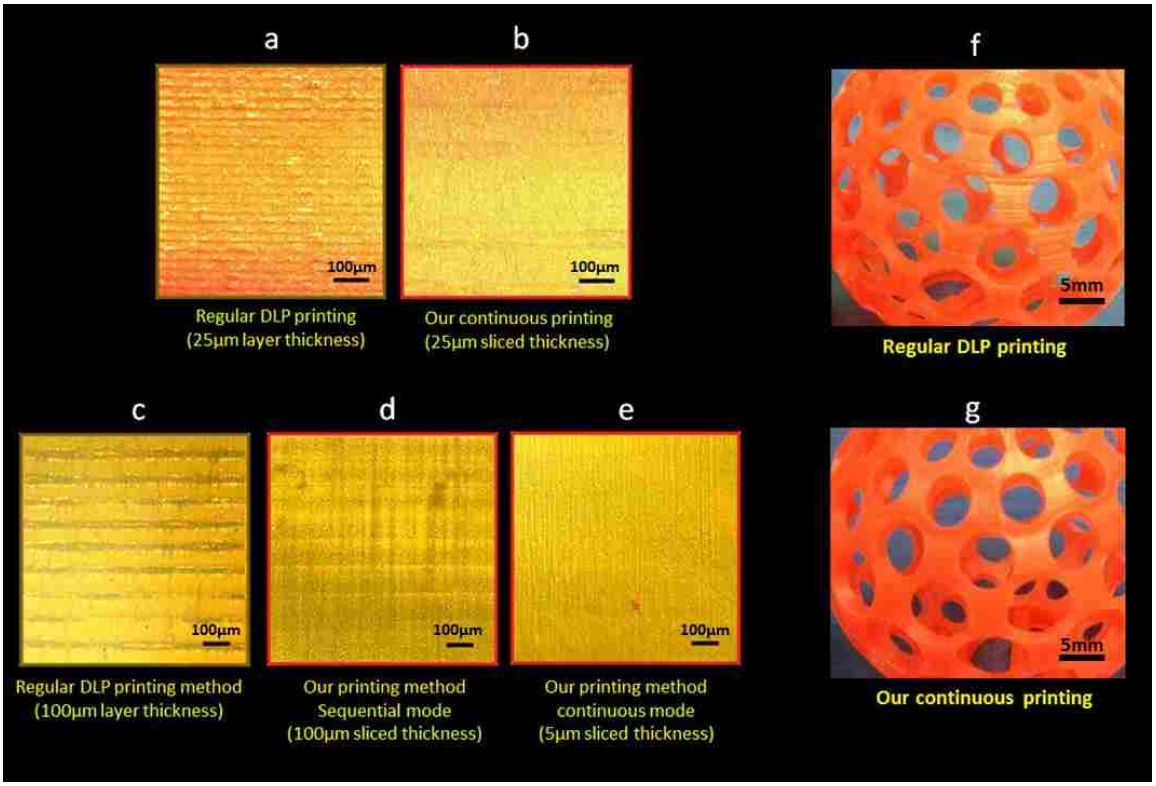

Figure 6-7 Comparisons between parts 3D printed by different approaches. (a-e)The microscope image of (a)an object printed by regular DLP-based 3D printer (25μm layer thickness), (b)an object printed by our continuous 3D printer (25μm sliced thickness), (c)an object printed by regular DLP-based 3D printer (100μm layer thickness), (d)an object printed by our continuous 3D printer under sequential mode (100μm sliced thickness), and (e)an object printed by our continuous 3D printer under continuous mode (5μm sliced thickness); (f-g)3D printed porous balls printed by (f)regular DLP-based 3D printer (50μm layer thickness), and (g)our continuous printer (5μm sliced thickness).

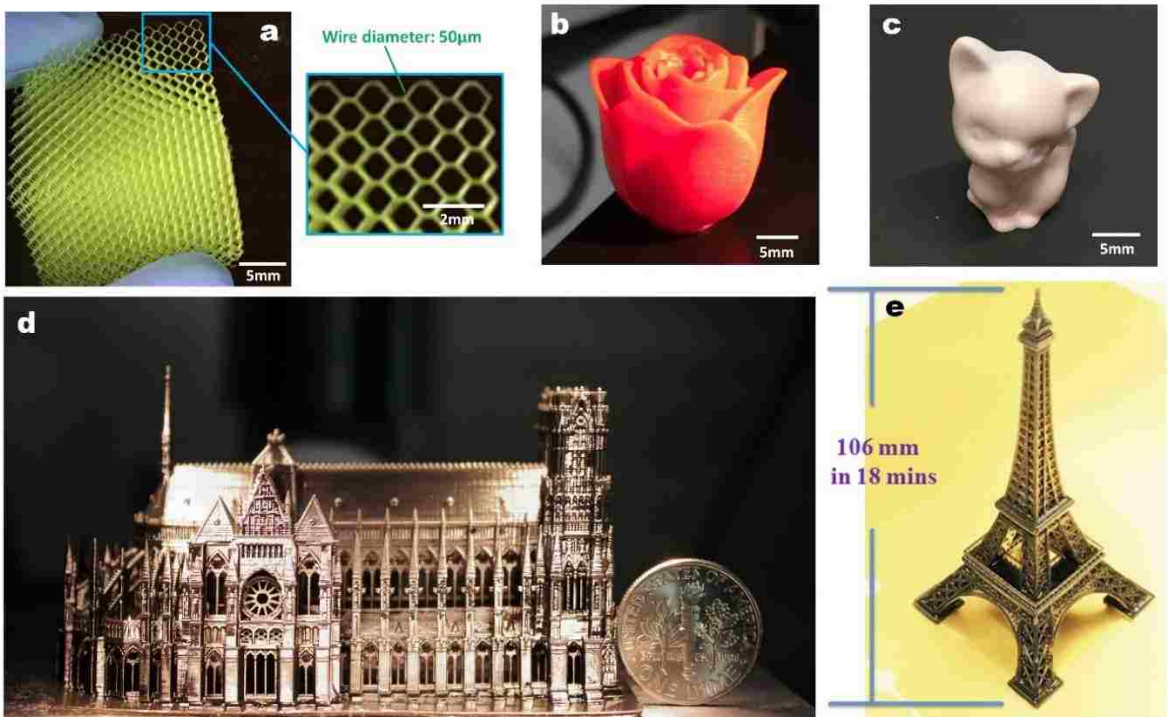

Figure 6-8 A series of 3D printed results with unconventional structures (a)A meshed structure with diamond cell; (b)A rose with hollow inner structure; (c)A kitten with solid inner structure; (d)A Reims Cathedral model; (e)An Eiffel Tower (106mm tall) printed in 18mins.

As shown in Table 6-1, the continuous 3D printing method developed in this research shows its advantage in printing speed when comparing with most mainstream players in the market. Carbon's CLIP technology also has the capability to reach the printing speed of the same level. However, due to the expense of AF2400 film and software algorithms in Carbon's technology, the price in unaffordable for many users in both consumer and industrial market. Meanwhile, our invention utilized a gas-permeable film and air chamber control methods, which has a much cheaper cost. Furthermore, this continuous printing methods offers the sequential mode, which has can produce parts with large cross-sections that is hard to be produced by other layer-less printing methods.

	Our Technique	Carbon M1	EnvisionTech cDLM	B9 Creator 550	MoonRay S	MiiCraft 100
Peak Speed	600 mm/hr	500 mm/hr	70 mm/hr	100 mm/hr	25 mm/hr	30mm/hr
Minimum Layer Thickness	Layer-less	Layer-less	1 μm	Up to 10 μm	20 μm	30 μm
Minimum Feature Size	40μm	75 μm	30μm	50μm	70μm	53μm
Technology	Continuous 3D Fabrication	CLIP	cDLM	DLP	DLP	DLP
Market Price	Less than $10,000 (Estimated)	$120,000 three-year leasing	$29,900	$9,955	$5,999	$11,500

Table 6-1 Comparison of mainstream DLP 3D printers' specifications.

6.4 Conclusions

Through this research, a continuous 3D printing technology is developed. This technique enables the ultra-high-speed fabrication of 3D object with improved surface qualities. Parts with complex geometries and intricate details can be generated in very short time, which can significantly reduce the lead time of urgent need or customized products. Through the closed loop control of film and air chamber systems, printing processes are dynamically changed. 3D objects with both solid inner structures and porous structures can be precisely fabricated. This technology is compatible with a variety of photocurable materials, including prototyping, engineering, biological, castable, ceramic, and even metal

materials. Therefore, it has the great potential to be applied in varies industries, such as jewelry, medical, dental, and research development.

Chapter 7 : Summary and Outlook

This dissertation presents a series of innovative fabrication technologies to advance the microfabrication field and its applicable areas. These techniques all utilized the digital-light lithography to generate unique microstructures that can be hardly fabricated via prior arts. Due to the difficulties in fabrication, typically including the cost, geometric limitations, customizability and efficiency, these microstructures are not commonly seen in published research or industrial works. We call them unconventional structures in this dissertation. On the other hand, these unconventional structures are important, as many opportunities in technological innovations depend on the ability to fabricate novel structures and high-performance devices that request effective and precise fabrication technologies. Thus, methods have been innovated and developed through our research, providing solutions for effectively generating geometries that are demanded to conduct future research projects. Trace to its source, this series of research began with the original motivation of fabricating lab-on-a-chip devices with micro-patterned structures for biomedical research. Through the first success, we realized the high efficiency, customizability, and extensibility of the digital lithography. It can bring more potentials to not only microfluidic applications, but also various of fields that require precise manufacturing. Along with our progress in developing digital-lithographic fabrication in microfluidic applications, we also extended the approach to develop novel 3D printing techniques, which can bring more opportunities in both scientific and industrial fields.

The first development was a grayscale direct-image lithography method, which was driven by the need of fabricating wavy-patterned microfluidic devices for capturing CTCs.

Although direct-image lithography has been used in prior arts, they barely considered and utilized this effect of optical distortion to fabricate micro-structures. Due to optical distortion, the non-uniform energy distribution always exists and generates errors (from a few microns to hundreds of microns) on the fabricated micro-patterns. Instead of considering the optical distortion as trivial matters or errors, we utilized it to model inaccuracies inherent in the polymerization process. The combination of grayscale and digital lithography allowed the generation of highly customized patterns with complex profiles. Most importantly, we wanted to consistently predict the results. Thus, the established computation models of grayscale polymerization process and software for image generation were designed to predict and guide fabrication results. Since this method does not require a clean room or expensive lithography equipment, it brings not only high efficiency but great convenience and low cost to the fabrication of lab-on-a-chip devices with complex patterns. In this first lithography project, we managed to develop a novel approach to fabricate functional patterns with diverse geometries in a precise and controllable manner. Furthermore, the establishment of the mathematical model can guide the fabrication of more complex 3D structures in the future - not just limited to wavy patterns.

Build upon the first development, and further driven by the need of generating circular microfluidic channels for particle binding study, we developed the second microfabrication technique, a dual-projection lithography method, to fabricate circular microfluidic channels. Since the previous grayscale lithography systems can generate controllable wavy patterns, we utilized two of these systems to expose grayscale images face-to-face and simultaneously polymerize the photocurable materials. An improved

computational model for this dual-projection lithography method was established to predict and guide fabrication results. This method can generate well controlled circular and elliptical channels, along with complex fluidic networks. The complex networks of channels that generated by this method, such as junctions, bifurcations, hierarchical structures, and channels with gradually changed diameters, can be hardly fabricated by other technologies. As circular microfluidic channels with complex networks are hard to fabricate, but are in great demand since they are more realistic in mimicking nature systems, this technique can provide great convenience for researchers to improve scientific experimentation for biological and medical applications, especially in nanomedicine and therapeutic studies.

The third technique invented in this series is a combination of several novel methods developed from our research. To further advance the microfluidic field, we wished to generate actuation systems instead of static structures. The more advanced ways are in situ fabrication, remotely controlled actuating, and precise control of the rotation angle. Therefore, in this developed technique, the in situ fabrication was achieved by utilizing the light inhibition effect to selectively curing a floating object and a fixed object at the same time. Compared with prior arts, this in situ process does not require any post processing, assembly, or pre-fabrication. The remote control was achieved by applying magnet field to manipulate the floating structure with embedded magnetic nanoparticles. The precise control of the rotation angle was realized by aligning the embedded magnetic particles with acoustically before curing. All these three features are highly desired and they can hardly be achieved in prior arts. The combination of these three features offers a complete novel technique to in situ fabricate microfluidic actuators with precisely controlled movement,

making it suitable for many potential microfluidic applications, such as micromixers, sorting, and micropumps.

The digital lithography can be further extended to fields other than the microfluidics. SLA technology in additive manufacturing became more popular and has started replacing some of the traditional manufacturing techniques. Aimed at printing both integrated large-scale objects and intricate details, we developed a scanning lithography technique to allow the UV projector to continuously cure resin while scanning over the build area. This approach can be regarded as a combination of both laser based 3D printing and DLP based 3D printing, adopting laser's mobility and DLP's ability to exposure an area at once. The key part of this technique was synchronizing the dynamically exposed images with the scanning of the projector. Due to the resin reflow and surface tension, maintaining the flatness of the resin surface for each layer was also a big challenge in this approach. This 3D printing method can serve as a scalable technology that enables customized build volumes in very large scale. Along with the development of various photocurable materials, this technique can fabricate parts made of polymer, ceramic[130][131], and potentially metal, leading to direct manufacturing of functional parts with desired materials. More projectors can be used to scan together to further improve the printing speed. As this printing technique has advantages in printing speed, resolution and size, it can potentially attract more interests from research and industries.

Since the printing of large-scale object with intricate details can be achieved by our scanning lithography method, we wanted to further improve the printing speed and printing quality. 3D printing is commonly known as a layer-by-layer printing process, which leaves inevitable lines on the surface of printed objects. In SLA based 3D printing, this layer-by-

layer process also significantly slows down the printing, as it is accompanied by platform relocating process that can take up to minutes for each layer. We invented a continuous 3D printing method based on partially inhibited polymerization induced by oxygen. Ultra-high-speed and layer-less finish were realized at the same time. Since the relocating process of the build platform and adhesion force have been eliminated, parts with tiny details made by elastomer materials can be fabricated. Different from other continuous 3D printing technologies, this invention used a close-loop pressure control to provide robust solutions for printing objects with solid inner structures and large cross-sections. Current 3D printing technology and market trends are driving the cost of 3D printers and materials to make them affordable for commercial manufacturing. As the cost of this technology is much cheaper compared with other mainstream players, it can potentially be a very competitive product for any researchers or industries who are interested in an affordable 3D printer with outstanding performance in speed and print quality.

In sum, this dissertation has presented five fabrication technologies based on digital lithography for various applications. Each of them has its uniqueness in the corresponding applications. The results showed competitive advantages in some ways over the existing methods. Since microfabrication techniques for lab-on-a-chip devices and 3D printing are of great interests and leading the trend, the research and inventions developed here are expected to have advancements in the related fields. However, as most technologies presented in this dissertation are still in laboratory stage, converting them into successful commercial products are also challenging processes. On the other hand, as the digital microfabrication is a rapid growing area, any breakthrough invention can potentially open a new trend in manufacturing, just like the role that 3D printing is currently playing.

References

[1] B. Postier, R. DiDonato, K. P. Nevin, A. Liu, B. Frank, D. Lovley, and B. a. Methe, “Benefits of in-situ synthesized microarrays for analysis of gene expression in understudied microorganisms,” *J. Microbiol. Methods*, vol. 74, no. 1, pp. 26–32, 2008.

[2] V. Faustino, S. O. Catarino, R. Lima, and G. Minas, “Biomedical microfluidic devices by using low-cost fabrication techniques: A review,” *J. Biomech.*, vol. 49, pp. 2280–2292, 2016.

[3] P. K. Dey, B. Pramanick, a. Ravi Shankar, P. Ganguly, and S. Das, “Microstructuring of su-8 resist for mems and bio-applications,” *Int. J. Smart Sens. Intell. Syst.*, vol. 3, no. 1, pp. 118–129, 2010.

[4] G. a Urban, “Micro- and nanobiosensors—state of the art and trends,” *Meas. Sci. Technol.*, vol. 20, no. 1, p. 12001, 2008.

[5] T. Nisisako and T. Torii, “Microfluidic large-scale integration on a chip for mass production of monodisperse droplets and particles,” *Lab Chip*, vol. 8, no. 2, pp. 287–293, 2008.

[6] I. E. Araci and P. Brisk, “Recent developments in microfluidic large scale integration,” *Curr. Opin. Biotechnol.*, vol. 25, pp. 60–68, 2014.

[7] N. S. G. K. Devaraju and M. a Unger, “Pressure driven digital logic in PDMS based microfluidic devices fabricated by multilayer soft lithography.,” *Lab Chip*, vol. 12, no. 22, pp. 4809–15, 2012.

[8] M. S. Thomas, B. Millare, J. M. Clift, D. Bao, C. Hong, and V. I. Vullev, “Print-and-peel fabrication for microfluidics: What’s in it for biomedical applications?,” *Ann. Biomed. Eng.*, vol. 38, no. 1, pp. 21–32, 2010.

[9] V. I. Vullev, J. Wan, V. Heinrich, P. Landsman, P. E. Bower, B. Xia, B. Millare, and G. Jones II, “Nonlithographic fabrication of microfluidic devices,” *J. Am. Chem. Soc.*, vol. 128, no. 50, pp. 16062–16072, 2006.

[10] V. Pinto, P. Sousa, V. Cardoso, and G. Minas, “Optimized SU-8 Processing for Low-Cost Microstructures Fabrication without Cleanroom Facilities,” *Micromachines*, vol. 5, no. 3, pp. 738–755, 2014.

[11] R. Lopes, R. O. Rodrigues, D. Pinho, V. Garcia, H. Schütte, R. Lima, and S. Gassmann, “Low cost microfluidic device for partial cell separation : micromilling approach,” *IEEE Int. Conf. Ind. Technol. 2015*, pp. 3347–3350, 2015.

[12] E. Sollier, M. Cubizolles, Y. Fouillet, and J. L. Achard, “Fast and continuous plasma extraction from whole human blood based on expanding cell-free layer devices,” *Biomed. Microdevices*, vol. 12, no. 3, pp. 485–497, 2010.

[13] L. Wang, R. Kodzius, X. Yi, S. Li, Y. S. Hui, and W. Wen, “Prototyping chips in minutes:

Direct Laser Plotting (DLP) of functional microfluidic structures," *Sensors Actuators, B Chem.*, vol. 168, pp. 214–222, 2012.

[14] B. Ziaie, A. Baldi, M. Lei, Y. Gu, and R. a. Siegel, "Hard and soft micromachining for BioMEMS: Review of techniques and examples of applications in microfluidics and drug delivery," *Adv. Drug Deliv. Rev.*, vol. 56, no. 2, pp. 145–172, 2004.

[15] G. M. Whitesides, E. Ostuni, X. Jiang, and D. E. Ingber, "S Oft L Ithography in B Iology," *Annu. Rev. Biomed. Eng.*, vol. 3, pp. 335–73, 2001.

[16] Y. Xia and G. M. Whitesides, "Soft Lithography," *Annu. Rev. Mater. Sci.*, no. 28, pp. 153–84, 1998.

[17] B.-J. de Gans, P. C. Duineveld, and U. S. Schubert, "Inkjet Printing of Polymers: State of the Art and Future Developments," *Adv. Mater.*, vol. 16, no. 3, pp. 203–213, 2004.

[18] M. Singh, H. M. Haverinen, P. Dhagat, and G. E. Jabbour, "Inkjet printing-process and its applications," *Adv. Mater.*, vol. 22, no. 6, pp. 673–685, 2010.

[19] Y. M. Huang, S. Kuriyama, and C. P. Jiang, "Fundamental study and theoretical analysis in a constrained-surface stereolithography system," *Int. J. Adv. Manuf. Technol.*, vol. 24, no. 5–6, pp. 361–369, 2004.

[20] F. P. W. Melchels, J. Feijen, and D. W. Grijpma, "A review on stereolithography and its applications in biomedical engineering," *Biomaterials*, vol. 31, no. 24, pp. 6121–6130, 2010.

[21] A. K. Au, W. Lee, and A. Folch, "Mail-order microfluidics: evaluation of stereolithography for the production of microfluidic devices," *Lab Chip*, vol. 14, no. 7, pp. 1294–1301, 2014.

[22] A. I. Shallan, P. Smejkal, M. Corban, R. M. Guijt, and M. C. Breadmore, "Cost-effective three-dimensional printing of visibly transparent microchips within minutes," *Anal. Chem.*, vol. 86, no. 6, pp. 3124–3130, 2014.

[23] S. Takenaga, B. Schneider, E. Erbay, M. Biselli, T. Schnitzler, M. J. Schöning, and T. Wagner, "Fabrication of biocompatible lab-on-chip devices for biomedical applications by means of a 3D-printing process," *Phys. Status Solidi Appl. Mater. Sci.*, vol. 212, no. 6, pp. 1347–1352, 2015.

[24] J.-F. Xing, M.-L. Zheng, and X.-M. Duan, "Two-photon polymerization microfabrication of hydrogels: an advanced 3D printing technology for tissue engineering and drug delivery," *Chem. Soc. Rev.*, vol. 44, no. 15, pp. 5031–5039, 2015.

[25] M. Farsari and B. N. Chichkov, "Materials processing: Two-photon fabrication," *Nat. Photonics*, vol. 3, no. 8, pp. 450–452, 2009.

[26] H. Z. Cao, M. L. Zheng, X. Z. Dong, F. Jin, Z. S. Zhao, and X. M. Duan, "Two-photon nanolithography of positive photoresist thin film with ultrafast laser direct writing," *Appl. Phys. Lett.*, vol. 102, no. 20, 2013.

[27] S. Kawata, H.-B. Sun, T. Tanaka, and K. Takada, "Finer features for functional

microdevices," *Nature*, vol. 412, no. 6848, pp. 697–698, 2001.

[28] M. Stoneman, M. Fox, C. Zeng, and V. Raicu, "Real-time monitoring of two-photon photopolymerization for use in fabrication of microfluidic devices," *Lab Chip*, vol. 9, no. 6, pp. 819–827, 2009.

[29] G. Kumi, C. O. Yanez, K. D. Belfield, and J. T. Fourkas, "High-speed multiphoton absorption polymerization: fabrication of microfluidic channels with arbitrary cross-sections and high aspect ratios," *Lab Chip*, vol. 10, no. 8, p. 1057, 2010.

[30] A. K. Geim, S. V Dubonos, I. V Grigorieva, K. S. Novoselov, A. A. Zhukov, and S. Y. Shapoval, "Microfabricated adhesive mimicking gecko foot-hair.," *Nat. Mater.*, vol. 2, no. 7, pp. 461–3, Jul. 2003.

[31] A. Saez, A. Buguin, P. Silberzan, and B. Ladoux, "Is the mechanical activity of epithelial cells controlled by deformations or forces?," *Biophys. J.*, vol. 89, no. 6, pp. L52–L54, 2005.

[32] A. Khademhosseini, J. Yeh, S. Jon, G. Eng, K. Y. Suh, J. a Burdick, and R. Langer, "Molded polyethylene glycol microstructures for capturing cells within microfluidic channels.," *Lab Chip*, vol. 4, no. 5, pp. 425–430, 2004.

[33] J. Hu, C. Hardy, C.-M. Chen, S. Yang, A. S. Voloshin, and Y. Liu, "Enhanced cell adhesion and alignment on micro-wavy patterned surfaces.," *PLoS One*, vol. 9, no. 8, p. e104502, Jan. 2014.

[34] J. Genzer and J. Groenewold, "Soft matter with hard skin: From skin wrinkles to templating and material characterization," *Soft Matter*, vol. 2, no. 4, p. 310, 2006.

[35] C. Jin, A. Jagota, and C.-Y. Hui, "Structure and Energetics of Dislocations at Micro-Structured Complementary Interfaces Govern Adhesion," *Adv. Funct. Mater.*, vol. 23, no. 27, pp. 3453–3462, Jul. 2013.

[36] Y. Rahmawan, C.-M. Chen, and S. Yang, "Recent advances in wrinkle-based dry adhesion.," *Soft Matter*, vol. 10, no. 28, pp. 5028–39, 2014.

[37] P.-C. Lin and S. Yang, "Mechanically switchable wetting on wrinkled elastomers with dual-scale roughness," *Soft Matter*, vol. 5, no. 5, p. 1011, 2009.

[38] N. Bowden, S. Brittain, and A. Evans, "Spontaneous formation of ordered structures in thin films of metals supported on an elastomeric polymer," *Nature*, vol. 393, no. May, pp. 146–149, 1998.

[39] D. Chandra and A. J. Crosby, "Self-Wrinkling of UV-Cured Polymer Films," *Adv. Mater.*, vol. 23, no. 30, pp. 3441–3445, 2011.

[40] A. Rammohan, P. K. Dwivedi, R. Martinez-Duarte, H. Katepalli, M. J. Madou, and A. Sharma, "One-step maskless grayscale lithography for the fabrication of 3-dimensional structures in SU-8," *Sensors Actuators, B Chem.*, vol. 153, no. 1, pp. 125–134, 2011.

[41] C. M. Waits, B. Morgan, M. Kastantin, and R. Ghodssi, "Microfabrication of 3D silicon MEMS structures using gray-scale lithography and deep reactive ion etching," *Sensors*

Actuators, A Phys., vol. 119, no. 1, pp. 245–253, 2005.

[42] C. F. Guo, S. Cao, P. Jiang, Y. Fang, J. Zhang, Y. Fan, Y. Wang, W. Xu, Z. Zhao, and Q. Liu, "Grayscale photomask fabricated by laser direct writing in metallic nano-films.," *Opt. Express*, vol. 17, no. 22, pp. 19981–19987, 2009.

[43] M. H. Wu, C. Park, and G. M. Whitesides, "Fabrication of arrays of microlenses with controlled profiles using gray-scale microlens projection photolithography," *Langmuir*, vol. 18, no. 24, pp. 9312–9318, 2002.

[44] C. Zhou and Y. Chen, "Additive manufacturing based on optimized mask video projection for improved accuracy and resolution," *J. Manuf. Process.*, vol. 14, no. 2, pp. 107–118, 2012.

[45] S.-H. Song, K. Kim, S.-E. Choi, S. Han, H.-S. Lee, S. Kwon, and W. Park, "Fine-tuned grayscale optofluidic maskless lithography for three-dimensional freeform shape microstructure fabrication.," *Opt. Lett.*, vol. 39, no. 17, pp. 5162–5, Sep. 2014.

[46] Y. Jung, H. Lee, T.-J. Park, S. Kim, and S. Kwon, "Programmable gradational micropatterning of functional materials using maskless lithography controlling absorption," *Sci. Rep.*, vol. 5, no. October, p. 15629, 2015.

[47] S. Han, H. J. Bae, J. Kim, S. Shin, S. E. Choi, S. H. Lee, S. Kwon, and W. Park, "Lithographically encoded polymer microtaggant using high-capacity and error-correctable QR Code for anti-counterfeiting of drugs," *Adv. Mater.*, vol. 24, no. 44, pp. 5924–5929, 2012.

[48] E. D. Pratt, C. Huang, B. G. Hawkins, J. P. Gleghorn, and B. J. Kirby, "Rare Cell Capture in Microfluidic Devices.," *Chem. Eng. Sci.*, vol. 66, no. 7, pp. 1508–1522, Apr. 2011.

[49] M. Yu, S. Stott, M. Toner, S. Maheswaran, and D. a. Haber, "Circulating tumor cells: Approaches to isolation and characterization," *J. Cell Biol.*, vol. 192, no. 3, pp. 373–382, 2011.

[50] S. Wang, Y. Wan, and Y. Liu, "Effects of nanopillar array diameter and spacing on cancer cell capture and cell behaviors.," *Nanoscale*, vol. 6, no. 21, pp. 12482–9, Nov. 2014.

[51] S. L. Stott, C.-H. C.-H. Hsu, D. I. Tsukrov, M. Yu, D. T. Miyamoto, B. a. Waltman, S. M. Rothenberg, A. M. Shah, M. E. Smas, G. K. Korir, F. P. Floyd, A. J. Gilman, J. B. Lord, D. Winokur, S. Springer, D. Irimia, S. Nagrath, L. V. Sequist, R. J. Lee, K. J. Isselbacher, S. Maheswaran, D. a. Haber, and M. Toner, "Isolation of circulating tumor cells using a," *October*, vol. 107, no. 35, pp. 18392–7, 2010.

[52] P. Xue, K. Ye, J. Gao, Y. Wu, J. Guo, K. M. Hui, and Y. Kang, "Isolation and elution of Hep3B circulating tumor cells using a dual-functional herringbone chip," *Microfluid. Nanofluidics*, vol. 16, no. 3, pp. 605–612, 2013.

[53] K. M. Krone, R. Warias, C. Ritter, A. Li, C. G. Acevedo-Rocha, M. T. Reetz, and D. Belder, "Analysis of Enantioselective Biotransformations Using a Few Hundred Cells on an Integrated Microfluidic Chip," *J. Am. Chem. Soc.*, vol. 138, no. 7, pp. 2102–2105, 2016.

[54] N. Brandenberg and M. P. Lutolf, “In Situ Patterning of Microfluidic Networks in 3D Cell-Laden Hydrogels,” *Adv. Mater.*, pp. 7450–7456, 2016.

[55] D. B. Wolfe, R. S. Conroy, P. Garstecki, B. T. Mayers, M. a Fischbach, K. E. Paul, M. Prentiss, and G. M. Whitesides, “Dynamic control of liquid-core/liquid-cladding optical waveguides.,” *Proc. Natl. Acad. Sci. U. S. A.*, vol. 101, no. 34, pp. 12434–12438, 2004.

[56] S. Wang, Y. Zhou, J. Tan, J. Xu, J. Yang, and Y. Liu, “Computational modeling of magnetic nanoparticle targeting to stent surface under high gradient field,” *Comput. Mech.*, vol. 53, no. 3, pp. 403–412, 2014.

[57] S. Wang, S. Sohrabi, J. Xu, J. Yang, and Y. Liu, “Geometry design of herringbone structures for cancer cell capture in a microfluidic device,” *Microfluid. Nanofluidics*, vol. 20, no. 11, p. 148, 2016.

[58] M. Shin, K. Matsuda, O. Ishii, H. Terai, M. Kaazempur-Mofrad, J. Borenstein, M. Detmar, and J. P. Vacanti, “Endothelialized networks with a vascular geometry in microfabricated poly(dimethyl siloxane),” *Biomed. Microdevices*, vol. 6, no. 4, pp. 269–278, 2004.

[59] S. S. Shevkoplyas, S. C. Gifford, T. Yoshida, and M. W. Bitensky, “Prototype of an in vitro model of the microcirculation,” *Microvasc. Res.*, vol. 65, no. 2, pp. 132–136, 2003.

[60] H. Lu, L. Y. Koo, W. M. Wang, D. a. Lauffenburger, L. G. Griffith, and K. F. Jensen, “Microfluidic shear devices for quantitative analysis of cell adhesion,” *Anal. Chem.*, vol. 76, no. 18, pp. 5257–5264, 2004.

[61] N. W. Bartlett and R. J. Wood, “Comparative analysis of fabrication methods for achieving rounded microchannels in PDMS,” *J. Micromechanics Microengineering*, vol. 26, no. 11, p. 115013, 2016.

[62] G. M. Riha, P. H. Lin, A. B. Lumsden, Q. Yao, and C. Chen, “Roles of hemodynamic forces in vascular cell differentiation,” *Ann. Biomed. Eng.*, vol. 33, no. 6, pp. 772–779, 2005.

[63] S. H. Song, C. K. Lee, T. J. Kim, I. C. Shin, S. C. Jun, and H. Il Jung, “A rapid and simple fabrication method for 3-dimensional circular microfluidic channel using metal wire removal process,” *Microfluid. Nanofluidics*, vol. 9, no. 2–3, pp. 533–540, 2010.

[64] Y. Jia, J. Jiang, X. Ma, Y. Li, H. Huang, K. Cai, S. Cai, and Y. Wu, “PDMS microchannel fabrication technique based on microwire-molding,” *Chinese Sci. Bull.*, vol. 53, no. 24, pp. 3928–3936, 2008.

[65] M. K. S. Verma, A. Majumder, and A. Ghatak, “Embedded template-assisted fabrication of complex microchannels in PDMS and design of a microfluidic adhesive,” *Langmuir*, vol. 22, no. 24, pp. 10291–10295, 2006.

[66] H. Perry, C. Greiner, I. Georgakoudi, M. Cronin-Golomb, and F. G. Omenetto, “Simple fabrication technique for rapid prototyping of seamless cylindrical microchannels in polymer substrates,” *Rev. Sci. Instrum.*, vol. 78, no. 4, pp. 1–4, 2007.

[67] J. Tan, S. Wang, J. Yang, and Y. Liu, “Coupled particulate and continuum model for nanoparticle targeted delivery,” *Comput. Struct.*, vol. 122, pp. 128–134, 2013.

[68] J. Tan, S. Shah, A. Thomas, H. D. Ou-Yang, and Y. Liu, “The influence of size, shape and vessel geometry on nanoparticle distribution,” *Microfluid. Nanofluidics*, vol. 14, no. 1–2, pp. 77–87, 2013.

[69] K. Lee, C. Kim, K. S. Shin, J. W. Lee, B.-K. Ju, T. S. Kim, S.-K. Lee, and J. Y. Kang, “Fabrication of round channels using the surface tension of PDMS and its application to a 3D serpentine mixer,” *J. Micromechanics Microengineering*, vol. 17, pp. 1533–1541, 2007.

[70] L. K. Fiddes, N. Raz, S. Srigunapalan, E. Tumarkan, C. a. Simmons, A. R. Wheeler, and E. Kumacheva, “A circular cross-section PDMS microfluidics system for replication of cardiovascular flow conditions,” *Biomaterials*, vol. 31, no. 13, pp. 3459–3464, 2010.

[71] A. R. Abate, D. Lee, T. Do, C. Holtze, and D. a Weitz, “Glass coating for PDMS microfluidic channels by sol-gel methods.,” *Lab Chip*, vol. 8, no. 4, pp. 516–8, 2008.

[72] M. a. Unger, “Monolithic Microfabricated Valves and Pumps by Multilayer Soft Lithography,” *Science (80-.).*, vol. 288, no. 5463, pp. 113–116, 2000.

[73] G. J. Wang, K. H. Ho, S. H. Hsu, and K. P. Wang, “Microvessel scaffold with circular microchannels by photoresist melting,” *Biomed. Microdevices*, vol. 9, no. 5, pp. 657–663, 2007.

[74] D. S. Zhao, B. Roy, M. T. McCormick, W. G. Kuhr, and S. a Brazill, “Rapid fabrication of a poly(dimethylsiloxane) microfluidic capillary gel electrophoresis system utilizing high precision machining.,” *Lab Chip*, vol. 3, no. 2, pp. 93–99, 2003.

[75] M. E. Wilson, N. Kota, Y. Kim, Y. Wang, D. B. Stolz, P. R. LeDuc, and O. B. Ozdoganlar, “Fabrication of circular microfluidic channels by combining mechanical micromilling and soft lithography.,” *Lab Chip*, vol. 11, no. 8, pp. 1550–1555, 2011.

[76] A. Ahmadi, R. Samanipour, B. Parker, and K. Kim, “Rapid fabrication of circular channel microfluidic flow-focusing devices for hydrogel droplet generation,” *Micro Nano Lett.*, vol. 11, no. 1, pp. 41–45, 2016.

[77] S.-H. Song, K. Kim, S.-E. Choi, S. Han, H. Lee, S. Kwon, and W. Park, “Fine-tuned grayscale optofluidic maskless lithography for three-dimensional freeform shape microstructure fabrication.,” *Opt. Lett.*, vol. 39, no. 17, pp. 5162–5, 2014.

[78] R. He, S. Wang, G. Andrews, W. Shi, and Y. Liu, “Generation of Customizable Micro-wavy Pattern through Grayscale Direct Image Lithography,” *Sci. Rep.*, vol. 6, p. 21621, 2016.

[79] A. Vitale, M. Quaglio, A. Chiodoni, K. Bejtka, M. Cocuzza, C. F. Pirri, and R. Bongiovanni, “Oxygen-Inhibition Lithography for the Fabrication of Multipolymeric Structures,” *Adv. Mater.*, p. n/a-n/a, 2015.

[80] S. Sohrabi, J. Zheng, E. A. Finol, and Y. Liu, “Numerical Simulation of Particle Transport and Deposition in the Pulmonary Vasculature,” *J. Biomech. Eng.*, vol. 136, no. 12, p. 121010, 2014.

[81] S. Sohrabi, S. Wang, J. Tan, J. Xu, J. Yang, and Y. Liu, “Nanoparticle transport and delivery in a heterogeneous pulmonary vasculature,” *J. Biomech.*, vol. 50, pp. 240–247, 2017.

[82] A. A. S. Bhagat, S. S. Kuntaegowdanahalli, and I. Papautsky, “Inertial microfluidics for continuous particle filtration and extraction,” *Microfluid. Nanofluidics*, vol. 7, no. 2, pp. 217–226, 2009.

[83] M. P. Howard, A. Gautam, A. Z. Panagiotopoulos, and A. Nikoubashman, “Axial dispersion of Brownian colloids in microfluidic channels,” *Phys. Rev. Fluids*, vol. 1, no. 4, p. 44203, 2016.

[84] S. Sohrabi, D. E. Yunus, J. Xu, J. Yang, and Y. Liu, “Characterization of nanoparticle binding dynamics in microcirculation using an adhesion probability function,” *Microvasc. Res.*, vol. 108, pp. 41–47, 2016.

[85] A. Waldschik and S. Büttgenbach, “Micro gear pump with internal electromagnetic drive,” *Microsyst. Technol.*, vol. 16, no. 8–9, pp. 1581–1587, 2010.

[86] Y. Xie, D. Ahmed, M. I. Lapsley, S. C. S. Lin, A. A. Nawaz, L. Wang, and T. J. Huang, “Single-shot characterization of enzymatic reaction constants K m and k cat by an acoustic-driven, bubble-based fast micromixer,” *Anal. Chem.*, vol. 84, no. 17, pp. 7495–7501, 2012.

[87] R. Nosrati, A. Driouchi, C. M. Yip, and D. Sinton, “Two-dimensional slither swimming of sperm within a micrometre of a surface,” *Nat. Commun.*, vol. 6, p. 8703, 2015.

[88] Y. Kim, J. Lee, and S. Kwon, “A novel micro-mixer with a quasi-active rotor: fabrication and design improvement,” *J. Micromechanics Microengineering*, vol. 19, no. 10, p. 105028, 2009.

[89] S. G. Darby, M. R. Moore, T. a Friedlander, D. K. Schaffer, R. S. Reiserer, J. P. Wikswo, and K. T. Seale, “A metering rotary nanopump for microfluidic systems.,” *Lab Chip*, vol. 10, no. 23, pp. 3218–3226, 2010.

[90] A. Tokarev, A. Aprelev, M. N. Zakharov, G. Korneva, Y. Gogotsi, and K. G. Kornev, “Multifunctional magnetic rotator for micro and nanorheological studies,” *Rev. Sci. Instrum.*, vol. 83, no. 6, 2012.

[91] D. Dendukuri, D. C. Pregibon, J. Collins, T. A. Hatton, and P. S. Doyle, “Continuous-flow lithography for high-throughput microparticle synthesis,” *Nat. Mater.*, vol. 5, no. 5, pp. 365–369, 2006.

[92] X. Zeng and H. Jiang, “JMEMS Letters,” *J. Microelectromechanical Syst.*, vol. 20, no. 3, pp. 353–354, 2011.

[93] M. Kaynak, A. Ozcelik, N. Nama, A. Nourhani, P. E. Lammert, V. H. Crespi, and T. J. Huang, “Acoustofluidic actuation of in situ fabricated microrotors,” *Lab Chip*, vol. 16, pp. 33–35, 2016.

[94] T. Yue, M. Nakajima, M. Takeuchi, and T. Fukuda, “Improved laser manipulation for on-chip fabricated microstructures based on solution replacement and its application in single cell analysis,” *Int. J. Adv. Robot. Syst.*, vol. 11, no. 1, 2014.

[95] T. F. Scott, B. A. Kowalski, A. C. Sullivan, C. N. Bowman, and R. R. McLeod, “Two-Color

Single-Photon Photoinitiation and Photoinhibition for Subdiffraction Photolithography," *Science (80-.).*, vol. 324, no. 5929, p. 913 LP-917, May 2009.

[96] J. Melin, G. Giménez, N. Roxhed, W. van der Wijngaart, and G. Stemme, "A fast passive and planar liquid sample micromixer," *Lab Chip*, vol. 4, no. 3, pp. 214–219, 2004.

[97] K. S. Ryu, K. Shaikh, and C. Liu, "Micro Magnetic Stir-Bars Integrated Parylene Su ~ Ace-Micromachined," *October*, pp. 635–638, 2003.

[98] M. Islam, H. Brink, S. Blanche, C. DiPrete, T. Bongiorno, N. Stone, A. Liu, A. Philip, G. Wang, W. Lam, A. Alexeev, E. K. Waller, and T. Sulchek, "Microfluidic Sorting of Cells by Viability Based on Differences in Cell Stiffness," *Sci. Rep.*, vol. 7, no. 1, p. 1997, 2017.

[99] F. Abhari, H. Jaafar, and N. A. Md Yunus, *A comprehensive study of micropumps technologies*, vol. 7, no. 10. 2012.

[100] A. Ezkerra, L. J. Fern??ndez, K. Mayora, and J. M. Ruano-L??pez, "A microvalve for lab-on-a-chip applications based on electrochemically actuated SU8 cantilevers," *Sensors Actuators, B Chem.*, vol. 155, no. 2, pp. 505–511, 2011.

[101] C. Groth, N. D. Kravitz, P. E. Jones, J. W. Graham, and W. R. Redmond, "Three-dimensional printing technology.," *J. Clin. Orthod.*, vol. 48, no. 8, pp. 475–85, 2014.

[102] R. K. Chen, Y. an Jin, J. Wensman, and A. Shih, "Additive manufacturing of custom orthoses and prostheses-A review," *Addit. Manuf.*, vol. 12, pp. 77–89, 2016.

[103] E. Barnett and C. Gosselin, "Large-Scale 3D Printing With A Cable-Suspended Robot," *Addit. Manuf.*, vol. 7, pp. 27–44, 2015.

[104] Y. Zhang, F. Zhang, Z. Yan, Q. Ma, X. Li, Y. Huang, and J. A. Rogers, "Printing, folding and assembly methods for forming 3D mesostructures in advanced materials," *Nat. Rev. Mater.*, vol. 2, p. 17019, Mar. 2017.

[105] A. A. Pawar, G. Saada, I. Cooperstein, L. Larush, J. A. Jackman, S. R. Tabaei, N.-J. Cho, and S. Magdassi, "High-performance 3D printing of hydrogels by water-dispersible photoinitiator nanoparticles.," *Sci. Adv.*, vol. 2, no. 4, p. e1501381, 2016.

[106] R. He, D. Yunus, C. Uhl, W. Shi, S. Sohrabi, and Y. Liu, "Fabrication of circular microfluidic channels through grayscale dual-projection lithography," *Microfluid. Nanofluidics*, vol. 21, no. 1, p. 13, 2017.

[107] D. E. Yunus, S. Sohrabi, R. He, W. Shi, and Y. Liu, "Acoustic patterning for 3D embedded electrically conductive wire in stereolithography," *J. Micromechanics Microengineering*, vol. 27, no. 4, p. 45016, 2017.

[108] X. Song, Y. Chen, T. W. Lee, S. Wu, and L. Cheng, "Ceramic fabrication using Mask-Image-Projection-based Stereolithography integrated with tape-casting," *J. Manuf. Process.*, vol. 20, pp. 456–464, 2015.

[109] S. S. Crump, "Apparatus and Method for Creating Three-Dimensional Objects," *US Pat. 5,121,329*, p. 15, 1992.

[110] C. W. Hull, “Apparatus for production of three-dimensional objects by stereolithography,” *US Pat. 4,575,330*, pp. 1–16, 1986.

[111] K. Takagishi and S. Umezu, “Development of the Improving Process for the 3D Printed Structure,” *Sci. Rep.*, vol. 7, no. November 2016, p. 39852, 2017.

[112] A. A. Giannopoulos, D. Mitsouras, S.-J. Yoo, P. P. Liu, Y. S. Chatzizisis, and F. J. Rybicki, “Applications of 3D printing in cardiovascular diseases,” *Nat Rev Cardiol*, vol. 13, no. 12, pp. 701–718, Dec. 2016.

[113] J. W. Stansbury and M. J. Idacavage, “3D printing with polymers: Challenges among expanding options and opportunities,” *Dent. Mater.*, vol. 32, no. 1, pp. 54–64, 2016.

[114] F. Cooper, “Sintering and additive manufacturing: ‘additive manufacturing and the new paradigm for the jewellery manufacturer,’” *Prog. Addit. Manuf.*, vol. 1, no. 1–2, pp. 29–43, 2016.

[115] B. Lu, D. Li, and X. Tian, “Development trends in additive manufacturing and 3D printing,” *Engineering*, vol. 1, no. 1, pp. 85–89, 2015.

[116] A. P. Zhang, X. Qu, P. Soman, K. C. Hribar, J. W. Lee, S. Chen, and S. He, “Rapid fabrication of complex 3D extracellular microenvironments by dynamic optical projection stereolithography,” *Adv. Mater.*, vol. 24, no. 31, pp. 4266–4270, 2012.

[117] Y. Lu, G. Mapili, G. Suhali, S. Chen, and K. Roy, “A digital micro-mirror device-based system for the microfabrication of complex, spatially patterned tissue engineering scaffolds,” *J. Biomed. Mater. Res. - Part A*, vol. 77, no. 2, pp. 396–405, 2006.

[118] J. R. Tumbleston, D. Shirvanyants, N. Ermoshkin, R. Janusziewicz, A. R. Johnson, D. Kelly, K. Chen, R. Pinschmidt, J. P. Rolland, A. Ermoshkin, E. T. Samulski, and J. M. DeSimone, “Continuous liquid interface production of 3D objects,” *Science (80-.).*, vol. 347, no. 6228, p. 1349 LP-1352, Mar. 2015.

[119] M. P. Lee, G. J. T. Cooper, T. Hinkley, G. M. Gibson, M. J. Padgett, and L. Cronin, “Development of a 3D printer using scanning projection stereolithography.,” *Sci. Rep.*, vol. 5, p. 9875, 2015.

[120] S. C. Joshi and A. A. Sheikh, “3D printing in aerospace and its long-term sustainability,” *Virtual Phys. Prototyp.*, vol. 10, no. 4, pp. 175–185, Oct. 2015.

[121] C. L. Ventola, “Medical Applications for 3D Printing: Current and Projected Uses.,” *P T*, vol. 39, no. 10, pp. 704–711, 2014.

[122] S. Applications, “Dental applications of 3D printing,” *Dent. Abstr.*, vol. 61, no. 4, pp. 209–211, 2016.

[123] Y. L. Yap and W. Y. Yeong, “Additive manufacture of fashion and jewellery products: a mini review,” *Virtual Phys. Prototyp.*, vol. 9, no. 3, pp. 195–201, Jul. 2014.

[124] P. S. Heath, “3D Printing ; Hardware and Software for the Consumer Market,” *Int. J. Students’ Res. Technol. Manag.*, vol. 3, no. December, pp. 440–444, 2015.

[125] A. Pandian and C. Belavek, “A review of recent trends and challenges in 3D printing,” *Proc. 2016 ASEE North Cent. Sect. Conf.*, pp. 1–17, 2016.

[126] D. For, P. An, O. By, M. Of, P. Et, D. Permettant, D. E. P. Un, and O. Par, “EP001192041B1,” 2003.

[127] The Chemours Company FC, “Teflon ™ AF Solutions,” 2016.

[128] J. Shi, M. B. Chan-Park, C. Gong, H. Yang, Y. Gan, and C. M. Li, “Spatially controlled oxygen inhibition of acrylate photopolymerization as a new lithography method for high-performance organic thin-film transistors,” *Chem. Mater.*, vol. 22, no. 7, pp. 2341–2346, 2010.

[129] M. Li, Y. Luo, H. Wu, K. Zhu, Y. Niu, T. Zhao, J. Xing, and Z. Kang, “A Prenecking Strategy Makes Stretched Membranes With Clamped Ends Wrinkle-Free,” *J. Appl. Mech.*, vol. 84, no. 6, p. 61006, 2017.

[130] Z. C. Eckel, C. Zhou, J. H. Martin, A. J. Jacobsen, W. B. Carter, and T. A. Schaedler, “Additive Manufacturing of Polymer-Derived Ceramics,” *Science (80-.).*, vol. 351, no. 6268, pp. 58–62, 2016.

[131] D. E. Yunus, R. He, W. Shi, O. Kaya, and Y. Liu, “Short fiber reinforced 3d printed ceramic composite with shear induced alignment,” *Ceram. Int.*, no. June, pp. 0–1, 2017.

Vita

Ran He was born on February 27th, 1990 in Qiqihar, Heilongjiang Province, China to Lianke He and Yuping Wang. Ran's father is an engineer, and mother is a math teacher. He attended Shanghai Jiao Tong University, Shanghai, China in 2008. Before his Ph.D. study, he has experienced many areas in mechanical engineering, including turbine engine and robotics. Now his research areas are focused on additive manufacturing and microfabrication. He was awarded Rossin Doctoral Fellowship and Graduate Fellowship from Lehigh University. After graduation, he will start his career in Formlabs Inc., a 3D printing company located in Boston, MA, USA.

EDUCATION

Lehigh University, College of Engineering & Applied Science, Bethlehem, PA
Ph.D*. in Mechanical Engineering & Mechanics* 2017
M.Sc. *in Mechanical Engineering & Mechanics* 2014

Shanghai Jiao Tong University (SJTU), Shanghai, China 2012
B.S. *in Mechanical Engineering*

PATENTS

Y. Liu, **R. He**, and W. Shi, "All Dimensional Fabrication Apparatus and Methods", U.S. Patent, US20160303795A1, published on Oct 20, 2016.

J. Fei, **R. He**, H. Zhou, J. Zhai, Z. Fu, and Y. Zhao, "Multi-Degree-of-Freedom Single-Wound-Hole Robot Flexible Hand for Celiac Minimally Invasive Surgery", C.N. Patent, CN102499759B, issued on Nov 20, 2013. **Grant**

PEER-REVIEWED JOURNAL PUBLICATION

R. He, D. Yunus, C. Uhl, W. Shi, S. Sohrabi, and Y. Liu, "Fabrication of Circular Microfluidic Channels through Grayscale Dual-projection Lithography", *Microfluidics and Nanofluidics*, 21(1),13, 2017

R. He, S. Wang, G. Andrews, W. Shi, and Y. Liu, "Generation of Customizable Micro-Wavy Pattern through Grayscale Direct Image Lithography", *Scientific Reports*, 6,21621, 2016

D. Yunus, **R. He**, W. Shi, O. Kaya, and Y. Liu, "Short Fiber Reinforced 3D Printed Ceramic Composite with Shear Induced Alignment", *Ceramics International,* 2017

W. Shi, **R. He** and Y. Liu, "3D Printing Scaffolds with Hydrogel Materials for Biomedical Applications", *European Journal of BioMedical Research,* 1(3), 3-8, 2015

D. Yunus, S. Sohrabi, **R. He**, W. Shi and Y. Liu, "Acoustic Patterning for Embedded Electrically Conductive Wire in Stereolithography", *Journal of Micromechanics and Microengineering,* 27, 2017

J. Tan, S. Sohrabi, **R. He**, "Numerical Simulation of Cell Squeezing through A Micropore by the Immersed Boundary Method", *Journal of Mechanical Engineering Science,* 2017

A. Thomas, S. Wang, S. Sohrabi, C. Orr, **R. He**, W. Shi and Y. Liu, "Characterization of Vascular Permeability Using a Biomimetic Microfluidic Blood Vessel Model", *Biomicrofluidics,* 11, 024102, 2017

W. Shi, S. Wang, A. Maarouf, C. Uhl, **R. He**, D. Yunus, Y. Liu, "Magnetic Particles Assisted Capture and Release of Rare Tumor Cells using Wavy-Herringbone Structured Microfluidic Devices", *Lab on a Chip,* 2017

R. He, J. Landowne, J. Currie, C. Uhl, W. Shi, D. Yunus, J. Amoah, and Y. Liu, "3D Printing of Large Objects by Scanning Lithography", *Additive Manufacturing,* under review

W. Shi, **R. He**, D. Yunus, J. Yang and Y. Liu, "A Facile Way to Fabricate Transparent Superhydrophobic Surfaces", *Nanotechnology,* under review

S. Sohrabi, J. Tan, D. Yunus, **R. He** and Y. Liu, "Label-free Sorting of Soft Microparticles Using a Bioinspired Synthetic Cilia Array", *Microfluidics and Nanofluidics*, under review

R. He, D. Yunus, W. Shi and Y. Liu, "In situ generation of controllable microfluidic actuators", in preparation

CONFERENCE PRESENTATION

Poster Presentation, TechConnect World Innovation Conference & Expo, "Pixel Sweeping Technology enabling 3D Printing of Large-Scale Object with delicate Details", May 2017, National Harbor, Maryland, USA

Presenter, TechConnect World Innovation Conference & Expo, "High-Speed All Dimensional 3D Printing", May 2016, National Harbor, Maryland, USA

Poster presentation, Global Commercialization Conference, "All Dimensional Continuous Fabrication", December 2015, New Brunswick, NJ, USA

Poster presentation, Life Sciences Future, "Cell/Membrane Stretcher", October 2014, Philadelphia, PA, USA

Conference Paper: Isolation of Rare Tumor Cells Using Adhesion Rolling in a Microfluidic Chip with Inclined Wavy Surfaces SB^3C2016-749

EMPLOYMENT EXPERIENCE

Research Assistant - Lehigh University 2012-2017

- Bio-Nanomechanics Laboratory
- Mechatronics Laboratory

Teaching Assistant - Lehigh University

- Numerical Method in Mechanical Engineering Fall 2015 & 2016
- Nuclear Reactor Engineering & Renewable Energy Spring 2014
- Mathematical Methods in Engineering I Fall 2013

Quality Engineer (Intern) - General Motors (Shanghai) Corp. Ltd Jun - Sep 2011